

Development of A Gadolinium-Based Nanotheranostics Platform  
for Irradiation Activatable MRI-Radiosensitization and  
Doxorubicin Release in Cancer Therapy

by

Zhipeng Yuan

A thesis submitted in partial fulfillment of the requirements for the degree of

Doctor of Philosophy

Department of Biomedical Engineering  
University of Alberta

© Zhipeng Yuan, 2022

## Abstract

The ultimate goal of this thesis research was to design, fabricate, and characterize an integrated nanotheranostics platform for activatable doxorubicin delivery and simultaneous MRI-radiosensitization for synergistic cancer therapy, targeting breast cancer treatment. As shown in the diagram, once these nanocomplexes enter into tumour sites through the EPR (enhanced permeability and retention) effect, an external radiation source can be applied with extreme precision to activate the cleavage of the mPGA shells (the outer fluorescent blue layer in the diagram). This exposes the positively charged Gd:Mn-Dox cores which are readily adsorbed by the negatively charged cancer cell membrane and internalized through endocytosis. The acidic environment within endosomes then triggers the dissociation of the Gd:Mn-Dox nanocomplexes contained within them, and resulting release of doxorubicin and gadolinium for simultaneous real time MRI-radiosensitization and synergistic therapy.

Gadolinium, as one of lanthanide metal elements, has been well investigated and its chelates are commonly used as  $T_1$  contrast agents for clinical magnetic resonance imaging (MRI). Anthracycline antibiotics, such as the cancer chemotherapeutic drug doxorubicin, can form complexes with transition metals. Gadolinium and doxorubicin drug-metal complexes were selected for study, and were fabricated as nanostructures through a simple one-step homogeneous precipitation method. They were designed for acidic environment-triggered doxorubicin and gadolinium release. A partially modified poly-glutamic acid polymer (which was esterified to prevent the polymer material from undergoing auto-hydrolysis) was used to coat the surface of the harvested spherical Gd:Mn-Dox nanocomplexes. This surface coating was designed to be radiation activatable and biocompatible.

The first nanostructures synthesized in this thesis were  $\text{Gd}(\text{OH})_3$  and  $\text{Gd}(\text{OH})_3:\text{Mn}$  crystalline nanorods, and rod-shaped crystalline  $\text{Gd}(\text{OH})_3:\text{Mn}$ -Dox nanocomplexes with a 7.85wt% drug loading capacity of doxorubicin. The longitudinal dimension of these nanorods and nanocomplexes ranged from 200 nm to 400 nm. Next, the reaction process was modified to successfully produce spherical amorphous  $\text{Gd}:\text{Mn}$  and  $\text{Gd}:\text{Mn}$ -Dox nanocomplexes with a higher doxorubicin loading capacity (10.1wt%). The diameter of these nanospheres could be tuned within the range of 100 nm to 500 nm by using different quantities of glycerol in the reaction process. Both the rod-shaped and spherical nanocomplexes were demonstrated to undergo dissociation and release of doxorubicin and gadolinium in acidic environments. The amorphous spherical nanocomplexes had a shorter release time relative to the crystalline rod-shaped nanocomplexes. Confocal and TEM micrographs demonstrated that the synthesized nanocomplexes were actively taken up via endocytosis by human breast cancer cells. A radiation-activated radiosensitization effect, as well as dose-dependent trends in the percentage of apoptotic cells, were measured in the nanocomplex-treated cancer cells *in vitro*. MRI traceability of this nanotheranostics platform was demonstrated both *in vitro* and *in vivo*, using clinical MRI and PET-MRI. These nanocomplexes were well tolerated in rats at the highest tested dose of 240 mg/kg administered intravenously, with negligible histological changes observed. The *in vivo* biodistribution of these intravenously injected nanocomplexes was observed to be mainly in the liver, lungs and spleen.

Overall, a novel and smart doxorubicin-loaded gadolinium-based amorphous cancer nanotheranostic system was developed with a very simple and environmentally-friendly fabrication process. This system demonstrated the capability to deliver gadolinium and doxorubicin for theranostic MRI-radiosensitization and doxorubicin chemotherapy. This

proposed nanotheranostics platform represents an increasing trend in cancer nanotheranostics towards the research and development of novel and much more effective drug delivery platforms which pave the way for individualized cancer medicine.

This thesis work has explored the feasibility of fabricating a new amorphous-phase gadolinium-based drug/metal theranostic nanocomplex doped with manganese through an environmentally friendly process. The research performed in this thesis takes advantage of the fact that doxorubicin drug molecules can form drug-metal complexes with gadolinium and manganese ions, allowing one to avoid incorporating other complex chelating materials. This work also uses a “smart” radiation-activable strategy for theranostic cargo delivery. This new design of a nanotheranostic solution paves the way for new clinical workflows where real-time MRI-guided synergistic therapy can be carried out during treatment. This work also inspired the consideration of other suitable drugs that may be studied using a similar work flow to extend their potential applications into theranostics and brought about new insights regarding the fabrication of theranostic nanoplatfoms.

## Preface

This thesis is an original work by Zhipeng Yuan. The research project, of which this thesis is a part, received research ethics approval from the University of Alberta Research Ethics Board, Project Name “Radiation Sensitive Nanoparticles For Breast Cancer Therapy”, No. AC14213, December 11, 2014.

Chapter 2 of this thesis has been published as S.S. Yoo, L. Guo, X. Sun, A.R. Shaw, Z. Yuan, R. Löbenberg, and W.H. Roa, “Fabrication and *in vitro* characterization of gadolinium-based nanoclusters for simultaneous drug delivery and radiation enhancement,” *Nanotechnology*, vol. 27, 385104. I (Z. Yuan) was responsible for the materials fabrication, manuscript composition, *in vitro* cellular uptake, *in vivo* study and nanostructure formation mechanism deduction. S.S. Yoo was also responsible for the manuscript composition, materials fabrication, conducting experiments, as well as the data collection and analysis. L. Guo was responsible for concept formation, as well as materials fabrication, data analysis and manuscript composition. X. Sun was responsible for the TEM study. R. Löbenberg and W.H. Roa were the supervisory authors and were involved with concept formation and manuscript review.

Portions of Chapter 3 and Chapter 4 have been published or represented as Z. Yuan, L. Guo, S.S. Yoo, R. Löbenberg, and W.H. Roa, “A Gadolinium-Doxorubicin Nanocomplex as A Novel Targeted Drug-Delivery System,” *CSPS/CC-CRS Conference 2016, Vancouver, BC, Canada, AAPS Conference 2016, Denver, CO, United States and Alberta Nano Research Symposium 2016, Edmonton, AB, Canada*. I (Z. Yuan) was responsible for the materials fabrication and characterization, manuscript composition, *in vitro* cellular uptake, *in vivo* study and nanostructure formation mechanism deduction, conducting experiments, as well as the data collection and analysis. L. Guo and S.S. Yoo were responsible for concept formation, materials

fabrication and data analysis. R. Löbenberg and W.H. Roa were the supervisory authors and were involved with concept formation and manuscript review.

## **Dedication**

I would like to dedicate this work to my maternal grandfather who just defeated his cancer; my maternal grandmother who was holding her husband's hands tightly in the days that he was fighting cancer; my beloved parents; and my sister.

## **Acknowledgements**

I would like to thank my supervisors Dr. Robert Burrell, Dr. Jie Chen, Dr. Todd McMullen, Dr. Raimar Löbenberg, Dr. Wilson Roa and Dr. Frank Wuest for their help and advice. I would also like to thank my supervisory, candidacy (Dr. Afsaneh Lavasanifar, Dr. Michael Doschak), and defense committees for their efforts. A special thank goes to Dr. Linghong Guo for his generous help and advice from the very beginning and throughout the whole journey; Dr. Patricia Nadworny for editing the thesis with me; and Ms. Shannon Yoo for helping me become familiar with the lab's resources and teaching me the techniques to use during the rod-shaped gadolinium nanocomplexes project. I would also like to thank Dr. Zi-Hua Justin Jiang from Lakehead University for providing the mPGA materials. I would like to thank the Cell Imaging Facility, Division of Experimental Oncology, Department of Oncology, University of Alberta for allowing me to use their space and research instruments and for the help of their supportive staff. I would also like to acknowledge the Vivarium Manager, Mr. Dan McGinn, at the Cross Cancer Institute for his valuable support towards completing the animal studies in this thesis; as well as Dr. Ronald Moore from the Department of Surgery, University of Alberta, for letting me use their lab space and cell culture facility. I would also like to recognize Dr. Don Robinson from the Department of Medical Physics, University of Alberta, for his help with the radiation tests; Dr. Keith Wachowicz, also from the Department of Medical Physics, University of Alberta, and Mr. Kevin Kevamme and his colleagues at the Cross Cancer Institute for their help with the MRI experiments. I would also like to thank the following previous Ph.D. students and postdoctoral fellows at the University of Alberta: Hoda Soelyamni Abyaneh, Leandro Santoro, Xia Xu, Deepak Dinakaran, Igor Paiva, and others, for always standing by me as I pursued my goals.

Finally, I would like to express my deep gratitude to Dr. Robert Burrell, Dr. Victoria Ruetalo, Dr. John Lewis and Dr. Pengfei Wang, who lifted me out of troubled waters and offered me the confidence and courage to achieve my goal of completing my thesis at the University of Alberta; as well as Dr. Yanfang Li from Sichuan University who supervised my Master's thesis and ignited the fire in me to complete a doctoral thesis. The following sources of assistance funded this work: the Canadian Breast Cancer Foundation and the China Scholarship Council.

## Table of Contents

<b>Chapter 1 – Introduction.....</b>	<b>1</b>
Cancer Nanomedicine.....	1
Cancer Nanotheranostics .....	4
MRI and MRI Contrast Agents .....	8
Radiation Therapy and Radiosensitization in Cancer Treatment .....	12
Gd and Gd Nanotheranostics.....	13
Doxorubicin.....	24
Previous Gadolinium-Based Nanocomplex Research by This Group.....	25
Gadolinium-Layered Nanocomplexes for Anti-miRNA Oligonucleotide Delivery in Human Breast Cancer Cells and Magnetic Resonance Imaging.....	25
Gadolinium-Dox Nanorod Complexes for Doxorubicin Delivery and Simultaneous MRI-Radiosensitization .....	26
Purpose .....	28
Thesis Outline.....	29
<b>Chapter 2 – Manufacture of Gadolinium-Based Nanocomplexes.....</b>	<b>32</b>
Introduction .....	32
Materials and Methods .....	35
Materials.....	35
Fabrication of Gd(OH) <sub>3</sub> , Gd(OH) <sub>3</sub> :Mn Nanorods and Gd(OH) <sub>3</sub> :Mn-Dox Nanocomplexes and Study of Their Morphology .....	36
Characterization of the Obtained Nanoparticles by SEM, TEM, and X-Ray Powder Diffraction .....	37

Cell Culture .....	37
Determination of Cellular Uptake of Gd(OH) <sub>3</sub> :Mn-Dox Nanocomplexes .....	38
<i>In Vitro</i> Cytotoxicity and Radiation Sensitizing Effect Assessment .....	38
<i>In Vivo</i> Observation of Acute Toxicity and Organ Distribution (Pilot Study).....	40
Synthesis of Gd:Mn Nanospheres .....	40
Results & Discussion.....	42
Fabrication of Gd(OH) <sub>3</sub> , Gd(OH) <sub>3</sub> :Mn Nanorods and Gd(OH) <sub>3</sub> :Mn-Dox Nanocomplexes and Study of Their Morphology .....	42
Characterization of the Obtained Nanoparticles by X-Ray Powder Diffraction....	45
Determination of Cellular Uptake of Gd(OH) <sub>3</sub> :Mn-Dox Nanocomplexes .....	47
<i>In Vitro</i> Cytotoxicity and Radiation Sensitizing Effect Assessment .....	48
<i>In Vivo</i> Observation of Acute Toxicity and Organ Distribution (Pilot Study).....	51
Synthesis of Gd:Mn Nanospheres .....	52
Conclusions .....	57
<b>Chapter 3 – Modifying Morphology and Loading Gd:Mn Nanospheres .....</b>	<b>58</b>
Introduction .....	58
Materials and Methods .....	60
Materials.....	60
Loading Gd:Mn Nanospheres with Doxorubicin.....	60
Preparation of Partially Modified Poly- $\alpha$ , L-Glutamic Acid (mPGA).....	62
Fabrication of mPGA@Gd:Mn and mPGA@Gd:Mn-Dox.....	63
Results & Discussion.....	63
Loading Gd:Mn Nanospheres with Doxorubicin.....	63

Preparation of Partially Modified Poly- $\alpha$ , L-Glutamic Acid (mPGA).....	67
Fabrication of mPGA@Gd:Mn and mPGA@Gd:Mn-Dox.....	69
Conclusions .....	70
<b>Chapter 4 – <i>In Vitro</i> Characterization of Fabricated Nanospheres .....</b>	<b>72</b>
Introduction .....	72
Materials and Methods .....	74
Materials.....	74
X-ray Powder Diffraction.....	75
Elemental Analysis via Energy Dispersive X-ray Spectroscopy (EDS) and UV-Vis Spectroscopy of the Obtained Nanodispersions.....	75
Radiolytic Activation of the Modified PGA Candidates .....	76
<i>In Vitro</i> Low pH-Responsive Doxorubicin Release from mPGA-Coated Gd:Mn-Dox Nanospheres via Radiolytic Activation of the mPGA Coatings .....	76
Doxorubicin Stability Study.....	77
<i>In Vitro</i> Cellular Uptake of Gd:Mn Nanospheres, Doxorubicin-Loaded Gd:Mn-Dox Nanospheres and Radiation Activated/Non-Activated mPGA@Gd:Mn-Dox Nanospheres using Confocal Laser Scanning Microscopy and Transmission Electron Microscopy .....	78
<i>In Vitro</i> Cytotoxicity and Biocompatibility Studies.....	80
<i>In Vitro</i> Magnetic Resonance Imaging (MRI) .....	82
Results & Discussion.....	83
X-ray Powder Diffraction.....	83

Elemental Analysis via Energy Dispersive X-ray Spectroscopy (EDS) and UV/Vis spectroscopy of the Obtained Nanodispersions .....	84
Radiolytic Activation of the Modified PGA Candidates .....	86
<i>In Vitro</i> Low pH-Responsive Doxorubicin Release from mPGA-Coated Gd:Mn-Dox Nanospheres via Radiolytic Activation of the mPGA Coating.....	88
Doxorubicin Stability Study.....	89
<i>In Vitro</i> Cellular Uptake of Gd:Mn Nanospheres, Doxorubicin-Loaded Gd:Mn-Dox Nanospheres and Radiation Activated/Non-Activated mPGA@Gd:Mn-Dox Nanospheres using Confocal Laser Scanning Microscopy and Transmission Electron Microscopy .....	90
<i>In Vitro</i> Cytotoxicity and Biocompatibility .....	95
<i>In Vitro</i> Magnetic Resonance Imaging (MRI) .....	100
Conclusions .....	102
<b>Chapter 5 – <i>In Vivo</i> Animal Studies Using a Rat Model.....</b>	<b>104</b>
Introduction .....	104
Materials and Methods .....	107
Materials.....	107
Xenograft Human Breast Cancer Tumour-Bearing Rat Model .....	107
<i>In Vivo</i> Biodistribution Study of mPGA@Gd:Mn-Dox Nanospheres Using mPGA NO. 132 .....	108
<i>In Vivo</i> Toxicity Testing of Gd:Mn, Gd:Mn-Dox and mPGA@Gd:Mn-Dox Nanospheres .....	108
<i>In Vivo</i> MR Imaging.....	112

Results & Discussion.....	113
Xenograft Human Breast Cancer Tumour-Bearing Rat Model .....	113
<i>In Vivo</i> Biodistribution of mPGA@Gd:Mn-Dox Nanospheres .....	114
<i>In Vivo</i> Toxicity Testing of Gd:Mn, Gd:Mn-Dox and mPGA@Gd:Mn-Dox Nanospheres .....	116
<i>In Vivo</i> MR Imaging.....	119
Conclusions .....	122
<b>Chapter 6 – Conclusions.....</b>	<b>123</b>
Conclusions .....	123
<b>Bibliography .....</b>	<b>128</b>

## List of Tables

<b>Table 2-1.</b> Sizes of Gd(OH) <sub>3</sub> nanorods, Gd(OH) <sub>3</sub> :Mn nanorods and Gd(OH) <sub>3</sub> :Mn-Dox nanocomplexes in Figure 1. ....	45
<b>Table 2-2.</b> Components and refinement parameters of the synthesized crystal nanostructures...	47
<b>Table 2-3.</b> Clonogenicity assay results of irradiated and non-irradiated groups treated with Gd(OH) <sub>3</sub> :Mn nanorods or Gd(OH) <sub>3</sub> :Mn-Dox nanocomplexes. ....	50
<b>Table 3-1.</b> a: The synthesized nanospheres showed a decreased diameter after doxorubicin was added to the reaction system; b: different ratios of glycerol:urea affected the morphology and diameter of the final products.....	66
<b>Table 3-2.</b> Particles size of nanospheres before and after the coating procedure. ....	70
<b>Table 5-1.</b> Experimental animal body sign scoring sheet. ....	110
<b>Table 5-2.</b> The established tumour model growth rate.....	113

## List of Figures

- Figure 2-1.** Transmission electron microscopy (left column) and scanning electron microscopy (right column) images of Gd(OH)<sub>3</sub> (a) and Gd(OH)<sub>3</sub>:Mn (b) nanorods, as well as Gd(OH)<sub>3</sub>:Mn-Dox nanocomplexes (c)..... 44
- Figure 2-2.** Proposed mechanism for the interaction between doxorubicin molecules and Gd(OH)<sub>3</sub>:Mn nanorods. Doxorubicin molecules work as binding agents to holding the assembled nanorods together in bundles. Cyan=gadolinium, grey=carbon, white=hydrogen, red=oxygen, blue=nitrogen (Mn not shown). ..... 45
- Figure 2-3.** X-ray powder diffraction patterns of Gd(OH)<sub>3</sub> nanorods, Gd(OH)<sub>3</sub>:Mn nanorods, and Gd(OH)<sub>3</sub>:Mn-Dox nanocomplexes. .... 46
- Figure 2-4.** Confocal images of cellular uptake of Gd(OH)<sub>3</sub>:Mn-Dox nanocomplexes after 4 hours, 24 hours, and six days of incubation with MDA-MB-231 cells. Blue indicates cell nuclei and red indicates doxorubicin loaded within, and released from, the nanocomplexes..... 48
- Figure 2-5.** MDA-MB-231 cell apoptotic rates after various treatments. The x-axis shows an increasing dose of Gd(OH)<sub>3</sub>:Mn-Dox nanocomplexes applied to experimental groups with or without radiation. Solid colour filled columns represent irradiated groups, while the white columns represent non-irradiated groups. \*\**p* < 0.0001..... 49
- Figure 2-6.** Clonogenicity assay results comparing irradiated and non-irradiated groups treated with Gd(OH)<sub>3</sub>:Mn nanorods or Gd(OH)<sub>3</sub>:Mn-Dox nanocomplexes. \*\**p* < 0.0001..... 50
- Figure 2-7.** Gadolinium content in different organs of interest in a female RNU rat with human breast cancer tumor xenograft 24 hours after injection of Gd(OH)<sub>3</sub>:Mn-Dox. The

gadolinium uptake in different organs was assessed using ICP-MS. The data are presented as the percentage of the total injected dose per gram of tissue..... 52

**Figure 2-8.** a: The reactor used for synthesizing Gd:Mn nanospheres consisted of an autoclave tube (a-1) lined with a Teflon tube (a-2), a-3 shows the synthesized Gd:Mn nanospheres suspended in ddH<sub>2</sub>O. b: TEM images of Gd:Mn nanospheres produced at different diameters (from b-1 to b-5, these were produced with 0.4, 0.8, 2.4, 3.2, and 5 mL of glycerol solution, respectively); note that the last image (b-6) shows rod/rice-like particles produced with excess quantities of urea solution (7.5 mL). c: The relationship between the quantity of glycerol solution used and particle sizes of corresponding synthesized Gd:Mn nanospheres is shown. .... 56

**Figure 3-1.** Reaction scheme for hydrophobic modification of the poly (L-glutamic acid). RCH<sub>2</sub> = investigated lipophilic substitutes. .... 62

**Figure 3-2.** a: Synthesized white Gd:Mn nanospheres and purple doxorubicin-loaded (Gd:Mn-Dox) nanospheres suspended in ddH<sub>2</sub>O; b, c, d: TEM images of Gd:Mn-Dox nanospheres of various sizes, which were achieved by varying the ratio of glycerol:urea – in the figure, the ratios used were 0.8:1.5, 0.4:2, and 0.4:1.5, respectively); e, f: SEM images of Gd:Mn-Dox nanospheres. .... 65

**Figure 3-3.** Schematic diagram of the radiolytic process. RCH<sub>2</sub> = selected lipophilic substituents; x = carboxyl group on the side chains of a PGA molecule..... 68

**Figure 3-4.** A schematic diagram showing a nanosphere surface coated with mPGA molecules.

 represents mPGA molecules, and  represents Gd:Mn or Gd:Mn-Dox nanospheres. .... 69

**Figure 3-5.** TEM images of mPGA (NO. 132) coated nanospheres. a and b show mPGA-coated Gd:Mn (a) and Gd:Mn-Dox (b) nanospheres; the arrows indicate layers of the polymer coating and the dashed circle shows the nanosphere core. c and d show mPGA coated Gd:Mn-Dox (c) and Gd:Mn (d) nanospheres suspended in ddH<sub>2</sub>O..... 70

**Figure 4-1.** X-ray powder diffraction patterns of Gd:Mn nanospheres and Gd:Mn-Dox nanospheres. .... 83

**Figure 4-2.** Energy-dispersive x-ray spectroscopy (EDS) elements mapping of the synthesized Gd:Mn-Dox nanospheres. a: gadolinium mapping; b: EDS element spectra. Note: The Mn was not detected as it is present at trace levels in the nanospheres. .... 85

**Figure 4-3.** UV/Vis absorption spectra of doxorubicin hydrochloride solution (red), Gd(NO<sub>3</sub>)<sub>3</sub>+doxorubicin mixed solution (orange), the final reaction mixture (green), and the resulting Gd:Mn-Dox nanodispersion (purple). .... 86

**Figure 4-4.** Impact of different doses of x-ray irradiation on irradiation-induced degradation of selected mPGA candidates (**a**: NO. 132 & **b**: NO. 128A). The bar graphs on the left plot normalized absorbance at 258 nm after different irradiation doses, and the full absorbance scan after different irradiation doses is shown on the right for **a** (top) and **b** (bottom). ... 87

**Figure 4-5.** Release profiles of doxorubicin from two different types of mPGA coated Gd:Mn-Dox nanospheres with or without 30 Gy of x-ray irradiation in pH 4.5 phosphate buffered saline, over a nine day period. \*\* The mean values of the two groups indicated are significantly different ( $p < 0.0001$ ). .... 89

**Figure 4-6.** TEM images of cellular uptake of mPGA@Gd:Mn nanospheres (A, B) and x-ray activated mPGA@Gd:Mn (x-mPGA@Gd:Mn) nanospheres (C, D). Dotted and black arrows indicate cell nuclei and nanospheres (solid black spheres), respectively,

internalized in vesicular structures within the cytoplasm, i.e. at a subcellular level. E shows the ICP-MS results measuring the quantity of internalized gadolinium in the non-treated group, mPGA@Gd:Mn nanospheres treated group, and activated x-mPGA@Gd:Mn nanospheres treated group. \*\* The mean values of these two groups are significantly different ( $p < 0.0001$ ). ..... 92

**Figure 4-7.** CLSM (A, B and D) and TEM (C) analysis of cellular uptake of Gd:Mn-Dox nanospheres. A: Control cells treated with doxorubicin solution (two micrographs on the left) and Gd:Mn nanospheres without doxorubicin (two micrographs on the right). B: Cells incubated with Gd:Mn-Dox nanospheres for 6 hours (left) and 24 hours (right). C: Black arrows indicate the internalized Gd:Mn-Dox nanospheres (small black spheres) in the vesicular structures within cell cytoplasm. D: Fluorescence profile analysis from point 1 to point 2. Points 1 and 2 are two lysosomes containing Gd:Mn-Dox nanospheres (as indicated by the overlapping doxorubicin red and LysoTracker Green signals). Fluorescence signals: Blue = DAPI, Red = Doxorubicin (in A) or Gd:Mn-Dox nanospheres (in B), Green = Oregon Green (in B) or LysoTracker Green (in D). ..... 95

**Figure 4-8.** Biocompatibility study results of mPGA (A), Gd:Mn nanospheres and mPGA@Gd:Mn nanospheres (B) using an MTT assay against an MCF-7 human breast cancer cell line. .... 96

**Figure 4-9.** *In vitro* radiation enhancement effect of unloaded Gd:Mn nanospheres using an MTT test (A) and a clonogenic assay (B). Results are shown for the saline (Control), x-ray (X-ray), x-ray plus mPGA@Gd:Mn nanospheres (X-ray + mPGA @Gd:Mn) and x-ray plus x-ray activated mPGA@Gd:Mn nanospheres (X-ray + X-mPGA@Gd:Mn)

treated groups. ** The mean values of the indicated groups are significantly different ( $p < 0.0001$ ). .....	98
<b>Figure 4-10.</b> Percentage of MCF-7 cells undergoing apoptosis after three days exposure to various concentrations of Gd:Mn-Dox and mPGA@Gd:Mn-Dox nanospheres. ** The mean values of the indicated groups are significantly different ( $p < 0.0001$ ). .....	99
<b>Figure 4-11.</b> T <sub>1</sub> -weighted MRI images of Gd:Mn nanospheres (A) and T <sub>2</sub> -weighted MRI images of Gd:Mn-Dox nanospheres (B) at concentrations noted on the figures. The bar graph (C) shows the MRI signal intensity produced by the Gd:Mn-Dox nanospheres in different acidic environments (HCl solution control or pH 4.5 buffer test solution). The pH 4.5 buffer was used to mimic the lysosome environment. ....	101
<b>Figure 5-1.</b> <i>In vivo</i> biodistribution of mPGA@Gd:Mn-Dox nanospheres in major organs of female rats with xenografted human breast cancer tumours. ....	115
<b>Figure 5-2.</b> <i>In vivo</i> biodistribution of Gd:Mn-Dox nanospheres, 2 and 8 hours after injection, in major organs of female rats with xenografted human breast cancer tumours. ....	116
<b>Figure 5-3.</b> Examples of micrographs used for histological examination of various H&E stained tissues from female RNU rats treated with saline; Gd:Mn nanospheres at 24, 72, and 240 mg/kg; Gd:Mn-Dox nanospheres at 240 mg/kg; or mPGA@Gd:Mn-Dox nanospheres at 240 mg/kg; all 42 days after treatment. ....	119
<b>Figure 5-4.</b> <i>In vivo</i> T <sub>1</sub> weighted MR images of saline, Gadavist® and Gd:Mn-Dox nanosphere-treated rats. ....	121
<b>Figure 5-5.</b> <i>In vivo</i> T <sub>2</sub> weighted MR images of the rat before (left) and after (right) being injected with mPGA@Gd:Mn-Dox nanospheres. ....	122

## List of Symbols, Abbreviations, and Nomenclature

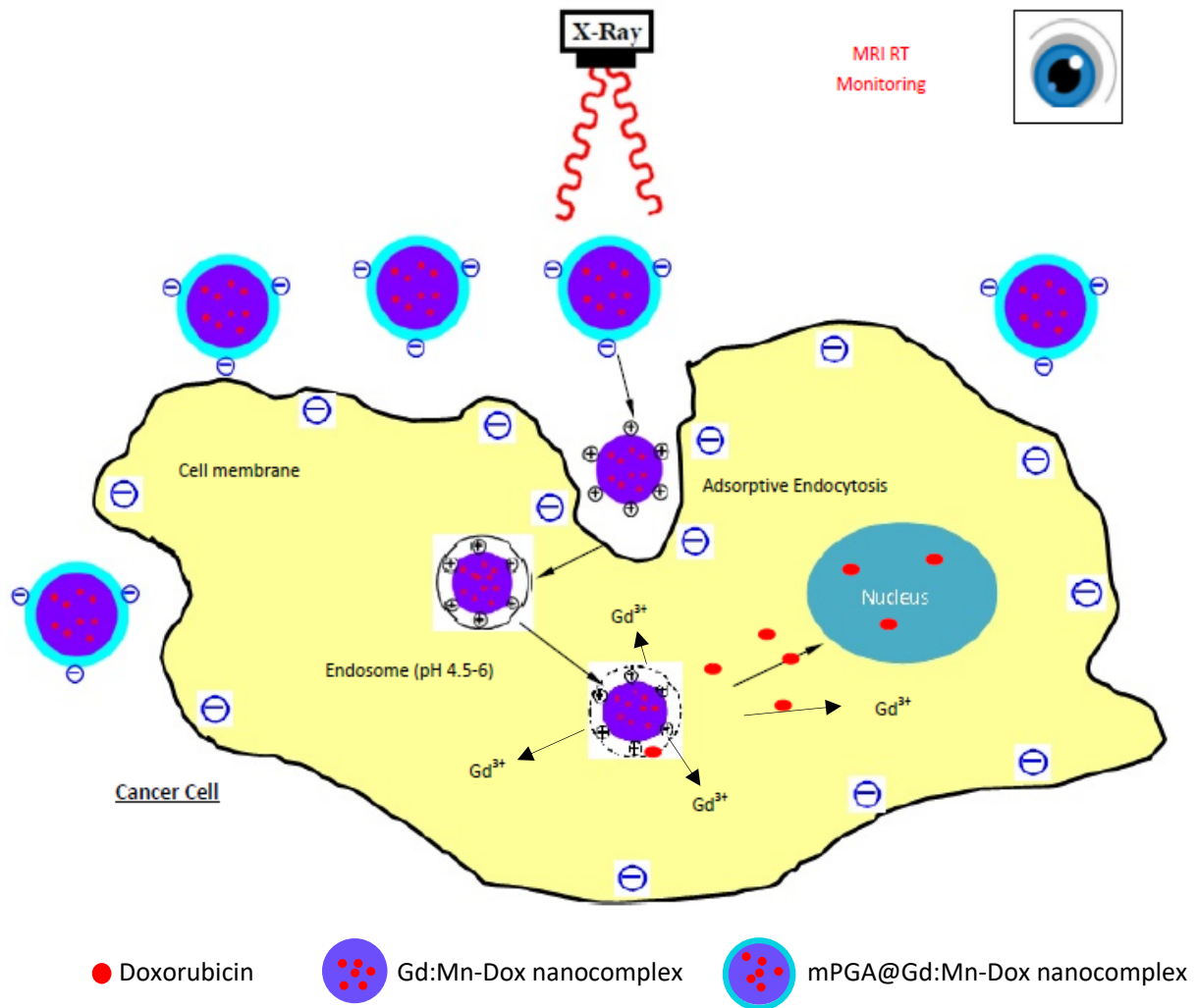
<b>Symbols</b>	<b>Definition</b>
3D	three-dimension
ANOVA	analysis of variance
APC	allophycocyanin
ATCC	American Type Culture Collection
B16F10	murine melanoma cell line
CLSM	confocal laser scanning microscope
CT	computed tomography
cTnI	cardiac troponin I
DACHPt	(1,2-diaminocyclohexane)platinum(II)
DAPI	4',6-diamidino-2-phenylindole
ddH <sub>2</sub> O	double distilled H <sub>2</sub> O
DMSO	dimethyl sulfoxide
DAD	diode array detection
DMEM	Dulbecco's Modified Eagle Medium
DNA	deoxyribonucleic acid
DOTAGA	1,4,7,10-tetra-azacyclododecane-1-glutaric anhydride-4,7,10-triacetic acid
Dox	doxorubicin
DTDTPA	dithiolated DTPA
DTPA	diethylenetriaminepentaacetic acid
DTPADA	diethylenetriaminepentaacetic dianhydride

DU145	human prostate cancer cell line
EDTA	ethylenediaminetetraacetic acid
EL4-luc	murine lymphoma cell line
EMA	European Medicines Agency
EDXS	energy dispersive x-ray spectroscopy
EPR effect	enhanced permeability and retention effect
Eu	Europium element
FBS	fetal bovine serum
FDA	Food and Drug Administration
FITC	fluorescein isothiocyanate
GLP	good laboratory practice
Gy	Gray, unit of applied radiation dose
H358-Luc	human lung cancer cell line
HeLa	human cervical carcinoma cell line
H&E	hematoxylin and eosin
HIFU	high intensity focused ultrasound
HPLC	high performance liquid chromatography
i.v.	intravenous
ICP-MS	inductively coupled plasma mass spectrometry
LGdH	layered gadolinium hydroxychloride
LINAC	linear accelerator
MCF-7	human breast cancer cell line

MDA-MB-231	human breast cancer cell line
miRNA	micro ribonucleic acid
mPGA	modified poly (L-glutamic acid)
MPIOs	micro-sized particles of iron oxide, which have a size larger than 1 $\mu\text{m}$
MR-LINAC	magnetic resonance imaging guided linear accelerator
MRI	magnetic resonance imaging
MTD	maximum tolerated dose
MTT	3-(4,5-Dimethylthiazol-2-yl)-2,5-diphenyltetrazolium bromide
N	normality
NIH	National Institutes of Health
NO. 128A, NO. 132	code names of mPGA candidates
OECD	Organisation for Economic Co-operation and Development
<i>p</i>	<i>p</i> -value in null hypothesis significance testing
PBS	phosphate buffered saline
PC3	human prostate cancer cell line
PDT	photodynamic therapy
PEG	polyethylene glycol
PEGylation	grafting with PEG molecules

PET	positron emission tomography
PFA	paraformaldehyde
PGA	poly (L-glutamic acid)
PI	propidium iodide
PTT	photothermal therapy
R-CH <sub>2</sub>	investigated lipophilic substitutes, R stands for functional groups
REE	rare earth elements
RNase A	bovine pancreatic ribonuclease A
RNU	Rowett nude
SQ20B	human head and neck squamous cell carcinoma cell line
SEM	scanning electron microscope
SPECT	single-photon emission computed tomography
SPIOs	superparamagnetic iron oxide nanoparticles, which have a size larger than 50 nm
T	Tesla
T98G	human glioblastoma cell line
T1 relaxation	longitudinal relaxation
T2 relaxation	transverse relaxation
TE	time to echo

TEM	transmission electron microscope
TLC	thin layer chromatography
TR	repetition time
U-87, U-87MG	human glioblastoma cell line
U.S.	United States
UI penicillin	units of penicillin
UV	Ultraviolet
UV-Vis	Ultraviolet-visible
USPIOs	ultra-small superparamagnetic iron oxide nanoparticles, which have a size smaller than 50 nm
XRD	x-ray powder diffraction
Z	atomic number of a chemical element



## **Chapter 1 – Introduction**

### **Cancer Nanomedicine**

Cancer, a large family of diseases that can occur in any part of the body, is a leading cause of death worldwide and infamous for its complexity and difficulty to be cured.

Traditionally, cancer treatment includes surgery, chemo/drug-therapy, radiotherapy and different combinations of those approaches. However, it is hard to use current regular approaches to treat cancer without harming the healthy tissue, which always causes more problems to patients. Thus, we need novel approaches to treat cancer. Cancer nanomedicine has already attracted intensive research focuses and showed very high potential to conquer challenges in clinical oncology. It may provide an opportunity for finding a novel cancer treatment approach.

Cancer nanomedicines are agents, tools or platforms developed via nanotechnological approaches for use in cancer clinics to gain improved outcomes in the diagnosis and treatment of human cancer diseases.

Nanotechnology commonly refers to techniques and engineering processes conducted at the molecular level, or at the nanometer scale, i.e. at a scale that is smaller than 1 micrometer. The earliest concept of nanomedicine came from Dr. Richard Feynman's visionary idea that nanosized machinery could be introduced into a patient's body to achieve key insights into the patient's illness and then perform a surgery or assist an inadequately functioning organ. The term 'nanomedicine' was established in 1998<sup>1</sup>. Since then, nanotechnologies have been extensively exploited in the medical arena as more and more researchers have recognized the potential of nanomedicine. The emerging field of nanomedicine research merged the field of medicine and the fields of engineering, chemistry, and biology, with the aim of unlocking brand new pathways to diagnosis and treatment of human diseases<sup>2,3</sup>.

Based on unique properties that appear when working at the nanoscale level, cancer nanomedicine is providing new opportunities and showing great potential in the fight against the complexity of cancer diseases<sup>4</sup>. To date, cancer nanomedicine research is the primary focus of nanomedicine studies. There are many innovative nanoscale diagnostic and therapeutic modalities at various stages of research and development, and some have been put to use in clinical cancer care.

Doxil was the first success story regarding the use of nanomedicine in cancer treatment<sup>5,6</sup>, launching the entire field of cancer nanomedicine in 1995. Doxil, a liposomal form of doxorubicin (see the section on Doxorubicin below for more details on this treatment) designed to treat certain types of solid tumour including human breast cancer, was approved for use in clinical treatments by the U.S. FDA (Food and Drug Administration). This early success was due to a unique feature that appears at the nanoscale when working with doxorubicin. The nanosized particles of liposomal doxorubicin are able to take advantage of leaky blood vessels that branch out in solid tumours to promote intratumoural drug accumulation due to the EPR effect (Enhanced Permeability and Retention effect, seen only in solid tumours), which results in an improved drug therapeutic index and improved safety profiles by reducing off-target drug delivery<sup>5,7,8</sup>.

Conventional small molecular drugs, such as doxorubicin, do not naturally distinguish between cancerous and healthy tissues in most cases, leading to unsatisfactory drug biodistribution, adverse side effects, and poor pharmacokinetics<sup>9,10</sup>. Cancer nanomedicines are envisioned as nanosized platforms for delivering drug molecules in a selective way to various types of cancer<sup>11,12</sup>. Cancer medicines are also being viewed as a new way to design medicines targeted towards particular types of cancers, such as specific carcinomas<sup>13-15</sup>. Nanoparticles and

nanosized structures developed via fabrication and encapsulation approaches based on nanotechnology principles generally have demonstrated favorable physicochemical characteristics for one or more specific clinical needs, including improved solubility and stability, targeted and localized delivery, desirable pharmacokinetics, improved disease diagnosis and/or improved disease treatment<sup>2,16</sup>. As an example, Abraxane, a nanoformulation of paclitaxel which is specifically used for advanced stage breast cancer treatment, is a successfully developed cancer nanomedicine that overcame some of the difficulties surrounding treatment with traditional paclitaxel formulations. Paclitaxel itself is a highly lipophilic naturally occurring anticancer treatment, but its insolubility in water makes it unfavorable for pharmaceutical development. However, when paclitaxel was bonded with albumin and produced as protein-bound paclitaxel nanoparticles with a diameter of 130 nm (nanometers), its water solubility, stability, safety and intratumoural accumulation were favorably altered, improving its functionality for use in this application<sup>17</sup>.

The extensive research and development work in the area of cancer nanomedicine<sup>18-20</sup> for more than two decades has paved the way to improved drug biodistribution patterns and pharmacokinetics by providing solutions to circumvent the following commonly occurring obstacles to the use of cancer chemotherapeutic and diagnostic agents: Poor water solubility, rapid systematic clearance, and drug resistance. Due to the versatility of engineered cancer nanomedicines, researchers are now able to precisely guide the biodistribution, site of action, and release of diagnostic and therapeutic agents<sup>21</sup>. Nanomedicine is thus one approach with very high potential to revolutionize both cancer diagnosis and treatment, and the current intensive research in cancer nanomedicine demonstrates that its use is perceived as having the potential to conquer

the ultimate goal of delivering personalized cancer diagnosis and treatment regimens to patients<sup>21-23</sup>.

### **Cancer Nanotheranostics**

In clinical oncology, diagnostics and therapeutics approaches are typically conducted separately. Patients have to undergo the processes separately. Now, we see another research concept has developed as the cancer nanomedicine research field continues to advance: Nanoscale complexes produced for synergistically delivering single agents with both diagnostic and therapeutic purposes. The portmanteau “cancer nanotheranostics” has developed within the past decade<sup>24</sup>. To provide both cancer diagnostic and cancer therapeutic functions, cancer nanotheranostics combine at least one diagnostic and one therapeutic module. The ultimate goal of cancer nanotheranostics is to achieve real-time imaging-guided decision making and optimal focal therapy, followed by similarly-guided post-treatment response management, thereby radically improving clinical outcomes of cancer patients. Any diagnostic tools, including MRI (magnetic resonance imaging), PET (positron emission tomography), CT (computed tomography), SPECT (single-photon emission computed tomography), optical imaging, photoacoustic imaging or ultrasound imaging; and any therapeutic means, including chemotherapy, radiation therapy, immunotherapy, gene therapy, photodynamic therapy, or photothermal therapy, could possibly be combined in cancer nanotheranostics<sup>25</sup>.

Kaida *et al* proposed a single-platform polymeric nanotheranostics carrier for an MRI contrast agent and a chemotherapeutic agent, allowing for MRI-visible delivery of DACHPt ((1,2-diaminocyclohexane)platinum(II)) directed towards a pancreatic tumour model<sup>26</sup>. The polymer micelles developed transported a clinical MRI contrast agent, Gd-DTPA (Gadolinium-

diethylenetriamine pentaacetate), and a drug, DACHPt, in a single polymeric carrier, and allowed for effective mapping of the drug accumulation at tumour sites using MRI.

Another study demonstrated approaches that allowed for delivery of nanoparticles with the simultaneous capabilities of activatable MRI monitoring of intratumoural doxorubicin release, drug-dose painting, and antitumor effects. In the study, Ponce *et al* loaded MnSO<sub>4</sub>, an MRI contrast agent, into temperature-sensitive doxorubicin liposome nanoparticles, and observed the spatial correlation between MRI signal and drug release locations<sup>27</sup>. Before the liposomes were disintegrated, the MRI contrast agent MnSO<sub>4</sub> was caged in the doxorubicin liposomes, with limited access to bulk water, and therefore limited ability to generate MRI signals. Once the release of the liposome payloads was triggered by heat being delivered to the tumour centres, the MRI signal was activated and found to be spatially correlated with doxorubicin release.

Physiologically acidic environments at tumour sites can also be utilized to trigger low-pH-sensitive nanotheranostics. Kaittanis *et al* demonstrated a doxorubicin-loaded Ferumoxytol (an FDA-approved iron oxide nanoparticle coated with dextran for iron deficient patients) nanotheranostic agent for acidic tumour microenvironments. The acidic extracellular environment around the tumour triggered the doxorubicin release and simultaneously unleashed the superparamagnetic property of the iron oxides, which could then be visualized by MRI in real-time. This nanotheranostic worked more efficiently than treatment with free doxorubicin, both *in vitro* and *in vivo*, in terms of inhibition of oncogenic pathways<sup>28</sup>.

In another *in vitro* study reported by Shannon *et al*, anti-miRNA (micro ribonucleic acid) oligonucleotides were loaded into an MRI-traceable gadolinium-based layered double hydroxide nanocarrier for miRNA-10b inhibition in metastatic human breast cancer cells<sup>29</sup>.

Furthermore, external stimuli including various forms of irradiation, heat, or ultrasound can be exploited to guide or activate the functionalities of nanotheranostics<sup>30</sup>. For instance, HIFU (high intensity focused ultrasound) can be employed in temperature-sensitive nanotheranostic platforms as a means of non-invasive heat delivery, which promises to be highly practical in clinical applications<sup>31</sup>. Muhanna *et al* reported a multimodal porphyrin lipoprotein-mimicking nanotheranostic for PET and fluorescence imaging guided surgery, and PDT (photodynamic therapy), for head and neck cancer diagnosis, treatment, and management<sup>32</sup>. PET and intraoperative fluorescence imaging were used to effectively visualize the tumours using the porphyrin lipoprotein-mimicking nanoparticles as imaging agents, as well as to precisely guide PDT for tumour eradication. In a study by Jin *et al*, MRI-guided focal PTT (photothermal therapy) for use against prostate cancer was investigated<sup>33</sup>. The proposed nanotheranostics platform in their study was the use of copper-64 chelated porphyrin nanoparticles for PET and PTT. In a rat prostate cancer model, a tumour-to-normal prostate tissue ratio of 6:1 was achieved and an optical fibre was inserted into the tumour site to deliver PTT with the guidance of MRI. Due to high intratumoural drug accumulation and precisely applied PTT, effective and selective PTT damage to the tumour was achieved, with minimal effect on the surrounding tissues.

Radiation cancer therapy, which is a mainstay in clinical oncology, is highly effective, precisely oriented, and deeply penetrating. Some clinical imaging tools have been integrated with radiation therapy facilities for imaging-guided radiation therapy to improve precision<sup>34,35</sup>. This concept could enable the creation of a number of radiation treatment paradigms. To date, there is still a clinical need for well controlled irradiation dose delivery in terms of location and accuracy within a patient's body. Nanotechnology has great potential for shifting the direction of radiation therapy towards patient specific treatments, including the development of imaging-guided

approaches, that achieve precise and accurate treatment delivery, thus reducing toxicity and enhancing irradiation efficacy<sup>36-39</sup>. Within the field of cancer nanotheranostics, researchers still have plenty of options to explore, as nanotheranostics-mediated radiation therapy enhancement has received relatively little attention to date<sup>24,40</sup>.

One study in this area was performed by Bonvalot *et al*, who reported their first *in vivo* human study of intratumourally injected radiosensitizing hafnium oxide nanoparticles, which substantially enhanced tumour radiotherapy outcomes<sup>41,42</sup>. Phase II/III clinical trials using these hafnium oxide nanoparticles as a way to enhance radiation treatment of adult soft tissue sarcomas by achieving better local control of tumours are underway and are expected to be completed this year (2020)<sup>43</sup>.

In 2004, Hainfeld *et al* first completed *in vivo* research using gold nanoparticles as efficient radiosensitizers in a mouse model, while maintaining a relatively safe *in vivo* profile<sup>37</sup>. Miladi *et al* reported an *in vivo* study of MRI-traceable ultrasmall gold-gadolinium nanocomplexes (Au@DTDTPA-Gd: gadolinium chelate-coated gold nanoparticles; DTDTPA = dithiolated DTPA) with MRI-radiosensitizing properties<sup>44</sup>. They demonstrated a significant radiation enhancement with the use of the Au@DTDTPA-Gd nanocomplexes, and also demonstrated that the nanocomplexes were biocompatible when irradiation was not present. Compared to untreated gliosarcoma-bearing rats, the mean survival time of the irradiation+Au@DTDTPA-Gd nanocomplex-treated rats was increased by 4.7 times, while the irradiation-only treated group's mean survival time was increased by 2.2 times. The opportunity to use MRI data to guide the application of the irradiation treatment was also demonstrated in this study.

## **MRI and MRI Contrast Agents**

Clinical magnetic resonance imaging (MRI) is a medical imaging technique that involves reconstructing highly resolved three dimensional anatomical pictures of scanned areas of the body. MRI is based on measuring the precession — wobbling motion that occurs when a spinning object is the subject of an external force — of water protons (protons of hydrogen atoms, which are naturally abundant in the human body) within an external magnetic field when certain radiofrequency pulses are applied. In the presence of the external magnetic field, water protons can absorb the energy of certain radiofrequencies, which allows them to be excited to a higher spin energy level and then re-emit the radio wave in order to return to the original aligned spin energy state<sup>45</sup>. The re-emitted radiofrequency signals are then detected, encoded, and transformed into graphic information within an MRI facility. The process of water protons returning from an excited state to their equilibrium state is called a relaxation process. The length of time taken for the relaxation process to occur is called the relaxation time. The spin-lattice relaxation, or longitudinal relaxation, time is called the T1 relaxation time, while the spin-spin relaxation, or transverse relaxation, time is called the T2 relaxation time. The relaxation times required to return to the equilibrium state are sensitive to the surrounding environment of the water protons, meaning that water protons in different human tissues or organs have various relaxation times. Images are thus produced based on water proton densities in different tissues and the water proton relaxation rate differences in  $1/T_1$  (longitudinal) or  $1/T_2$  (transverse). Water proton relaxation times from the same tissue type are the same and thereby different tissue types are distinguishable. MRI is one of the most widely performed medical imaging approaches, and is especially useful for finding or pinpointing tumours, and for guiding tumour surgery or radiation therapy<sup>46</sup>.

MRI, however, has its weaknesses, including low sensitivity, which can make it difficult to obtain good contrast between pathological tissues and normal tissues. Paramagnetic compounds, which are metal ions with unpaired electrons (including  $Mn^{2+}$ ,  $Fe^{2+}$ ,  $Fe^{3+}$ ,  $Gd^{3+}$ ) and free radicals, possess unpaired electrons which are able to influence excited water proton spins. A significant reduction in water proton relaxation time can be observed when reorientation of unpaired electrons enables a strong fluctuating magnetic field<sup>45</sup>. Paramagnetic compounds thereby can be utilized to alter water relaxation rates and enhance MRI image contrast for more reliable diagnostic results, and are therefore referred to as magnetic resonance imaging contrast agents<sup>47</sup>. Gadolinium ions (with seven unpaired electrons), manganese ions (with five unpaired electrons) or dysprosium ions (with four unpaired electrons) are commonly used as clinical paramagnetic contrast agents<sup>48</sup>. These paramagnetic contrast agents are also called  $T_1$  or positive contrast agents because they can enhance  $T_1$  relaxation in the target areas and thus produce brighter images.

In most cases, MRI contrast agents are classified as paramagnetic or superparamagnetic contrast agents based on their magnetic properties<sup>49,50</sup>. Superparamagnetic compounds, also known as iron oxides in colloidal form, are iron oxide-composed nanoparticle dispersions with particle sizes of 5 – 200 nm, including USPIOs (ultra-small superparamagnetic iron oxide nanoparticles, which have a size smaller than 50 nm) and SPIOs (superparamagnetic iron oxide nanoparticles, which have a size larger than 50 nm)<sup>51</sup>. There is another type of superparamagnetic iron oxides called MPIOs (micro-sized particles of iron oxide, which have a size larger than 1  $\mu m$ ), but these are not used for intravenous injection and tumour detection due to their large size<sup>52</sup>. USPIOs and SPIOs are ideal for intravenous administration and subsequent detection of pathological changes in the reticuloendothelial system, as they are readily taken up

by the liver, spleen and lymph nodes<sup>53</sup>. Superparamagnetic iron oxide nanoparticles were initially developed as negative contrast agents to enhance T<sub>2</sub> relaxation<sup>54</sup>. In areas where iron oxide nanoparticles accumulate, darkened images are produced as a result of their T<sub>2</sub> enhancement effect. Thus, superparamagnetic iron oxide nanoparticles are also referred to as T<sub>2</sub> contrast agents. More recently developed USPIOs with a size of less than 10 nm have also been reported as positive contrast agents with excellent T<sub>1</sub> enhancement ability<sup>53,55–58</sup>.

Intravenously administered MRI contrast agents enable image contrast enhancement of living tissues that either have a high affinity for the injected contrast agent or are highly vascularized. Tumour tissues are physiologically different from normal tissues and are highly vascularized. The permeable hyper-vascularization in solid tumours results in higher uptake of injected contrast agents, and thereby higher contrast in MRI images. When MRI images are acquired with T<sub>1</sub> contrast agents, this produces positive image contrast, and the resulting image is called a T<sub>1</sub>-weighted image because the MRI signal intensity is increased at the target tissue. T<sub>2</sub>-weighted images, on the other hand, produce negative image contrasts with T<sub>2</sub> contrast agents.

The most widely used intravenous MRI contrast agents are composed of gadolinium (III) chelates, which are also called T<sub>1</sub> or positive contrast agents<sup>45,59</sup>. Gadolinium ions are delivered in a chelated form to ensure their safe use while maintaining their paramagnetism, as there is a risk of patients with severe kidney failure developing a rare nephrogenic systematic fibrosis from using free gadolinium ions. There are two structural classes of gadolinium chelates for clinical MRI: Linear and macrocyclic, which are composed of gadolinium ions chelated with either linear or cyclic polyamino ligands, respectively<sup>60,61</sup>. These paramagnetic contrast agents for MRI are commonly used at a clinical dosage of 0.1 mmol/kg injected intravenously at concentrations of 0.5 or 1 mmol/mL. Currently, there are nine types of gadolinium chelate MRI contrast agents

approved for human use, either by the FDA or EMA (European Medicines Agency): gadobutrol (Gd-DO<sub>3</sub>A-butrol, Gadovist<sup>®</sup>), gadoxetate (Gd-EOB-DTPA, Eovist<sup>®</sup>), gadoversetamide (Gd-DTPA-BMEA, OptiMARK<sup>®</sup>), gadoteridol (Gd-HP-DO<sub>3</sub>A, ProHance<sup>®</sup>), gadopentetate (Gd-DTPA, Magnevist<sup>®</sup>), gadobenate (Gd-BOPTA, MultiHance<sup>®</sup>), gadodiamide (Gd-DTPA-BMA, Omniscan<sup>®</sup>), gadoterate (Gd-DOTA, Dotarem<sup>®</sup>) and gadofosveset (Gd-Ms-325, Ablavar<sup>®</sup>)<sup>49,62,63</sup>.

Most of the current clinically available molecular contrast agents for MRI, however, have low blood circulation half-lives which reduces the acquisition time interval and lowers the likelihood of accumulation at pathological sites<sup>64,65</sup>. This rapid excretion from the body and lack of specificity has limited the usefulness of commercially available MRI contrast agents in making further advances in oncological detection and therapy processes<sup>66</sup>.

Medical MRI facilities allow for powerful and precise measurements for tracing of tumours. When coupled with cancer nanotheranostics, it is possible to use MRI for quantification of the accumulation of nanotheranostics (which could possibly be carrying various other imaging and/or therapeutic modalities, such as chemotherapeutic agents and radiosensitizers) inside tumour tissues and inside the surrounding healthy tissues, before activation of the injected nanotheranostics. This allows doctors to determine the optimal timing for activation of the nanotheranostics (for example, through external irradiation<sup>67</sup>) once the drug administration is complete. This approach to MRI can also be used as part of post-procedure follow-ups and tumour case management, and thus can contribute to the concept of patient-specific therapeutic strategies.

## **Radiation Therapy and Radiosensitization in Cancer Treatment**

Radiation therapy uses high energy ionizing radiation beams to precisely destroy cells (often cancerous), within a targeted pathological site. Accurately applied ionizing radiation can shrink or completely eliminate a tumour by destroying cancerous cells and their DNA, which thus controls or prevents the proliferation of the cancer cells<sup>38</sup>. The damage produced by radiation is caused by ionizing of cancerous cell biomolecules, which are ionized either directly by the applied irradiation or by highly reactive species produced from the ionization of water molecules that is also induced by the applied irradiation<sup>68</sup>. This mechanism is most effective on rapidly proliferating cells. Since cancerous cells are more radiosensitive and tend to divide faster than most normal cells, radiation therapy was introduced for cancer treatment. Compared to other clinical techniques in oncology, radiation therapy is very cost-effective<sup>69</sup>. Radiation therapy, therefore, is extensively applied in cancer treatment. Over half of all cancer patients receive radiation therapy, which can be used either independently or with another treatment such as chemotherapy or surgery, depending on patient-specific situations<sup>70</sup>, to improve therapeutic efficacy and reduce toxicity. Due to its inherent characteristics and mode of action, radiation therapy can be used as the primary tool to eliminate tumours, to shrink tumours in preparation for surgery, to destroy any possible remaining cancerous tissues post-surgery, or to enhance the curative efficacy of cancer chemotherapies.

In radiation oncology, radiosensitization is an intervention which amplifies the antineoplastic effects of applied radiation therapy. Accordingly, radiosensitizers are defined as agents that make cancerous cells more sensitive to radiation therapy. Because radiosensitizers enhance the effectiveness of applied radiation therapy in the area where they are present, their use further improves the selectivity of radiation therapy and thus can spare normal tissues when

radiosensitizers are only present in targeted area. The mechanisms behind how radiosensitizers act are not fully understood yet, but elements with high  $Z$  value (atomic number), including gold ( $Z = 79$ ), platinum ( $Z = 78$ ) and gadolinium ( $Z = 64$ ), have been determined to be efficient radiosensitizers<sup>71-73</sup>. High capture cross sections of high  $Z$  elements can enable the intrinsic therapeutic properties of these heavy metals by elevating radiation deposition in targeted areas and thereby enhancing the therapeutic efficacy of the radiation<sup>68</sup>.

### **Gd and Gd Nanotheranostics**

Gadolinium is a well-known metallic element (atomic number 64, symbol Gd) belonging to the lanthanide series, which are also known as the rare earth elements (REE). Gadolinium-based medical MRI contrast agents were first approved in the 1980s and are currently used at a rate of more than 30 million injections annually, which accounts for about 40% of the MRI investigations performed globally in a year<sup>74,75</sup>. Because gadolinium has seven unpaired electrons and a slow electron spin relaxation, it has the highest relaxation efficiency of all metals<sup>75</sup>. Clinically, gadolinium chelate solutions (such as Gadovist<sup>®</sup>) are the most commonly used paramagnetic medical imaging contrast agents for MRI<sup>49,76</sup>. Using gadolinium chelate formulas instead of pure gadolinium improves its biosafety when introduced into the body, because, as described earlier, the possible toxicities of gadolinium and chelating agents are effectively contained through complexation<sup>77</sup>. Unfortunately, these chelating agents limit not only the toxicity of free gadolinium ions but also the number of surrounding water molecules that are able to interact with single gadolinium ions, which thereby limits gadolinium-induced MRI signal amplification. These gadolinium chelates for MRI, due to their small size as molecular solutions, also have the disadvantages of relatively short blood circulation half-lives

for data acquisition and non-specific biodistribution in tissues<sup>64,65</sup>. This rapid excretion from the body and lack of specificity has limited the use of gadolinium chelated MRI contrast agents in terms of their use in advances in detection and therapy management in oncology<sup>66</sup>.

Rapidly advancing nanoscience and nanomedicine research has suggested that multifunctional nanoparticles could be a better strategy for effectively utilizing the multiple valuable physicochemical features of gadolinium for medical applications. Unlike gold and iron oxide nanoparticles, which also hold great potential for medical applications but have already received a great deal of research attention, gadolinium-based or, more generally, lanthanide-based nanoparticles have received less attention in biomedical research publications in the past. Lanthanide-based nanoplatfoms warrant further study, because lanthanides possess a variety of interesting features that can be utilized for medical monitoring and therapeutic nanoplatfoms. Among the lanthanides, gadolinium is believed to be a very attractive candidate for designing multi-purpose nanocomplexes due to its high Z value ( $Z = 64$ ) and paramagnetism, as described above<sup>24,40,75</sup>. Gadolinium and other lanthanide elements have gained significant interest in biomedical engineering research in the past decade, due to their versatile chemical and physical properties, for the development of a variety of nanotechnology-engineered agents for disease diagnosis, monitoring, and treatment<sup>75,78,79</sup>. Nanocomplexes involving gadolinium have shown great potential in biomedical applications and, in particular, offer unique opportunities in cancer theranostics<sup>40</sup>. Nanocomplexes based on gadolinium chelates, as well as nanocomplexes made of crystalline cores based on gadolinium, have been fabricated and tested for their application to MRI and/or radiosensitization<sup>80-87</sup>. In these reported studies, the grafted gadolinium chelates or gadolinium-based crystalline nanoparticles displayed the potential to significantly enhance MRI image contrast, while at the same time gaining distinct properties due to the nanoformulation

(such as prolonged half-life, distinct biodistributions, and specific excretion pathways). Many of the reported studies were devoted either to image contrast enhancement or multimodal imaging, but research works focused on theranostics applications have started to appear in the published literature, and it is believed that such applications would be cost-effective and hold great clinical potential<sup>88</sup>.

As well as being paramagnetic and having a relatively high  $Z$  value ( $Z=64$ ), gadolinium has a very high neutron cross-section<sup>40</sup>. These properties are the foundation of gadolinium's versatile clinical utility. Neutron-capture therapy with gadolinium, performed mainly in North America and Japan, is another promising example of the use of gadolinium for clinical purposes<sup>89</sup>. Because gadolinium has the ability to increase the sensitivity of surrounding tissues to externally applied irradiation, due to its relatively high  $Z$  value, it can work as an x-ray imaging agent<sup>90,91</sup>. These features are very helpful in the development of multifunctional nanotheranostics platforms for imaging-guided therapy to simultaneously diagnose and treat cancers. Gadolinium nanocomplexes, as with all the nanosized particulates, could be used to exploit the structural abnormalities of tumours, allowing for the accumulation of the nanocomplexes at pathological sites based on the EPR effect described earlier<sup>92</sup>. Since the physicochemical properties of gadolinium nanocomplexes can be optimized for certain non-invasive visualization or therapeutic purposes, as well as delivery requirements of the target location<sup>93-95</sup>, research studies have started to focus on development of multipurpose cancer nanotheranostics incorporating gadolinium.

Among the reported gadolinium-based theranostic nanoplatfroms, crystalline gadolinium oxide nanocomplexes proposed by Bazzi R. *et al* were demonstrated to have great potential based on the following studies from their group. They first reported a reproducible and

controllable way of synthesizing gadolinium oxide nanocomplexes<sup>96,97</sup>. The synthesis of their inorganic crystalline gadolinium oxide nanocomplexes was carried out at 180°C, and the nanosized gadolinium oxide particles were directly precipitated from a mixture of gadolinium chloride and diethylene glycol. The presence of the high viscosity organic solvent diethylene glycol played an important role in size control and preventing aggregation of particles. Following this work, to further increase the colloidal stability of their gadolinium oxide nanocomplexes, they encapsulated them into a polysiloxane shell<sup>98</sup>. Engström *et al* reported surface PEGylation (grafting with polyethylene glycol – PEG – molecules) and confirmed the potential of gadolinium oxide nanocomplexes for use in MRI<sup>99–101</sup>. PEGylation is now a fairly common technique for nanomedicine surface modification, as the PEGylated products can have favorable physiological traits in terms of bioavailability, pharmacokinetics, and biodistribution<sup>102</sup>. The above studies describing gadolinium oxide nanocomplexes did not include *in vivo* results, although the measured MRI enhancement effect of the gadolinium oxide nanocomplexes appeared to be sufficient for the intended purposes.

Following the development of hydrophilic polysiloxane shell-encapsulated gadolinium oxide nanocomplexes, they modified the polysiloxane-coated gadolinium oxide nanoparticle surface with either PEG molecules or DTPADA (diethylenetriaminepentaacetic dianhydride) and performed *in vitro* and *in vivo* evaluation of these gadolinium oxide-based multifunctional nanotheranostics<sup>85,103–106</sup>. Both the Gd-Si-PEG (surface PEGylated gadolinium oxide nanocomplexes) and the Gd-Si-DTPADA (surface DTPADA modified gadolinium oxide nanocomplexes in a polysiloxane shell) were non-toxic as tested *in vitro*, and were able to act as x-ray imaging and MRI contrast agents because of the gadolinium<sup>85,104</sup>. The Gd-Si-PEG nanocomplexes were further demonstrated to provide excellent irradiation enhancement of

neutron capture therapy (which involves using the irradiation of neutrons to treat tumours) in the murine lymphoma cell line EL4-luc<sup>85</sup>. The *in vivo* biodistribution and pharmacokinetic profiles of Gd-Si-PEG nanocomplexes were determined to be favorable, and could be altered by adjusting the chain length and chain tip group of the PEG molecules grafted on the surface of the nanocomplexes<sup>106</sup>. The Gd-Si-PEG nanocomplexes using a short chain PEG with carboxyl groups on the chain tips did not accumulate in the liver, spleen, and lungs prior to being eliminated from the animal body through the renal pathway, which indicated the *in vivo* safety of the Gd-Si-PEG nanocomplexes when administered intravenously in a mouse model. These results suggested that the Gd-Si-PEG nanocomplexes may have the potential for use in imaging-guided neutron capture therapy. In the study of the Gd-Si-DTPADA nanocomplexes<sup>104</sup>, a maximum radiation enhancement effect was observed in radioresistant human glioblastoma U87 cells when they were incubated with Gd-Si-DTPADA nanocomplexes at a gadolinium concentration of 0.5 mM and 10 Gy (Gray, unit of applied radiation dose) of x-ray irradiation was applied. This suggested the feasibility of applying gadolinium oxide nanocomplexes for imaging-guided radiation enhanced therapy *in vivo*. Cells treated with Gd-Si-DTPADA nanocomplexes at a higher concentration, coupled with the same dose of x-ray irradiation, resulted in a higher survival rate of the cancer cells, which was attributed to the aggregation of Gd-Si-DTPADA nanocomplexes limiting the interaction efficacy between the applied irradiation and the Gd-Si-DTPADA nanocomplexes. The *in vivo* behavior of Gd-Si-DTPADA nanocomplexes was similar to the Gd-Si-PEG nanocomplexes - they did not accumulate in the liver, spleen, and lungs prior to being eliminated from the animals' bodies through the renal pathway<sup>103,107</sup>. The Gd-Si-DTPADA nanocomplexes injected in gliosarcoma (murine brain tumour) bearing rats exhibited an accumulation in the region of the gliosarcoma, which was

attributed to the EPR effect within the tumour. Thanks to the improved image contrast by the Gd-Si-DTPADA nanocomplexes present at the tumour region, the tumour was visualized by MRI with sufficient image contrast to be detectable by the human eye. In their subsequent *in vivo* study of Gd-Si-DTPADA nanocomplexes-induced radiosensitization in a 9 L gliosarcoma murine brain tumour-bearing rat model, they compared the therapeutic results from three different treatment groups and the untreated control group<sup>105</sup>. Compared with the control group, the x-ray treatment applied five minutes after Gd-Si-DTPADA injection (i.v. - intravenous) resulted in a 78% increase in life span; the x-ray-only treated group had a 147% increase in life span; and the x-ray treatment applied 20 minutes after Gd-Si-DTPADA injection (i.v.) resulted in a 373% increase of life span. This remarkable life span increase, achieved by combined treatment with x-ray radiation and Gd-Si-DTPADA nanocomplexes, was attributed to the radiosensitization effect of the injected Gd-Si-DTPADA nanocomplexes accumulated in the gliosarcoma. It is important to note that, in the combined treatment, when the x-ray was applied five minutes post-injection, the therapeutic effect was even worse than the x-ray only treated group. The reason, as deduced by the authors, was that the injected Gd-Si-DTPADA nanocomplexes distributed in the rat brain had not yet been eliminated from the brain at five minutes post-injection, which led to a radiosensitization effect in the normal brain tissue as well as the target tissue. In contrast, 20 minutes after injection, most of the Gd-Si-DTPADA nanocomplexes had been eliminated from the healthy brain tissues, while the quantity of Gd-Si-DTPADA nanocomplexes retained in the tumour was still high, thus sparing the healthy tissue and enhancing the intratumoural radiation therapeutic efficacy. In this case, therefore, the clearance of injected nanocomplexes from healthy tissue prior to irradiation was crucial, as the presence of radiosensitizing nanocomplexes could exert unwanted damage on the healthy

tissue<sup>105</sup>. These studies also showed that the paramagnetism of gadolinium-based nanocomplexes was an important asset, as, with their use, MRI could be used to guide the irradiation, allowing the radiation to be applied at the most suitable moment and location.

This study confirmed the feasibility of applying these biocompatible gadolinium-based nanocomplexes as theranostic agents (in this case, combining dose enhancement of x-ray irradiation and image contrast enhancement of MRI) to *in vivo* cancer treatment studies. These results indicated that it might be possible to use these nanocomplexes for real-time imaging-guided radiation cancer therapy, and thus paved the way toward patient-specific therapy.

Since radiation therapy relies heavily on imaging, clinical strategies have already included MRI as a part of personalized cancer radiation therapy, assessment of cancer responses to the applied radiation dose, and post-treatment management<sup>34</sup>. Furthermore, the idea of merging the radiotherapeutic capability of a linear accelerator (LINAC) with the visualizing capability of an MRI instrument (MR-LINAC – Magnetic Resonance Imaging Guided Linear Accelerator) has become a reality very recently. The first patient in Canada to be treated with MR-LINAC was treated in August 2019 at Sunnybrook Health Sciences Centre for a glioblastoma. Radiation oncologists now can monitor radiation beam movement in the body in real time with MRI. This allows doctors to precisely orient and deliver irradiation to a targeted area and spare the surrounding healthy tissues. Without MR-LINAC, determining the location for delivery of irradiation is commonly based on estimation and marks drawn on the patient's body during the imaging process prior to the beginning of the radiation treatment. For strategic therapies, such as the use of MR-LINAC in combination with radiation, to become part of regular practice, there will be a need to develop novel agents that can perform both as imaging

contrast agents and radiosensitizers. The successful development of such novel multi-role agents could thereby significantly advance this field of therapy.

Another successful example of gadolinium-based cancer nanotheranostics is AGuIX<sup>®</sup><sup>108,109</sup>. AGuIX<sup>®</sup> is a type of ultra-small (~3 nm diameter) theranostic nanocomplex that is made of polysiloxane cores grafted with gadolinium chelates (Gd-DOTAGA (1,4,7,10-tetra-azacyclododecane-1-glutaric anhydride-4,7,10-triacetic acid)), which actually could be viewed as an upgraded version of the previously described theranostic Gd-Si-DTPADA nanocomplexes<sup>109,110</sup>. The synthesis process described to make AGuIX<sup>®</sup> was similar to the synthesis of Gd-Si-DTPADA nanocomplexes, except that the gadolinium oxide cores were then dissolved, and the dissociated gadolinium ions became conjugated with the grafted DOTAGA molecules<sup>111</sup>. After the cores' dissociation, the hollow polysiloxane spheres left behind further broke down into smaller fragments which still possessed all the physicochemical properties of the initial nanostructures. Based on the success of Gd-Si-DTPADA nanocomplexes, AGuIX<sup>®</sup> was developed to have a high gadolinium content and thus demonstrated a high T<sub>1</sub> contrast enhancement for MRI and an impressive radiosensitizing effect. The research group has recently reported phase 1 clinical trials of AGuIX<sup>®</sup> targeting brain metastases<sup>108</sup> and is ready to start their phase 2 clinical trial on AGuIX<sup>®</sup> (NANORAD2, NCT03818386)<sup>112</sup> based on the positive outcomes from phase 1. Before they filed to start the phase 1 trial, many *in vitro* and *in vivo* validation and safety tests were carried out on AGuIX<sup>®</sup> nanocomplexes<sup>87,104,109,111,113–118,119–123</sup>.

High dose enhancement fractions and sensitivity enhancement ratios have been observed in *in vitro* studies against glioblastoma cells (U-87MG and T98G), head and neck squamous cell carcinoma cells (SQ20B), melanoma cells (B16F10), prostate cells (DU145 and PC3) and cervical carcinoma cells (HeLa) with AGuIX<sup>®</sup><sup>67</sup>. *In vivo* animal studies have achieved tumour

volume reductions and increased life span and survival rate of the animals. In particular, in a study using a glioblastoma model, AGuIX<sup>®</sup> efficiently accumulated in the tumours within the first minute after the injection was performed, as verified by MRI, and the signal was still detectable 24 hours post-injection, which was attributed to the EPR effect present in the tumours<sup>109,111</sup>. Irradiation was applied post-injection at a time, selected based on the MRI results, when the difference in AGuIX<sup>®</sup> distribution between health tissues and pathological tissues was maximized, thereby resulting in optimal tumour selectivity.

The AGuIX<sup>®</sup> was also administered via the airways into H358-Luc lung tumour-bearing mice in a study on its impact on both MRI of lung tumours and radiosensitization<sup>123</sup>. This was the first time that using a nanocomplexes-based positive MRI contrast agent for lung imaging was reported. The radiotherapy was applied 24 hours post-injection. A life span increase of 45% was observed in the irradiation+AGuIX<sup>®</sup> treated mice.

MRI and radiosensitization studies were also carried out in a mouse pancreatic xenograft model, which demonstrated the effectiveness of AGuIX<sup>®</sup><sup>116</sup>. Studies were then performed in cynomolgus monkeys, which showed that the AGuIX<sup>®</sup> was non-toxic *in vivo* and had imaging-guidance potential. After the completion of this study, they filed for the phase 1 clinical trial<sup>108,109,117</sup>.

In their Phase I clinical trial in patients with multiple brain metastases<sup>124</sup>, a single intravenous infusion of AGuIX at doses of  $\leq 100$  mg/kg was well tolerated by all patients when combined with whole brain radiation therapy (30 Gy in 10 fractions). Injection of AGuIX showed MRI contrast enhancement in brain metastases 2h post-injection, while healthy brain tissues had no MRI enhancement observed under the same conditions. This enhancement effect in brain metastases lasted for up to 8 days. A Phase II trial is under way.

Meanwhile, the same research group went on to demonstrate the MRI-guided radiosensitization efficacy of AGuIX in 9L glioma brain tumour-bearing rats using a clinical 1.0 Tesla MRI-LINAC<sup>125</sup> and established a workflow for using AGuIX with MRI-LINAC.

In the study by Wu *et al*<sup>126</sup>, gadolinium oxide nanoparticles using hyaluronic acid as a surface modification material (HA-Gd<sub>2</sub>O<sub>3</sub> NPs) for MRI-radiosensitization were fabricated. These HA-Gd<sub>2</sub>O<sub>3</sub> NPs were prepared via a hydrothermal approach and had an average size of 105 nm. An *in vitro* study showed that the HA-Gd<sub>2</sub>O<sub>3</sub> NPs had no obvious cytotoxicity against human hepatocarcinoma cells (HepG2) and vascular smooth muscle cells (VSMC) at the highest tested dose (200 µg/mL). As well, no histological change or inflammatory response was observed 1 week after HA-Gd<sub>2</sub>O<sub>3</sub> NPs were injected into mice intravenously. The HA-Gd<sub>2</sub>O<sub>3</sub> NPs outperformed their commercial counterpart, Magnevist, in terms of *in vitro* MRI enhancement effect, with an almost doubled *r1* value. An *in vivo* study showed intravenously injected HA-Gd<sub>2</sub>O<sub>3</sub> NPs had an early accumulation in kidneys and bladder, occurring 10 minutes post-injection and thereby enhancing MRI contrast in these areas. This enhancement occurred for up to 60 minutes in mice post-injection, which outperformed Gd complex small molecules (Magnevist). Intravenously injected HA-Gd<sub>2</sub>O<sub>3</sub> NPs also enhanced MRI contrast in the area of a subcutaneous liver tumor xenograft mouse model. In tumour-bearing mice, HA-Gd<sub>2</sub>O<sub>3</sub> NPs combined with radiation exhibited a radiosensitization effect by suppressed tumour growth by ~20% compared with the radiation-only treated group, in terms of tumour volume.

Another interesting nanotheranostic system incorporating both gadolinium and iron was reported by Qin *et al*<sup>127</sup>. Using a metal-catechol coordination assembly process, they integrated gadolinium and iron as MRI diagnostic and photothermal therapeutic components, respectively, into polymer nanoparticles, creating a bimetal phenolic coordination polymer nanosystem. These

Gd/Fe metal phenolic coordination polymer nanoparticles (Gd/Fe-MPCPs) exhibited a higher *in vitro* MRI contrast enhancement effect compared with Magnevist. An *in vivo* MRI study of EMT-6 tumour-bearing mice showed that Gd/Fe-MPCPs increased the image contrast at the tumour site, with the highest image contrast being observed 4 hours post-injection. Significant inhibition of tumour growth was observed in the presence of Gd/Fe-MPCPs in the photothermal therapy group, compared with non-Gd/Fe-MPCPs treated groups.

More recently, Memona *et al* synthesized PEG-functionalized bimetal Gd-Au nanorods with Dox loaded either inside (Dox-In-Gd-AuNRs) or outside (Dox-On-Gd-AuNRs) the nanorods<sup>128</sup>. Gold salt was chelated with Dox, PEG and gadolinium salt to form this new nanosystem. Physicochemical properties of these nanorods were extensively characterized, and the results demonstrated their potential for use as a combined MRI contrast agent and photothermal therapeutic agent with added Dox chemotherapy.

Xia *et al* reported the development of gadolinium-based porphyrin metal-organic framework nanosheets (PPF-Gd NSs, 2D nanomaterial) with an ultra-high Dox loading capacity for tumour multimodal (MRI and fluorescence) imaging and pH-responsive Dox release<sup>129</sup>. This porphyrin paddlewheel Gd metal-organic framework (PPF-Gd/Dox) adsorbed large quantities of Dox molecules onto its porous structure and reached a loading capacity of over 1500%. A low pH environment (pH 5.5) triggered the release of Dox and 72% of the loaded drug was released over 96h. In contrast, a neutral environment (pH 7.4) only resulted in a release of 24% of the loaded drug over 96h. After being subcutaneously injected next to the tumour site in an A375 tumour-bearing mouse, PPF-Gd NSs gradually diffused inside the tumour tissue over the course of 24h and the highest fluorescence signal was subsequently observed at 72h. Intravenously injected PPF-Gd NSs accumulated inside the tumour and showed obvious fluorescence signals

72h post-injection. Strong MRI signals were observed 6h after an I.V. injection of PPF-Gd NSs. Strong MRI contrast enhancement was still detected 6h after an intratumoural injection of PPF-Gd NSs. Next, PPF-Gd/Dox was used to treat A375 tumour-bearing mice. As compared with the Dox treated group, for which a body weight loss effect caused by free Dox was measured, PPF-Gd/Dox treatment showed a higher tumour growth suppression efficacy without body weight loss. This was attributed to the biocompatibility, combined with the high Dox loading capacity, of the PPF-Gd/Dox NSs.

### **Doxorubicin**

Doxorubicin (Dox) is a member of the anthracycline antibiotics. It is a chemotherapeutic anti-cancer drug that was initially discovered to be made by a non-wild subspecies of *Streptomyces peucetius* (*Streptomyces peucetius* varietas *caesius*)<sup>130,131</sup>. Clinically, doxorubicin is commonly administered intravenously, either alone or with other approved antineoplastic agents, to treat human cancers including breast carcinoma, acute lymphoblastic and myeloblastic leukemias, soft tissue sarcomas, bronchogenic carcinoma, gynecologic carcinomas, testicular carcinoma, squamous cell carcinoma of the head and neck, and gastric carcinoma<sup>132</sup>. The antineoplastic activity of doxorubicin is currently attributed to its interaction with the DNA of target cells. There are two well-recognized mechanisms for this antineoplastic action: Doxorubicin molecules intercalating in double stranded DNA minor grooves; and doxorubicin causing the generation of reactive radicals, resulting in damage to ribose, DNA strands, and cell membranes<sup>133–135</sup>.

Doxorubicin, although currently the most effective anticancer chemotherapeutic agent available, is still limited by its off-target cardiotoxicity, resulting in a fairly narrow therapeutic

window, as well as the drug resistance developed to it in some sophisticated cases<sup>136,137</sup>.

Researchers have made extensive attempts to create various nanoplatfoms to overcome these limitations and improve the therapeutic effect of Dox. The favorable performance of clinically approved Dox nano-formulations demonstrates that nanoplatfom-mediated drug delivery is a great alternative to conventional methods of drug administration<sup>138,139</sup>.

Doxorubicin and adriamycin, another one of the anthracycline antibiotics, naturally form drug-metal complexes with paramagnetic lanthanide elements in aqueous solutions<sup>140,141</sup>.

Although the drug-metal interaction between gadolinium ions and doxorubicin molecules, to the knowledge of the author, has not been previously studied, the binding sites and mechanism are anticipated to be the same as those described in the literature for other paramagnetic lanthanide ions interacting with doxorubicin molecules<sup>140-142</sup>. It was hypothesized in this thesis that this mechanism to form drug-metal complexes could be exploited to synthesize coprecipitated amorphous Gd:Mn-Dox nanospheres. Manganese (Mn), a transition metal which enhances MRI signals, seems to play an important role in the interaction between doxorubicin and DNA<sup>142-144</sup>, and therefore is a desirable dopant in these nanospheres. This drug-metal interaction theory is one of the fundamental theories behind the design of this thesis.

### **Previous Gadolinium-Based Nanocomplex Research by This Group**

*Gadolinium-Layered Nanocomplexes for Anti-miRNA Oligonucleotide Delivery in Human Breast Cancer Cells and Magnetic Resonance Imaging*

Previously in this lab, a novel and biocompatible layered gadolinium hydroxylchloride (LGdH) nanostructure was developed and reported as an MRI-traceable delivery platform for microRNA therapeutics against miRNA-10b in metastatic human breast cancer cells<sup>29</sup>. The

structure of these LGdH nanocomplexes is similar to layered double hydroxides<sup>145</sup> and consists of positively charged gadolinium hydroxide layers with exchangeable chloride ions and water in interlayer spaces. The payload (anti-miRNA oligonucleotides effective against miRNA-10b) was loaded within the interlayer spaces via an ion exchange process. Good cellular uptake and miRNA-10b inhibition effects were observed *in vitro*. The MRI traceability of these structures was verified by T1-weighted MRI in aqueous solution.

Although the layered gadolinium hydroxide nanocomplexes demonstrated some great characteristics, the loading mechanism limited the drug loading capacity of the nanocomplexes, and weak interactions between the drug molecules and the matrix resulted in the premature release of Dox.

#### *Gadolinium-Dox Nanorod Complexes for Doxorubicin Delivery and Simultaneous MRI-Radiosensitization*

Recently, a new type of gadolinium hydroxide nanorods were developed and reported as an MRI traceable delivery platform for doxorubicin used in radiation conjugate therapy against human breast cancer cells<sup>83</sup>. These multifunctional nanocomplexes were synthesized through single-step, efficient, and environmentally friendly wet-chemical methods. The final nanocomplexes (Gd(OH)<sub>3</sub>:Mn-Dox) were composed of Gd(OH)<sub>3</sub> (gadolinium hydroxide) nanorods doped with Mn and loaded with 7.85wt% Dox. Compared with the LGdH nanocomplexes, these gadolinium-Dox nanorod complexes were an improvement, due to the formation of stable interactions between Dox molecules and the nanorod matrix. This resulted in a higher Dox loading capacity, while increasing the sensitivity of surrounding cells towards applied irradiation. Positive *in vitro* outcomes were measured in terms of the cellular uptake, anticancer efficacy and radio-sensitizing functions, confirming that the design could be effective.

The radiosensitizing effect of the synthesized gadolinium-based nanoparticles was observed in a clonogenic experiment. In the Gd(OH)<sub>3</sub>:Mn+radiation treated groups, the cancer cells' reproductive ability was appreciably inhibited, by 52.1% and 54.7%, at concentrations of 30 and 75 µg/mL Gd(OH)<sub>3</sub>:Mn, respectively, compared to the radiation-only and Gd(OH)<sub>3</sub>:Mn-only groups' outcomes. A pilot *in vivo* biodistribution study was carried out on a tumour-bearing rat model, and approximately half of the injected dose was retained in the rat body after 24 hours, with the most significant site of accumulation of the dose being in the spleen, followed by the lungs and liver. Gadolinium content detected in the tumor suggested successful tumor penetration and retention of the Gd(OH)<sub>3</sub>:Mn-Dox nanocomplexes, with no observable adverse effects at the tested dose.

This newly developed nanostructure had its own limitations. Although it had a suppressed burst payload release when compared with the LGdH platform, it was not perfectly suppressed. The payload release period was fairly long, which is possibly because the payload release rate was limited by a slow dissolution rate of the crystalline matrix.

Nanoparticles' *in vivo* performance is also affected by other factors<sup>146</sup>. Once nanoparticles are injected into the blood circulation, particles with sizes smaller than 6 nm will be rapidly cleared from circulation through renal clearance. Those with sizes over 200 nm will be cleared out by the reticuloendothelial system. To design nanoparticles to stay in blood circulation, the nanoparticles' sizes should be greater than the diameter (6-12 nm) of normal blood vessels. Different shapes/morphologies of nanoparticles also affect particles' tumour internalization, but the results in the published literature on this topic are currently a source of debate<sup>146</sup>. Some researchers have reported that rod-shaped nanoparticles worked better than other types, whereas others have found there was better internalization of spherical nanoparticles. The

surface coatings of materials also play an important role in how nanoparticles travel in the blood circulation. For example, polyethylene glycol (PEG) is one of the most popular surface coating materials that has been used for improving solubility, reducing clearance by the reticuloendothelial system and prolonging life time in circulation. The potential downside of using PEG is its immunogenicity, as was reviewed recently<sup>147</sup>. Antibodies against PEG are likely produced in response to the first injection of PEG-coated particles, which will then increase the clearance of PEG-coated particles in subsequent injections.

Taking into consideration all of these factors, it is unlikely that it will be possible to have one ideal design that contains all desired features. Thus “smart” designs of transformable nanoplatfroms could be a good strategy to obtain all the features of an ideal nanoparticle. An example of this would be a nanoplatfrom that can transform its surface characteristics once it comes into close contact with cancer cells at tumour sites, to further improve cellular uptake.

## **Purpose**

This thesis continues exploration in regards to the fabrication and investigation of newly synthesized gadolinium-based cancer theranostic nanoparticles with applications in simultaneous delivery of doxorubicin and MRI-radiosensitization agents that can be activated by external irradiation with extreme precision. The goal of this work is to seek out a novel and much more effective nanoplatfrom for coordinating diagnosis and therapy to address the needs of individual patients. The hypothesis of this thesis work is: An amorphous doxorubicin-loaded gadolinium-based nanocomplex doped with manganese can be synthesized through a hydrothermal homogeneous precipitation process. After surface modification with a modified poly-glutamic acid, this nanosystem can be triggered by external x-ray irradiation in combination with a low pH

environment to release its load, and thus to act as a combined doxorubicin delivery platform and MRI-radiosensitization agent that could be used in the targeted treatment of human breast cancer.

## Thesis Outline

Chapter 1 describes the overall background and scope of this work.

Chapter 2 describes the fabrication of  $\text{Gd}(\text{OH})_3$ ,  $\text{Gd}(\text{OH})_3:\text{Mn}$  nanorods and  $\text{Gd}(\text{OH})_3:\text{Mn}$ -Dox nanocomplexes, along with their characterization, as published in “Fabrication and *in vitro* characterization of gadolinium-based nanoclusters for simultaneous drug delivery and radiation enhancement”<sup>83</sup>. These multifunctional nanocomplexes were synthesized through single-step, efficient, and environmentally friendly wet-chemical methods. The final nanocomplexes ( $\text{Gd}(\text{OH})_3:\text{Mn}$ -Dox) are composed of  $\text{Gd}(\text{OH})_3$  (gadolinium hydroxide) nanorods doped with Mn (manganese) and loaded with Dox. The fabrication started with the synthesis of the basic and Mn-doped  $\text{Gd}(\text{OH})_3$  nanorods, followed by Dox loading to form the final  $\text{Gd}(\text{OH})_3:\text{Mn}$ -Dox nanocomplex. Mn was introduced into the design as a dopant because the high magnetic moment and relaxation efficiency of manganese can be exploited to further enhance MRI signals<sup>143,144</sup>. As a proof of concept, the cellular uptake, anticancer efficacy, and radio-sensitizing functions were assessed *in vitro*. A pilot *in vivo* biodistribution study was carried out on a tumour-bearing rat model to gain a basic understanding of the *in vivo* behavior of the injected nanocomplexes.

Chapter 3 describes the synthesis of amorphous Mn-doped Gd:Mn nanospheres, together with the development of Dox-loaded (Gd:Mn-Dox) and surface modified (mPGA@Gd:Mn-Dox) forms of these nanospheres. A hydrothermal homogeneous coprecipitation method was adapted to produce amorphous and size-controlled spherical nanoparticles. Unlike the crystalline

Gd(OH)<sub>3</sub>:Mn-Dox nanocomplexes described in Chapter 2, these spherical Gd:Mn and Gd:Mn-Dox nanoparticles were amorphous solids, which may have a shorter payload release time relative to their crystalline counterparts. The simple synthesis method described in this chapter resulted in the production of doxorubicin-loaded manganese-doped gadolinium nanospheres possessing a higher drug loading capacity than the nanorod complexes fabricated with the same components in Chapter 2. The main advantages of the method described in this chapter are good scale-up potential and ease of manufacture, without the introduction of harmful ingredients or procedures<sup>148,149</sup>.

Chapter 4 describes the *in vitro* characterization of the multifunctional properties of gadolinium-based nanocomplexes developed in Chapter 3. *In vitro* measurements and experiments were carried out to characterize Gd:Mn, mPGA@Gd:Mn, Gd:Mn-Dox, and mPGA@Gd:Mn-Dox nanospheres. The fabricated Gd:Mn and Gd:Mn-Dox nanospheres were subject to x-ray powder diffraction (XRD) and Energy Dispersive X-ray Spectroscopy (EDXS) for crystalline structure and elemental analysis, respectively. Ultraviolet-visible (UV-Vis) spectroscopy was used to monitor changes during the reaction process for the synthesis of Gd:Mn-Dox nanospheres. Irradiation-activated mPGA disintegration was assessed by measuring the absorbance changes in mPGA solutions before and after irradiation treatments using UV-Vis spectroscopy. The feasibility of irradiation-activated low-pH-responsive doxorubicin release from mPGA@Gd:Mn-Dox nanocomplexes was investigated by measuring the doxorubicin cumulative release profile of radiation-treated mPGA@Gd:Mn-Dox nanocomplex samples in an acidic release medium. TEM, confocal microscopy and ICP-MS were employed to assess the *in vitro* cellular uptake of these nanocomplexes by human breast cancer cells. MTT and clonogenic assays were used for evaluating the synergistic anticancer efficacy of gadolinium and

doxorubicin incorporated in the nanocomplexes. Flow cytometry was used to assess the apoptosis rate induced by the doxorubicin-loaded nanocomplexes in human breast cancer cells. The *in vitro* MRI traceability of doxorubicin-loaded and unloaded nanocomplexes was also explored via testing in clinical MRI and PET-MRI facilities.

Chapter 5 describes the *in vivo* characterization of the multifunctional properties of the gadolinium-based nanocomplexes developed in Chapter 3. The *in vivo* biodistribution profile, acute toxicity, and MRI contrast enhancement of the proposed theranostic nanocomplexes were studied in an immunodeficient rat model. The rats tolerated the injected doses well and accumulated the injected nanocomplexes mainly in the liver, lungs and spleen. This was different from the biodistribution of the rod-shaped nanocomplexes described in Chapter 2, where the spleen accumulated a much larger quantity of the test material relative to the other organs that were analyzed.

Chapter 6 describes the conclusions resulting from this work, the limitations of these studies, and recommended future research directions.

## Chapter 2 – Manufacture of Gadolinium-Based Nanocomplexes

### Introduction<sup>1</sup>

Gadolinium, as one of the well-known lanthanide elements, has drawn significant research interest in biomedical engineering. Due to their versatile chemical and physical properties, gadolinium and other lanthanide elements have been widely studied for development of a variety of nanotechnology-engineered agents for disease diagnosis, monitoring, and treatment in the past decade<sup>78,150,151</sup>. Nanocomplexes involving gadolinium have shown great potential in biomedical applications and, in particular, offer unique opportunities in cancer theranostics<sup>67</sup>.

Gadolinium possesses paramagnetic properties, a relatively high Z value ( $Z=64$ ) and a very high neutron cross-section<sup>67</sup>. These properties are the foundation of gadolinium's versatile clinical utility. Clinically, gadolinium has been used worldwide as a T<sub>1</sub> contrast enhancing agent for patient magnetic resonance imaging (MRI), particularly in cancer detection and management<sup>152,153</sup>. Neutron-capture therapy with gadolinium, performed mainly in North America and Japan, is another promising example of the use of gadolinium for clinical purposes<sup>154</sup>. Due to its relatively high Z value, gadolinium has the ability to increase the sensitivity of surrounding tissues to externally applied irradiation and work as an x-ray imaging agent<sup>155,156</sup>. All these important features are very helpful in the development of multifunctional nanotechnology platforms to diagnose and treat cancers. Gadolinium nanocomplexes, as with all the nanosized particulates, could be used by exploiting the structural abnormalities of tumours to accumulate the nanocomplexes at pathological sites based on the enhanced permeability and retention (EPR) effect. Since the physicochemical properties of gadolinium nanocomplexes can

---

<sup>1</sup> Portions of this chapter were published in: Yoo *et al.* 2016, *Nanotechnology* 27:385104 (14pp).

be optimized to meet certain non-invasive visualization or therapeutic purposes and delivery requirements of the target location<sup>152,157,158</sup>, many research studies have been focused on development of multipurpose cancer nanotheranostics incorporating gadolinium.

Previously, layered gadolinium-based nanoparticles were developed as a novel MRI traceable delivery platform for microRNA therapeutics<sup>159</sup>. In this chapter, the possibility of fabricating gadolinium-based MRI-traceable nanocomplexes for Dox (doxorubicin) delivery and radiation therapy efficacy enhancement was explored. Dox, although the most effectively used anticancer chemotherapeutic agent, is still limited by its off-target cardiotoxicity resulting in a fairly narrow therapeutic window, and the drug resistance developed in some sophisticated cases<sup>136,160</sup>. Researchers have made extensive attempts to make various nanoplatforms to overcome these limitations and improve the therapeutic effect of Dox. The favorable performance of clinically approved Dox nano-formulations demonstrates that nanoplatform-mediated drug delivery is a great alternative to conventional methods of drug administration<sup>161,162</sup>. Given its advantageous characteristics for use in diagnostic and therapeutic purposes, gadolinium-containing nanocomplexes have been extensively studied as image-enhancing agents, with only a few studies of gadolinium-based nanocomplexes proposing their use as drug delivery systems. In one such study, a layered gadolinium hydroxide nanocomplex was reported as a drug carrier in which drug molecules were intercalated through a simple ion exchange process<sup>163</sup>. Mesoporous gadolinium oxide nanorods<sup>164</sup> and nanospheres<sup>165</sup> doped with  $\text{Eu}^{3+}$  were developed with drug loading capacities of 3.5wt% of Camptothecin and Dox, similar to the loading capacity seen with the layered gadolinium hydroxide nanocomplex. Although the layered gadolinium hydroxide nanocomplex has demonstrated some great characteristics, the loading mechanism limited its drug loading capacity and the weak interaction between drug

molecules and the matrix resulted in the premature release of Dox. Here in this chapter, an MRI traceable gadolinium-based nanorods platform is described which could circumvent these deficiencies by forming a stable interaction between Dox molecules and the matrix, with a high Dox loading capacity, while increasing the sensitivity of surrounding cells towards applied irradiations. This provides the opportunity to incorporate all of the above-described benefits into a single nanocomplex that can be synthesized with great ease.

This chapter mainly describes the fabrication of  $\text{Gd}(\text{OH})_3$ ,  $\text{Gd}(\text{OH})_3:\text{Mn}$  nanorods and  $\text{Gd}(\text{OH})_3:\text{Mn-Dox}$  nanocomplexes, and their characterization. These multifunctional nanocomplexes were synthesized through single-step, efficient and environmentally friendly wet-chemical methods. The final nanocomplexes ( $\text{Gd}(\text{OH})_3:\text{Mn-Dox}$ ) are composed of  $\text{Gd}(\text{OH})_3$  (gadolinium hydroxide) nanorods doped with Mn (manganese) and loaded with 7.85wt% Dox. The fabrication started with the synthesis of the basic and Mn-doped  $\text{Gd}(\text{OH})_3$  nanorods, followed by Dox loading to form the final product - the  $\text{Gd}(\text{OH})_3:\text{Mn-Dox}$  nanocomplex.  $\text{Gd}(\text{OH})_3$  nanorods were previously reported to be biocompatible both *in vitro* and long term *in vivo* as a novel MRI contrast agent which promoted a higher  $T_1$  relaxation rate over the conventional gadolinium contrast agent Magnevist<sup>166-168</sup>. All these features, together with the added benefit of being able to exploit the EPR effect to achieve a passive target at the pathological site, make  $\text{Gd}(\text{OH})_3$  nanorods an ideal candidate for clinical applications. Mn was introduced into the design as a dopant as the high magnetic moment and relaxation efficiency of manganese can be exploited to further enhance MRI signals<sup>169,170</sup>. Mn together with Gd are able to chelate with Dox molecules and therefore form a thermodynamically stable complex<sup>171-174</sup>. In this chapter, the feasibility of creating a single phase  $\text{Gd}(\text{OH})_3$  was demonstrated using our single-step synthesis procedure. The synthesized products were characterized by TEM

(transmission electron microscope) and SEM (scanning electron microscope). The morphological changes of the synthesized nanorods were observed step by step when Mn was introduced, as well as upon the addition of both Mn and Dox to the reaction solution. The hexagonal crystal structure of Gd(OH)<sub>3</sub> in the final products was confirmed using XRD (x-ray powder diffraction)<sup>175</sup>. A loading mechanism of Dox was also deduced. As a proof of concept, the cellular uptake, anticancer efficacy and radio-sensitizing functions were assessed *in vitro*. A pilot *in vivo* biodistribution study was carried out on a tumour bearing rat model to give a rough idea of the *in vivo* behavior of the injected nanocomplexes.

Lastly, the work in this chapter led to the fabrication of a novel spherical formulation of amorphous Gd:Mn nanoparticles using a simple synthesis procedure.

## **Materials and Methods**

### *Materials*

Gadolinium oxide nanopowder (Gd<sub>2</sub>O<sub>3</sub>, 99.9+%) was purchased from Nanostructured and Amorphous Materials, Inc. Colour: white. Average particle size: 20-80 nm (determined from Specific Surface Area). Specific Surface Area: 10-40 m<sup>2</sup>/g. Purity: 99.9+% (Rare Earth Oxide). Morphology: Nearly spherical.

MnCl<sub>2</sub>·4H<sub>2</sub>O, PFA (paraformaldehyde), RNase A, and crystal violet were purchased from Sigma-Aldrich. HNO<sub>3</sub>, HCl, NaOH, urea, glycerol, methanol, ethyl alcohol and triton X-100 were purchased from Thermo Fisher Scientific. PBS (phosphate buffered saline) was supplied by the Experimental Oncology Laboratory at University of Alberta. Doxorubicin Hydrochloride Injection (2 mg/mL, 200 mg) was purchased from Pfizer Pharmaceutical Inc. Cell culture medium, FBS (fetal bovine serum) and PBS used for cell culture were purchased from Gibco.

Antibiotic-Antimycotic and all molecular dyes were purchased from Life Technologies, unless otherwise specified.

Centrifuge tubes, Petri dishes, cell culture flasks and all other consumable wares and plastics used for cell culture were purchased from Corning Inc., unless otherwise specified.

*Fabrication of Gd(OH)<sub>3</sub>, Gd(OH)<sub>3</sub>:Mn Nanorods and Gd(OH)<sub>3</sub>:Mn-Dox Nanocomplexes and Study of Their Morphology*

Gd(OH)<sub>3</sub> and Gd(OH)<sub>3</sub>:Mn nanorods were synthesized through hydrothermal processes. First, gadolinium oxide nanopowder was dissolved in nitric acid (20 v/v% in ddH<sub>2</sub>O) and diluted to give a 0.125M Gd(NO<sub>3</sub>)<sub>3</sub> solution. A 0.125M Mn<sup>2+</sup>-containing solution was made using MnCl<sub>2</sub>·4H<sub>2</sub>O and ddH<sub>2</sub>O.

For Gd(OH)<sub>3</sub> nanorod synthesis, 10 mL of the Gd(NO<sub>3</sub>)<sub>3</sub> solution was diluted in 35 mL ddH<sub>2</sub>O, followed by the dropwise addition of 2 mL of 1.5M NaOH with continuous stirring.

To produce the Gd(OH)<sub>3</sub>:Mn nanorods, 10 mL of the prepared Gd(NO<sub>3</sub>)<sub>3</sub> solution and 2 mL of the prepared MnCl<sub>2</sub> solution were combined and diluted with 35 mL ddH<sub>2</sub>O followed by the dropwise addition of 2.1 mL of 1.5M NaOH under continuous stirring. The resulting mixture was heated for 2.5 hours in a 90°C water bath with continuous stirring to produce the Gd(OH)<sub>3</sub>:Mn nanorods.

A post-loading mechanism enabled the assembly of Gd(OH)<sub>3</sub>:Mn-Dox nanocomplexes. Synthesis of the Gd(OH)<sub>3</sub>:Mn-Dox nanocomplexes was carried out as follows: Injectable doxorubicin hydrochloride (5 mL, 2 mg/mL) solution was added to the solution prior to the addition of NaOH in the above-described process for the synthesis of Gd(OH)<sub>3</sub>:Mn nanorods.

## *Characterization of the Obtained Nanoparticles by SEM, TEM, ICP-MS and X-Ray Powder Diffraction*

SEM characterization was carried out on a JEOL FXV SEM (JSM-6301) and TEM characterization was performed on a JEOL-2100 TEM at 200 kV. Specimens were washed no less than three times using ddH<sub>2</sub>O and placed on specimen holder for SEM study and specimen grids for TEM study. The length and width of the examined samples were measured from prints of the TEM images in Figure 1 and presented as the mean value and standard deviation in Table 1.

Obtained nanostructures were quantified by means of ICP-MS (inductively coupled plasma-mass spectrometry ; Elan 6000, Perkin Elmer) for metal elements and the Dox content was measured using an Evolution 60 S UV–Vis Spectrophotometer (Thermo Scientific). X-ray powder diffraction (XRD) was used to study the crystalline structures of the synthesized Gd(OH)<sub>3</sub> nanorods, Gd(OH)<sub>3</sub>:Mn nanorods and Gd(OH)<sub>3</sub>:Mn-Dox nanocomplexes. XRD was carried out on an Ultima IV Rigaku x-ray powder diffraction platform at 38 kV and 38 mA with a cobalt tube. Prior to XRD analysis, the samples were dried in a vacuum oven at 60±10°C for 24 hours and crushed into powder (they were crushed roughly using spatula prior to submission for XRD and then further crushed and prepared by the XRD operator).

## *Cell Culture*

Studies in this chapter used human breast cancer cell line MDA-MB-231 (ATCC). The cell line was cultured in DMEM (Dulbecco's Modified Eagle Medium) supplemented with 1% antibiotic-antimycotic and 10% FBS. The humidified cell incubator was maintained at 37°C and

5% CO<sub>2</sub>. A Beckman Coulter cell counter was used for cell counting. All the cells in this chapter were cultured under the same growth conditions, unless otherwise mentioned.

#### *Determination of Cellular Uptake of Gd(OH)<sub>3</sub>:Mn-Dox Nanocomplexes*

Since doxorubicin has a quinone-containing chromophore that causes it to emit red fluorescence under a fluorescence microscope, confocal laser scanning microscopy was used to study cellular uptake of Gd(OH)<sub>3</sub>:Mn-Dox nanocomplexes by MDA-MB-231, a human breast cancer cell line. Cells were seeded on glass microscope coverslips and treated with Gd(OH)<sub>3</sub>:Mn-Dox nanocomplexes for 4 hours, 24 hours, or six days before the cells were washed with phosphate-buffered saline (PBS, pH 7.4) and fixed in paraformaldehyde (PFA, 4%, v/v). A mounting medium fortified with DAPI (4',6-diamidino-2-phenylindole) at a concentration of 1:2000 was used to mount the samples on glass slides for confocal microscopy studies. Confocal immunofluorescence microscopy images were collected on a Carl Zeiss laser scanning confocal microscope (LSM-710) equipped with 1.4 OIL DIC M27 (40X) and Carl Zeiss ZEN software (2011 black, 7.0.4.0).

#### *In Vitro Cytotoxicity and Radiation Sensitizing Effect Assessment*

To study Gd(OH)<sub>3</sub>:Mn-Dox nanocomplex-induced cytotoxicity and radiation enhancement efficiency, 1x10<sup>6</sup> MDA-MB-231 cells were seeded in Corning T-25 flasks for one night before treatment with various concentrations (30, 150, 300, 700 and 1000 µg/mL) of Gd(OH)<sub>3</sub>:Mn-Dox nanocomplexes or sterile PBS (0 µg/mL of the nanocomplexes). The radiation group received 3 Gy of x-ray irradiation after one day of nanocomplex treatment. All the cells were then kept in the incubator for another six days to allow for the doxorubicin and irradiation

to take effect. On the end day of the experiment, the cells were fixed with 70% alcohol, followed by Triton X-100 (0.25% in ddH<sub>2</sub>O) treatment and RNase A-containing propidium iodide (PI) staining for flow cytometry analysis of cell apoptotic rate. The examination was performed using a BD Biosciences FACS Calibur flow cytometer. The statistical analyses were conducted with a Graphpad Prism 5 (Graphpad Software Inc., Ver 5.04). The effects of radiation on the apoptosis and clonogenic studies were evaluated with two-way ANOVA using Bonferroni multiple comparisons with the significance set at  $P < 0.0001$ .

A clonogenic cell survival assay was used to test the radiosensitizing potential of the synthesized Gd(OH)<sub>3</sub>:Mn-Dox nanocomplexes. 400 cells were seeded on each of thirty 100 mm Petri dishes (n=3 for each group). The dishes were randomized into radiation and non-radiation groups. Cells in each group were treated with Gd(OH)<sub>3</sub>:Mn nanorods or Gd(OH)<sub>3</sub>:Mn-Dox nanocomplexes at a concentration of 30 or 75 µg/mL, and sterile PBS-treated dishes were used as controls. A 3 Gy x-ray irradiation was performed one day after the treatment. All dishes were then kept in the incubator for another 15 days before the cells were fixed in methanol and dyed with crystal violet (0.5%) following standard methods<sup>176</sup>. Cell counts were performed using ImageJ (version 1.48d © National Institute of Health<sup>177</sup> image processing software. The plating efficiency (PE %) was calculated as:

$$PE \% = \frac{\text{Clones Counted}}{\text{Plated cells}} \times 100\%$$

The percent survival rate (Survival %) was calculated as:

$$\text{Survival \%} = \frac{\text{PE\% of test group}}{\text{PE\% of control group}} \times 100\%$$

The results and statistical analyses were calculated as previously reported by Munshi A *et al*<sup>176</sup>.

### *In Vivo Observation of Acute Toxicity and Organ Distribution (Pilot Study)*

To develop a preliminary understanding of *in vivo* compatibility and possible accumulation sites of the Gd(OH)<sub>3</sub>:Mn-Dox nanocomplexes, a dose of 8 mg/kg Gd(OH)<sub>3</sub>:Mn-Dox nanocomplexes was administered intravenously to an RNU female rat bearing a xenografted human breast cancer tumor, which had previously been developed by injecting 10 million MCF-7 human breast cancer cells subcutaneously into the flank of the rat<sup>178</sup>. The rat was observed for any abnormal behaviors or acute toxic effects for five hours after the rat was dosed. After 24 hours of treatment, the rat was euthanized, blood was collected, and organs of interest (heart, lungs, liver, spleen, kidneys, tumour, muscle and brain) were collected and weighed. The blood sample was dissolved in set volumes of nitric acid (68%) and the sampled organs were cut into pieces and fully dissolved in set volumes of nitric acid (68%) for gadolinium analysis at room temperature. This took approximately 1 week. Once all the samples in nitric acid were fully dissolved, the gadolinium content analysis was carried out using inductively coupled plasma mass spectroscopy (ICP-MS, Thermo Scientific ICAP-Q quadrupole ICP-MS, in the University of Alberta Department of Earth and Atmospheric Sciences).

### *Synthesis of Gd:Mn Nanospheres*

To demonstrate the feasibility of fabricating spherical Gd:Mn nanoparticles, a hydrothermal homogeneous precipitation method was adapted to produce monodisperse amorphous Gd:Mn nanospheres<sup>166</sup>. Reactants used were the same as those used in the synthesis of the Gd:Mn-Dox nanocomplexes, except that a urea solution was used in place of the NaOH solution to give a milder reaction process, and glycerol was added. The urea solution was

prepared by dissolving urea in ddH<sub>2</sub>O to give a 150 mg/mL urea solution. The glycerol (which was a key factor for size and morphology control) solution (50%, v/v) was made by mixing equal volumes of glycerol and ddH<sub>2</sub>O. Synthesis of Gd:Mn nanospheres was carried out in a vacuum oven reactor at 120°C for 3.5 hours at atmospheric pressure. The reactor used was a steel autoclave tube lined with a 45 mL Teflon tube. Prior to feeding the reactor, 1.125 mL of the Gd(NO<sub>3</sub>)<sub>3</sub> solution described above, 125 µL of the MnCl<sub>2</sub> solution described above, various quantities (0.4 to 5 mL) of glycerol, and 1.5 mL urea were successively added into 20 mL ddH<sub>2</sub>O. The mixture was homogenized vigorously on a magnetic stirrer for 10 to 15 minutes and maintained at 37°C in a water bath before being fed into the reactor. Appropriate quantities of urea and glycerol are critical factors for the development of homogeneous spherical precipitates and for control of their sizes. A number of experiments were attempted at various ratios of urea and glycerol to the other reactants, which were found to produce particles of varying diameters, as well as varying the sequence of adding the various reaction components. Before the near-spherical nanoparticles were successfully produced, a large number of attempts were conducted. Two types of hydrothermal synthesis methods were explored. The method not used in the successful production of spherical particles, referred to below as “BnS”, used a different synthesis apparatus. When using the BnS method, the solution containing the reactants was placed in a conical flask partially submerged in a boiling water bath. The conical flask was tightly sealed to prevent the evaporation of water and the reaction was carried out with continuous stirring in the dark to produce Dox-loaded products (as Dox molecules are sensitive to light). Since the chemical composition of the successfully synthesized gadolinium and manganese containing nanoparticles is not well understood, they are referred to as Gd:Mn nanospheres. Final products were washed with ddH<sub>2</sub>O and ethanol and then resuspended in

ddH<sub>2</sub>O. Samples of each batch were characterized via transmission electron microscope. TEM characterization was performed on a JEOL-2100 TEM at 200 kV. Specimens were washed no less than three times using ddH<sub>2</sub>O and placed on specimen grids for TEM study.

## Results & Discussion

### *Fabrication of Gd(OH)<sub>3</sub>, Gd(OH)<sub>3</sub>:Mn Nanorods and Gd(OH)<sub>3</sub>:Mn-Dox Nanocomplexes and Study of Their Morphology*

The method for synthesis of Gd(OH)<sub>3</sub>:Mn-Dox described resulted in a monodisperse Gd(OH)<sub>3</sub>:Mn-Dox nanocomplex suspension. Synthesized Gd(OH)<sub>3</sub>:Mn nanorods assemble into monodispersed nanocomplexes in the presence of doxorubicin in a basic environment. Doxorubicin molecules work as binders among the synthesized individual Gd(OH)<sub>3</sub>:Mn nanorods. They also function as therapeutic payloads. Figure 2-1 shows the SEM images of the prepared nanorods and nanocomplexes. Figure 2-1 panels (a) and (b) show rod/needle-like Gd(OH)<sub>3</sub> and Gd(OH)<sub>3</sub>:Mn nanoparticles, respectively, while (c) shows the Gd(OH)<sub>3</sub>:Mn-Dox nanocomplexes. As seen in Table 2-1, doping with manganese ions resulted in increased length and smoother surfaces of the synthesized nanorods compared with the Gd(OH)<sub>3</sub> nanorods, while the addition of doxorubicin produced bundles of nanorods with decreased length compared to the Gd(OH)<sub>3</sub>:Mn nanorods. Figure 2-2 illustrates the hypothesized principle behind the formation of Gd(OH)<sub>3</sub>:Mn-Dox nanocomplexes. Doxorubicin, as an anthracycline, is known to have a high affinity for gadolinium (a lanthanide metal) ions, which associate with its 11,12-(β)-ketophenolate group on the anthraquinone skeleton<sup>174,179</sup>. So, through this functional site, it is believed that doxorubicin molecules chelate with gadolinium ions on the surface of the nanorods

as they form. The ( $\pi$ )-electrons containing aromatic rings of doxorubicin molecules then associate to hold the nanorods together as bundles.

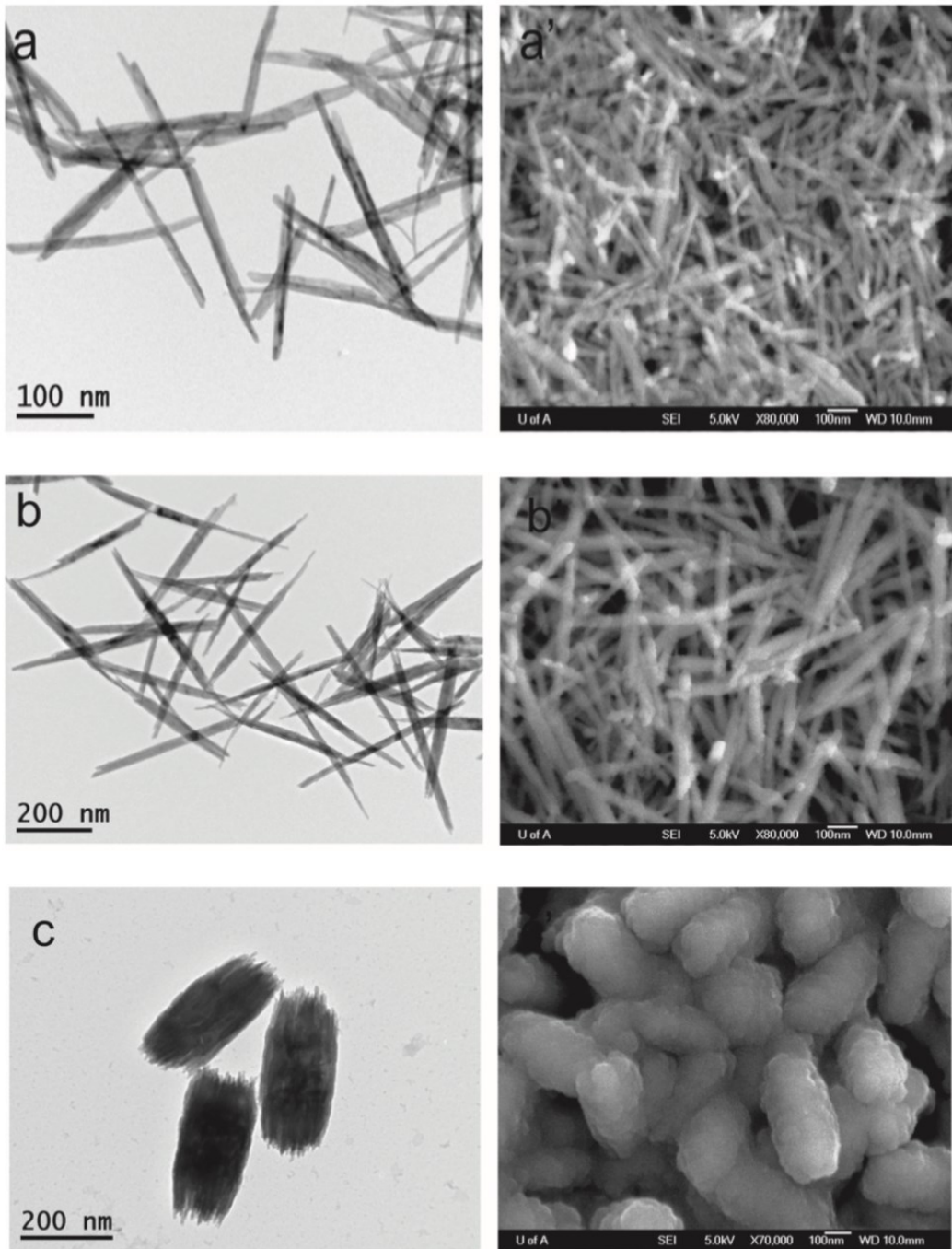


**Figure 2-1.** Transmission electron microscopy (left column) and scanning electron microscopy (right column) images of Gd(OH)<sub>3</sub> (a) and Gd(OH)<sub>3</sub>:Mn (b) nanorods, as well as Gd(OH)<sub>3</sub>:Mn-Dox nanocomplexes (c).

**Table 2-1.** Sizes of Gd(OH)<sub>3</sub> nanorods, Gd(OH)<sub>3</sub>:Mn nanorods and Gd(OH)<sub>3</sub>:Mn-Dox nanocomplexes in Figure 1.

Nanoparticles	Length <sub>(nm)</sub>	Width <sub>(nm)</sub>	Sample number
Gd(OH) <sub>3</sub> nanorods	247±15	13±5	5
Gd(OH) <sub>3</sub> :Mn nanorods	422±50	19±0	6
Gd(OH) <sub>3</sub> :Mn-Dox nanocomplexes	348±17	158±8	3

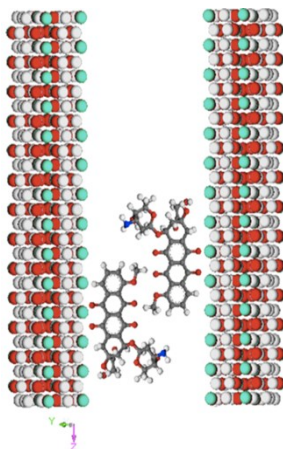


**Figure 2-2.** Proposed mechanism for the interaction between doxorubicin molecules and Gd(OH)<sub>3</sub>:Mn nanorods. Doxorubicin molecules work as binding agents to holding the assembled nanorods together in bundles. Cyan=gadolinium, grey=carbon, white=hydrogen, red=oxygen, blue=nitrogen (Mn not shown).

#### *Characterization of the Obtained Nanoparticles by X-Ray Powder Diffraction*

The results of the XRD analysis of the Gd(OH)<sub>3</sub>, Gd(OH)<sub>3</sub>:Mn and Gd(OH)<sub>3</sub>:Mn-Dox are shown in Figure 2-3. The sharp diffraction peaks present indicate that the tested samples are

crystalline materials. The  $\text{Gd}(\text{OH})_3$  nanorods have the same diffraction pattern as the gadolinium hydroxide powder's standard reference diffraction file in JCPDS (No. 83-2037:  $\text{Gd}(\text{OH})_3$ ). There were no additional diffraction peaks in the  $\text{Gd}(\text{OH})_3:\text{Mn}$  or  $\text{Gd}(\text{OH})_3:\text{Mn-Dox}$  samples, which indicated that the added manganese and doxorubicin were not incorporated into the crystal structure of the gadolinium hydroxide, but rather occurred in an amorphous phase. The metal and drug compositions of the synthesized nanostructures are presented in Table 2-2 along with the lattice constants of them as determined via Rietveld analysis. The absence of the impurity peaks and diffuse peaks indicates that no other phases resulted with the addition of Mn and Dox. This further indicates that Mn and/or Dox can be isomorphously introduced into the crystal structure of  $\text{Gd}(\text{OH})_3$  or associate in a manner that does not change the crystal structure of  $\text{Gd}(\text{OH})_3$  nanorods.

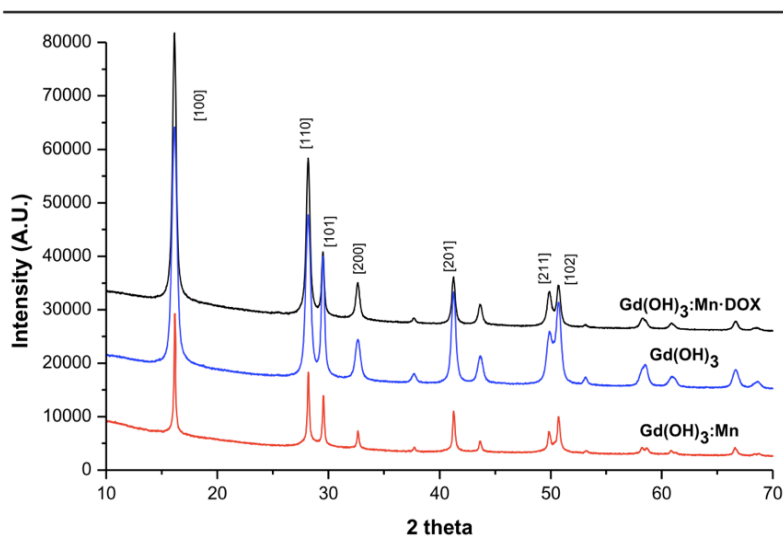


**Figure 2-3.** X-ray powder diffraction patterns of  $\text{Gd}(\text{OH})_3$  nanorods,  $\text{Gd}(\text{OH})_3:\text{Mn}$  nanorods, and  $\text{Gd}(\text{OH})_3:\text{Mn-Dox}$  nanocomplexes.

	Gd(OH) <sub>3</sub>	Gd(OH) <sub>3</sub> :Mn	Gd(OH) <sub>3</sub> :Mn-Dox
<b>Mass fractions (<math>\omega_i</math>)</b>			
<b>Gd</b>	1	0.997 86	0.892 183
<b>Mn</b>	0	0.002 14	0.029 363
<b>Dox</b>	0	0	0.078 454
<b>Space group</b>	<i>P6<sub>3</sub>/m</i>	<i>P6<sub>3</sub>/m</i>	<i>P6<sub>3</sub>/m</i>
<b>Lattice parameters (Å)</b>			
	a = 6.344 65	a = 6.337 37	a = 6.335 68
	b = 6.344 65	b = 6.337 37	b = 6.335 68
	c = 3.636 62	c = 3.633 41	c = 3.627 27
<b>Crystallite Size (nm)</b>			
	A = 540.849 35	A = 250.412 46	A = 460.767 52
	B = 540.849 35	B = 250.412 46	B = 460.767 52
	C = 1106.115 70	C = 1055.078 26	C = 622.704 69
<b>Lattice strain</b>			
	A = 0.297 40	A = 0.013 77	A = 0.013 77
	B = 0.297 40	B = 0.013 77	B = 0.013 77
	C = 0.104 66	C = 0.625 67	C = 0.231 81
<b>Rwp (%)</b>	1.73	2.68	4.31

**Table 2-2.** Components and refinement parameters of the synthesized crystal nanostructures.

#### *Determination of Cellular Uptake of Gd(OH)<sub>3</sub>:Mn-Dox Nanocomplexes*

Figure 2-4 represents the fluorescence images captured via confocal microscopy during the study of cellular uptake of Gd(OH)<sub>3</sub>:Mn-Dox in a human breast cancer cell line. The red fluorescence is emitted by doxorubicin molecules, and the blue is emitted by DAPI, the DNA counterstain reagent that bonded with DNA inside cell nuclei. With 4 hours of incubation, it was possible to observe that Gd(OH)<sub>3</sub>:Mn-Dox nanocomplexes (red fluorescence) accumulated in the cell plasma. After 24 hours of incubation, more Gd(OH)<sub>3</sub>:Mn-Dox nanocomplexes, producing a stronger red fluorescence, accumulated in cell plasma. After six days of incubation, the doxorubicin, which was originally loaded in the Gd(OH)<sub>3</sub>:Mn-Dox nanocomplexes, bound with DNA in the cell nuclei after evidently being released from the nanocomplexes. Since the nanocomplexes were not able to penetrate the membrane of the cell nucleus due to their size, the

doxorubicin signals in the cell nuclei must be from doxorubicin molecules released from the nanocomplexes.

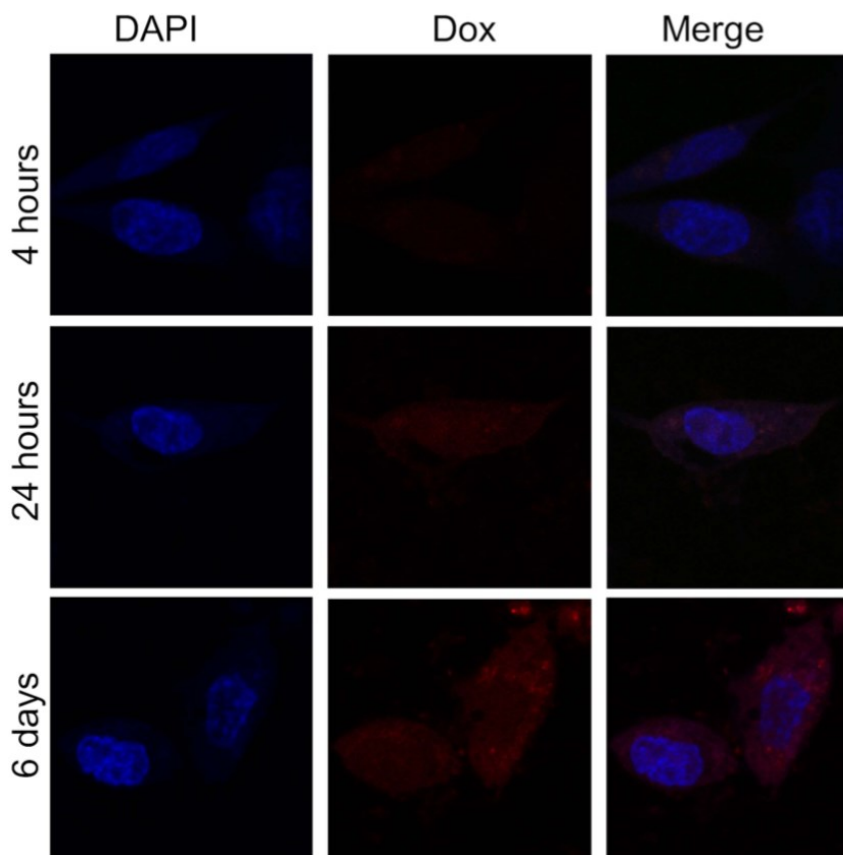


**Figure 2-4.** Confocal images of cellular uptake of Gd(OH)<sub>3</sub>:Mn-Dox nanocomplexes after 4 hours, 24 hours, and six days of incubation with MDA-MB-231 cells. Blue indicates cell nuclei and red indicates doxorubicin loaded within, and released from, the nanocomplexes.

#### *In Vitro Cytotoxicity and Radiation Sensitizing Effect Assessment*

The *in vitro* anti-human breast cancer cell efficacy of the Gd(OH)<sub>3</sub>:Mn-Dox nanocomplexes with applied external x-ray irradiation can be seen in Figure 2-5. The percentage of apoptotic cells induced by the nanocomplexes increased in a dose-dependent manner. In the 300 and 700 µg/mL treated groups, the combination treatment of Gd(OH)<sub>3</sub>:Mn-Dox

nanocomplexes and x-ray irradiation significantly increased the number of apoptotic cells compared with the non-radiation group by 26.6% and 32.7%, respectively.

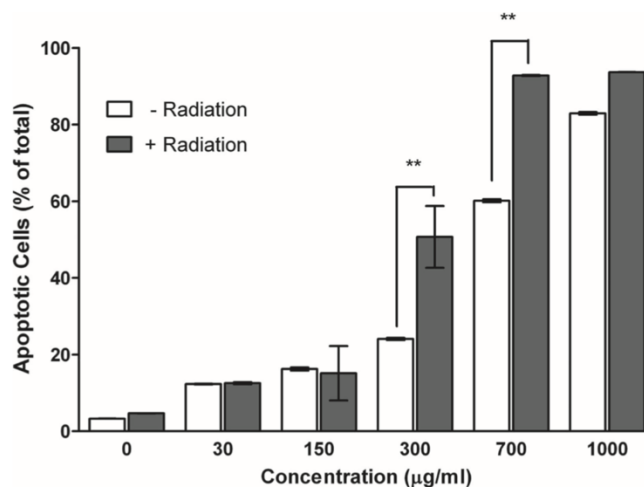


**Figure 2-5.** MDA-MB-231 cell apoptotic rates after various treatments. The x-axis shows an increasing dose of Gd(OH)<sub>3</sub>:Mn-Dox nanocomplexes applied to experimental groups with or without radiation. Solid colour filled columns represent irradiated groups, while the white columns represent non-irradiated groups. \*\*  $p < 0.0001$ .

In this clonogenic assay, the controls were the saline-treated groups, which, for the purpose of calculations, were assumed to have a 100% survival rate (Figure 2-6). Based on that assumption, the 75 µg/mL Gd(OH)<sub>3</sub>:Mn-Dox treated groups were non-proliferative, with or without the application of the external radiation. This can be attributed to the doxorubicin's cytotoxic effect, as compared to the Gd(OH)<sub>3</sub>:Mn treated group. The lower dose (30 µg/mL) Gd(OH)<sub>3</sub>:Mn-Dox treated group appeared to have a higher survival rate than the 75 µg/mL Gd(OH)<sub>3</sub>:Mn-Dox treated group. The radiation-sensitizing effect of the synthesized gadolinium based nanoparticles was observed in this experiment. In the Gd(OH)<sub>3</sub>:Mn treated groups, as shown in Table 2-3, the inhibition of the cancer cells' reproductive ability was appreciably

enhanced, by 52.1% and 54.7%, at concentrations of 30 and 75  $\mu\text{g}/\text{mL}$ , respectively, compared to the radiation-only and  $\text{Gd}(\text{OH})_3\text{:Mn}$ -only groups' outcomes.

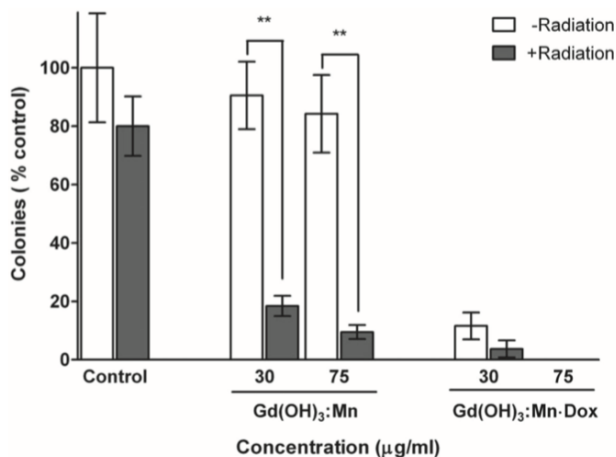


**Figure 2-6.** Clonogenicity assay results comparing irradiated and non-irradiated groups treated with  $\text{Gd}(\text{OH})_3\text{:Mn}$  nanorods or  $\text{Gd}(\text{OH})_3\text{:Mn-Dox}$  nanocomplexes.  $**p < 0.0001$ .

**Table 2-3.** Clonogenicity assay results of irradiated and non-irradiated groups treated with  $\text{Gd}(\text{OH})_3\text{:Mn}$  nanorods or  $\text{Gd}(\text{OH})_3\text{:Mn-Dox}$  nanocomplexes.

		PBS	$\text{Gd}(\text{OH})_3\text{:Mn}$		$\text{Gd}(\text{OH})_3\text{:Mn-Dox}$	
			30 $\mu\text{g}/\text{mL}$	75 $\mu\text{g}/\text{mL}$	30 $\mu\text{g}/\text{mL}$	75 $\mu\text{g}/\text{mL}$
	<i>PE %</i>	15.8	14.3	13.3	1.83	0
<b>- Radiation</b>	<i>Survival</i>	100	90.5	84.2	11.5	0
	<i>%</i>					
<b>+ Radiation</b>	<i>PE %</i>	12.6	2.9	1.5	0.58	0

<i>Survival</i>	80	18.4	9.5	3.7	0
%					

*In Vivo Observation of Acute Toxicity and Organ Distribution (Pilot Study)*

Prior to rat euthanization, no acute toxicity, apparent distress, or obvious signs of poor health were observed. The harvested organ weights were 1.9, 3.7, 0.7, 2.6, 8.6, 1.3, 1.7, 2.6, and 0.5 g for kidneys, blood, heart, tumor, liver, lung, brain, muscle and spleen, respectively. Figure 2-7 represents the gadolinium content in these organs 24 hours after injection. Approximately half of the injected dose was retained in the rat body after 24 hours, with the most significant accumulation being in the spleen, as previously observed in the biodistribution profile of Gd(OH)<sub>3</sub> nanorods in mice<sup>168</sup>. Gadolinium content detected in the tumor suggested successful tumor penetration and retention of the Gd(OH)<sub>3</sub>:Mn-Dox nanocomplexes with no observable adverse effects at the tested dose.

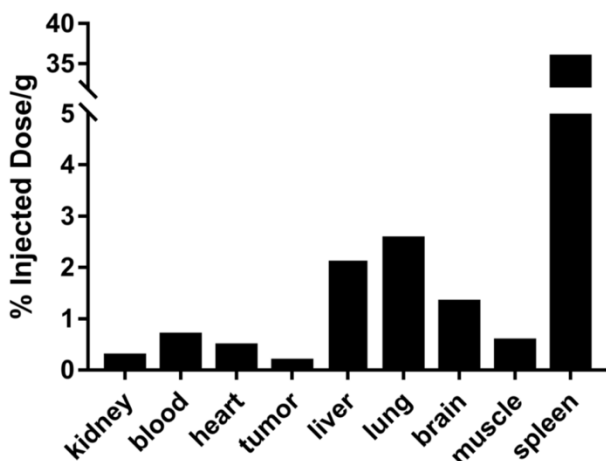


**Figure 2-7.** Gadolinium content in different organs of interest in a female RNU rat with human breast cancer tumor xenograft 24 hours after injection of  $Gd(OH)_3:Mn-Dox$ . The gadolinium uptake in different organs was assessed using ICP-MS. The data are presented as the percentage of the total injected dose per gram of tissue.

### *Synthesis of Gd:Mn Nanospheres*

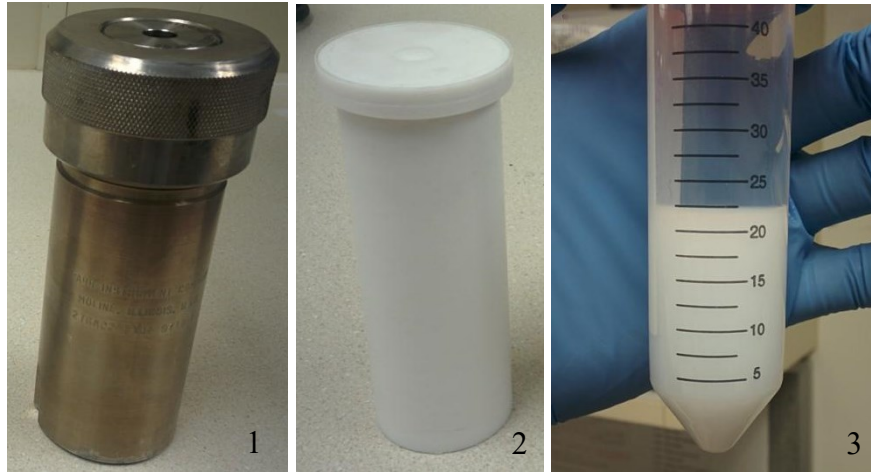
The hydrothermal homogeneous precipitation method was finally adopted. Using the BnS method, it was challenging to make sure every step of setting up the apparatus was done optimally, while needing to add hot water to the boiling water bath frequently without lowering the water bath temperature too much. Although the BnS method required more effort than the method described as the successful method in this section, it was still possible to harvest spherical particles from the BnS method. Besides the selection of an appropriate synthesis method, the reactants' composition ratio and the mixing sequence of each reactant were key to a successful synthesis of spherical amorphous gadolinium nanocomplexes. Following the sequence of adding reactants described here led to an evenly distributed and monodisperse final products. When introducing Dox into the system, a different sequence of adding reactants had to be

developed, as described in Chapter 3. The reactants' composition ratio affects the morphology and yield of the final products. The optimal formula is described in Chapter 3. When the quantity of Gd is set, the quantity of glycerol mainly affects the product's size and morphology (see Figure 2-8), while the quantity of urea mainly affects the yield and morphology. A higher relative quantity of glycerol produces smaller sized particles, and conversely, lowering the glycerol ratio increases the product's diameter. Urea also helps the precipitation process. When quantity of urea is too low, a lower yield is obtained. However, 2-3 times or more than the optimal quantity of urea results in the production of crystalline rod clusters or irregular precipitations (see Figure 2-8b-6).

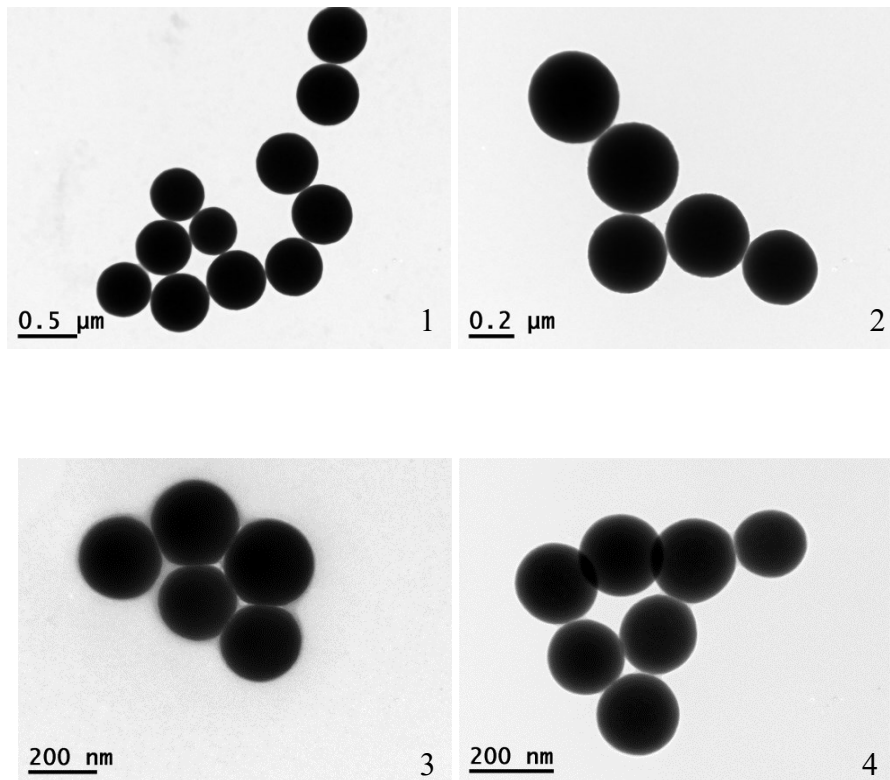
Figure 2-8 shows the equipment used, and the final product when using the above described method to create Gd:Mn nanospheres, including the autoclave tube (2-8a-1) and Teflon tube (2-8a-2) used to line the autoclave tube; the final Gd:Mn nanosphere product suspended in ddH<sub>2</sub>O (2-8a-3); and transmission electron microscope images (2-8b) of synthesized Gd:Mn nanospheres of different sizes. Monodisperse spherical particles of different diameters were observed with TEM, which demonstrated that this fabrication method produced nanoparticles with a smooth surface and perfect spherical shape. Particle shape and size are the two most important parameters that affect the dynamic stability of nanoparticles when injected into a bloodstream, and their interaction with cells at a subcellular level<sup>180,181</sup>. A spherical shape is better than other morphologies in terms of the flow dynamics of nanoparticles. This method resulted in nanospheres with as desirable a morphology as those synthesized previously using other methods but using a simpler and more environmentally friendly procedure. It was determined that the size of the Gd:Mn nanospheres could be controlled by varying the glycerol ratio in the reaction solution (as shown in Figure 2-8c). The introduced urea and glycerol

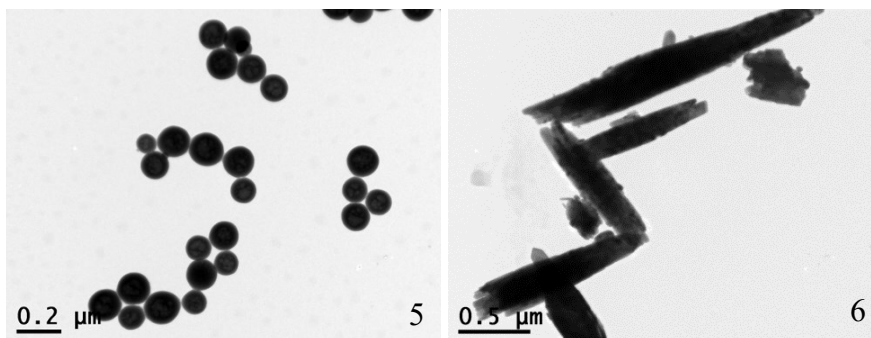
contribute to control the formation of the spherical morphology, preventing the production of the rod-like particles described earlier. Excess quantities of urea or NaOH make the final products into rod/rice-like particles (as shown in the last image of Figure 2-8b).

a:



b:





c:

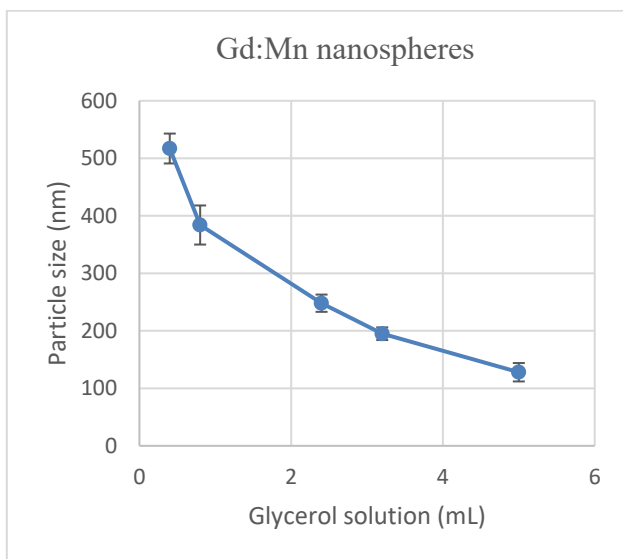


**Figure 2-8.** a: The reactor used for synthesizing Gd:Mn nanospheres consisted of an autoclave tube (a-1) lined with a Teflon tube (a-2), a-3 shows the synthesized Gd:Mn nanospheres suspended in ddH<sub>2</sub>O. b: TEM images of Gd:Mn nanospheres produced at different diameters (from b-1 to b-5, these were produced with 0.4, 0.8, 2.4, 3.2, and 5 mL of glycerol solution, respectively); note that the last image (b-6) shows rod/rice-like particles produced with excess quantities of urea solution (7.5 mL). c: The relationship between the quantity of glycerol solution used and particle sizes of corresponding synthesized Gd:Mn nanospheres is shown.

## Conclusions

In conclusion,  $\text{Gd}(\text{OH})_3$  nanorods,  $\text{Gd}(\text{OH})_3:\text{Mn}$  nanorods and  $\text{Gd}(\text{OH})_3:\text{Mn-Dox}$  nanocomplexes were successfully synthesized using a single-step wet chemical method. Characterization of size and morphology of these three nanostructures, and proof of concept testing, demonstrating promising synergistic anticancer effects of loaded Dox and enhanced radiation efficiency of the nanostructures, were conducted. The potential of the use of  $\text{Gd}(\text{OH})_3:\text{Mn-Dox}$  nanocomplexes as a multifunctional nanoplatform was explored. Confocal microscopy was used to confirm and visualise the cellular uptake and payload release of  $\text{Gd}(\text{OH})_3:\text{Mn-Dox}$  nanocomplexes against a human breast cancer cell line. The therapeutic efficacy of  $\text{Gd}(\text{OH})_3:\text{Mn-Dox}$  nanocomplexes was assessed by flow cytometry and using a clonogenic assay in the absence and presence of x-ray irradiation. The Dox-mediated formation mechanism of  $\text{Gd}(\text{OH})_3:\text{Mn-Dox}$  nanocomplexes was discussed.  $\text{Gd}(\text{OH})_3:\text{Mn-Dox}$  nanocomplexes could be an efficient multipurpose nanoplatform for synergistic therapy delivery with the added advantage of great ease of fabrication.

Subsequently, amorphous  $\text{Gd}:\text{Mn}$  nanospheres were developed, using a simple hydrothermal homogeneous precipitation method, and were characterized via TEM. Near-spherical shaped and monodisperse particles were produced and observed with varying sizes as the quantity of glycerol was changed. These spherical-shaped particles may have some distinct advantages over the nanorods in terms of their flow dynamics and interactions with cells *in vivo*.

## Chapter 3 – Modifying Morphology and Loading Gd:Mn Nanospheres

### Introduction

As was described in Chapter 2, the gadolinium element, as one of the lanthanide metallic elements, has significant promising and favorable physicochemical features. These unique features can be exploited to make gadolinium ideal for use as a bio-imaging agent and for delivering therapy, thereby potentially benefitting clinical oncology health providers and cancer patients<sup>78,182–185</sup>. Thus, this chapter further explores multifunctional gadolinium-based nanoplatforms.

Doxorubicin is a chemotherapeutic anti-cancer drug that was initially found to be made by a non-wild subspecies of *Streptomyces peucetius* (*Streptomyces peucetius* varietas *caesius*)<sup>186,187</sup>. Clinically, doxorubicin has been commonly administered intravenously, alone or with other approved antineoplastic agents, to treat human cancers including breast carcinoma, acute lymphoblastic and myeloblastic leukemias, soft tissue sarcomas, bronchogenic carcinoma, gynecologic carcinomas, testicular carcinoma, squamous cell carcinoma of the head and neck, and gastric carcinoma<sup>132</sup>. The outstanding antineoplastic activity of doxorubicin is currently attributed to its interaction with DNA of target cells. There are two well-recognized mechanisms of its antineoplastic action: doxorubicin molecules intercalating in double stranded DNA minor grooves, and generation of reactive radicals causing damage to ribose, DNA strands, and cell membranes<sup>135,188,189</sup>.

Doxorubicin and adriamycin, one of the anthracycline antibiotics, naturally form drug-metal complexes with paramagnetic lanthanide elements in aqueous solutions<sup>174,190</sup>. Although the drug-metal interaction between gadolinium ions and doxorubicin molecules, to the knowledge of the author, has not been previously studied, the binding sites and mechanism are anticipated to

be the same as those deduced in the literature for other paramagnetic lanthanide ions interacting with doxorubicin molecules<sup>174,190,191</sup>. It was hypothesized that this mechanism could be exploited to synthesize coprecipitated amorphous Gd:Mn-Dox nanospheres. Manganese, a transition metal which enhances MRI signals, seems to play an important role in the interaction between doxorubicin and DNA<sup>191–193</sup>. Thus, the introduction of manganese into the design was hypothesized to provide additional benefits to the Gd:Mn-Dox nanopatform design.

A modified Poly (L-glutamic acid) (mPGA) has also been introduced as a radiation sensitive polymer coating on the surface of the Gd:Mn-Dox nanospheres, which may convey several advantages, including: prolonged half-life and improved drug biodistribution; radiation activable; and decreased premature release. Poly(L-glutamic acid) is a well investigated polymer that possesses valuable properties including biocompatibility, biodegradability, and water solubility<sup>194–196</sup>. Poly(L-glutamic acid) has already been approved for use as a drug carrier to form water-soluble poly(L-glutamic acid)-paclitaxel drug conjugates, known as Opaxio®. The radiation-sensitive mPGA polymer was synthesized by partially modifying the carboxylic acid side chain with lipophilic chemical groups (e.g. phenacyl ester) through an ester linkage<sup>197,198</sup>.

Here in this chapter, the synthesis of amorphous spherical Mn-doped Gd:Mn nanospheres is proposed, together with the development of Dox-loaded (Gd:Mn-Dox) and surface modified (mPGA@Gd:Mn-Dox) forms of these nanospheres. A hydrothermal homogeneous coprecipitation method was adapted to produce amorphous and size controlled spherical nanoparticles.

Spherical nanoparticles, compared with their rod (needle) shaped counterparts, are reported to have better flow dynamics and to be less likely to marginate and adhere to blood vessel walls prior to reaching the target site<sup>199,200</sup>.

Amorphous solids are non-crystalline substances and are in a thermodynamically high energy state. The conversion of a substance from its crystalline form to an amorphous state is commonly used in the pharmaceutical industry to achieve improvements in dissolution and bioavailability<sup>201,202</sup>. As reported<sup>83</sup>, the mechanism for the release of Gd and Dox from the Gd(OH)<sub>3</sub>:Mn-Dox nanocomplexes developed in Chapter 2 is most effective when dissolution occurs in a low pH environment. Unlike the crystalline Gd(OH)<sub>3</sub>:Mn-Dox nanocomplexes, the herein proposed spherical Gd:Mn and Gd:Mn-Dox nanoparticles are amorphous solids, which may have a shorter payload release time relative to their crystalline counterparts.

The simple and integrative method described in this chapter resulted in the production of doxorubicin-loaded manganese-doped gadolinium nanospheres possessing a higher drug loading capacity than the nanorod complexes fabricated with same components in Chapter 2. The main advantages of the method described in this Chapter are good scale-up potential and ease of manufacture without the introduction of harmful ingredients or procedures<sup>149,203</sup>.

## **Materials and Methods**

### *Materials*

Dimethyl sulfoxide (DMSO) was purchased from Fisher Scientific. The other materials used in this chapter were sourced as described in Chapter 2.

### *Loading Gd:Mn Nanospheres with Doxorubicin*

The same hydrothermal homogeneous coprecipitation method used to synthesize Gd:Mn nanospheres, as described in Chapter 2, was used for the one-pot, one-step synthesis of doxorubicin-loaded Gd:Mn-Dox nanospheres. As the chemical composition of this nano-sized

precipitation containing gadolinium, manganese and doxorubicin was not known, the synthesized doxorubicin-loaded nanoparticles are referred to as Gd:Mn-Dox nanospheres. The synthesis method is described as follows.

1.125 mL Gd(NO<sub>3</sub>)<sub>3</sub> solution (0.125 M), 125 μL MnCl<sub>2</sub> solution (0.125 M), 1.5 mL urea (150 mg/mL solution in water), 1.6 mL doxorubicin hydrochloride injectable solution (2 mg/mL) and 0.4 mL glycerol (50% v/v solution in ddH<sub>2</sub>O) were successively added into 20 mL ddH<sub>2</sub>O. The mixture was homogenized vigorously on a magnetic stirrer for 10 to 15 minutes and maintained at 37°C in a water bath before being fed into the reactor. The procedures that involved doxorubicin were carried out in the dark. The Gd:Mn-Dox nanosphere synthesis was carried out in a vacuum oven at 120°C for 3.5 hours at atmospheric pressure. The final product was washed three times with ddH<sub>2</sub>O and ethanol, and then resuspended in 30 mL ddH<sub>2</sub>O. The supernatant of the final mixture solution was subject to High Performance Liquid Chromatography (HPLC - Shimadzu) equipped with a Diode Array Detection (DAD)/Ultraviolet (UV) detector (Shimadzu). This was used to check for doxorubicin in the post-reaction solution's supernatant. Samples were eluted with a mixture of methanol, phosphoric acid, water, and acetonitrile (at ratios of 170:2:540:290). Flow rate was 1 mL/min. Samples of each batch were characterized using scanning electron microscopy (SEM) and transmission electron microscopy (TEM). SEM characterization was carried out on a Zeiss Sigma 300 VP-FESEM and TEM characterization was performed on a JEOL-2100 TEM at 200 kV. Specimens were washed no less than three times using ddH<sub>2</sub>O and placed on a specimen holder for SEM study or specimen grids for TEM study. Independent two sample t tests were performed for statistical analysis conducted in Microsoft Excel (© 2019 Microsoft Co.)

### Preparation of Partially Modified Poly- $\alpha$ , L-Glutamic Acid (mPGA)

Carboxyl groups on the side chains of poly-L-glutamic acid (PGA) molecule were partially modified with various lipophilic chemical groups (Figure 3-1), which resulted in the production of a series of (more than one hundred) mPGA samples modified with different chemical groups at different grafting degrees. PGA and mPGA samples may undergo auto-hydrolysis. To select candidates with good aqueous solubility and chemical stability, the hydrolytic rate of all the samples was investigated. The hydrolysis rate was studied using a 0.5 M  $\text{NaH}_2\text{PO}_4/\text{Na}_2\text{HPO}_4$  buffer solution (pH 7.0) at room temperature ( $22^\circ\text{C}$ ) using qualitative TLC (thin layer chromatography) analysis. Those samples that underwent the least auto-hydrolysis were selected for the subsequent studies. The modification, and initial screening of mPGA candidates were completed by Dr. Justin Jiang at Lakehead University. Of these samples, a subset of the final mPGA candidates (NO. 128A and NO. 132) were selected and provided for this work, where they were used for *in vitro* and *in vivo* tests, as well as subsequent fabrication of mPGA coated nanoparticles.

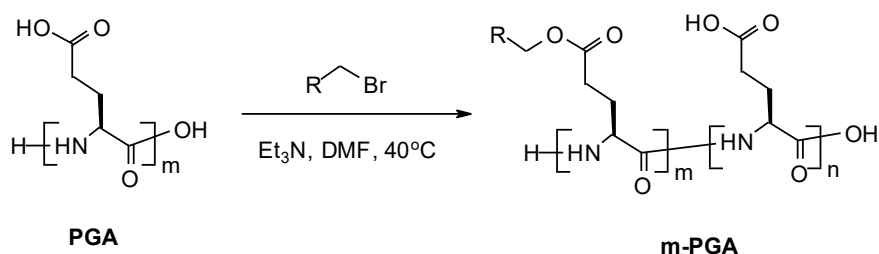


**Figure 3-1.** Reaction scheme for hydrophobic modification of the poly (L-glutamic acid).  $\text{RCH}_2$  = investigated lipophilic substitutes.

### *Fabrication of mPGA@Gd:Mn and mPGA@Gd:Mn-Dox*

The harvested Gd:Mn (see Chapter 2) or Gd:Mn-Dox nanospheres were resuspended in pure DMSO and mixed with modified poly-L-glutamic acid (mPGA NO. 128A or NO. 132) solutions (10:1). Then the mixture was stirred vigorously on a magnetic stirrer at room temperature for 3 hours protected from light, to allow the coating process to occur. The mPGA coated Gd:Mn or Gd:Mn-Dox nanospheres (referred to as mPGA@Gd:Mn or mPGA@Gd:Mn-Dox nanospheres) were washed with ddH<sub>2</sub>O no less than three times and resuspended in 30 mL ddH<sub>2</sub>O. Particles size of nanospheres before and after the coating procedure were measured from the TEM images using FIJI-ImageJ (MacOS version)<sup>177</sup>. TEM characterization was performed on a JEOL-2100 TEM at 200 kV. Specimens were washed no less than three times using ddH<sub>2</sub>O and placed on specimen grids for TEM study.

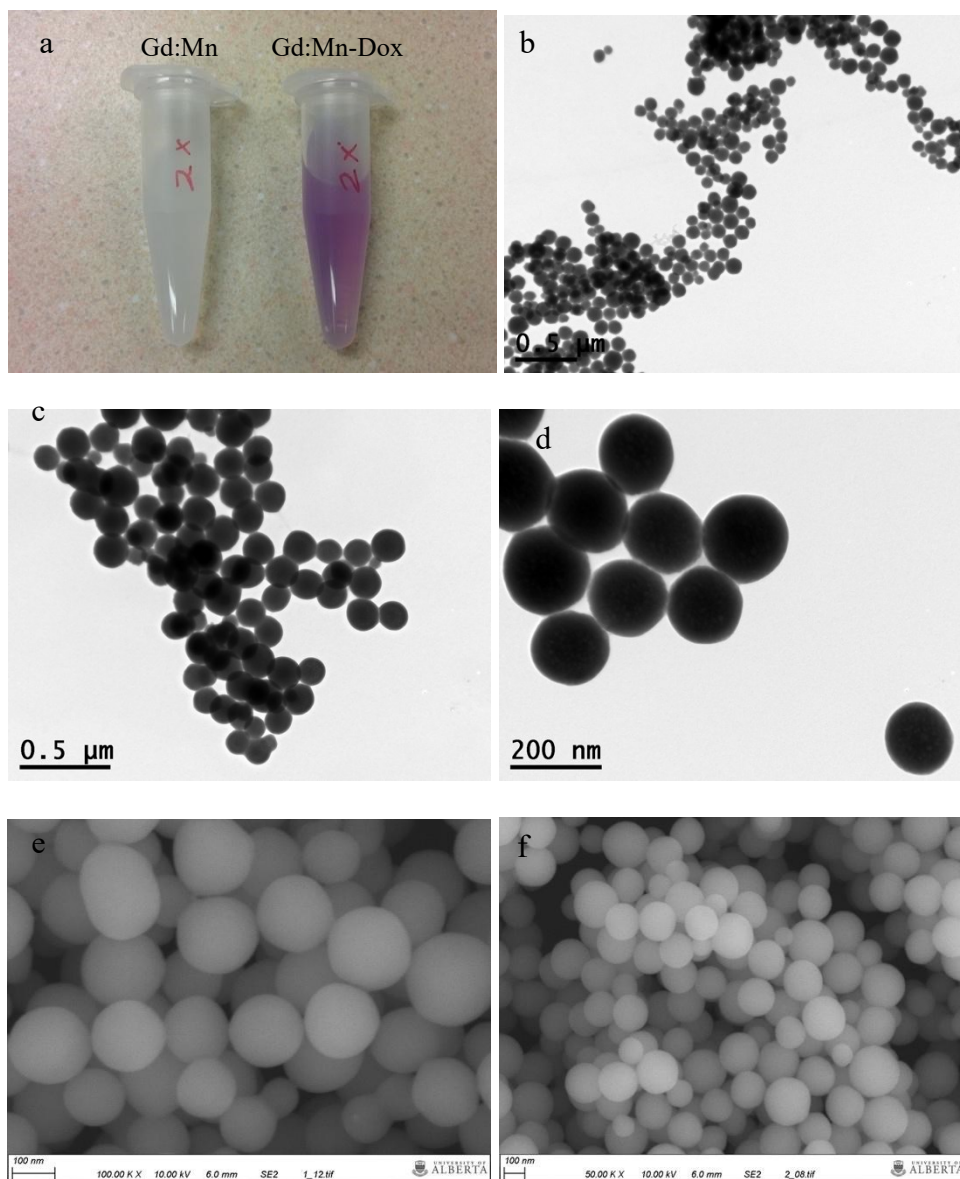
## **Results & Discussion**

### *Loading Gd:Mn Nanospheres with Doxorubicin*

To the knowledge of the author, this is the first time that the doxorubicin organic drug molecule was used to chelate with gadolinium ions instead of using polymer molecules. It is a simple, cost-effective, and environmentally friendly way to produce gadolinium nanoparticles. The final product, which consisted of purple-coloured doxorubicin-loaded Gd:Mn nanoparticles (Figure 3-2a), was obtained with a relatively uniform size (around 150 nm). Figure 3-2 shows TEM and SEM images of the Gd:Mn-Dox nanospheres, which demonstrated sizes ranging from around 80 nm to 200 nm (Figure 3-2b-d). There was no doxorubicin detected in the post-reaction solution's supernatant as measured by a validated method using HPLC. This indicated that all the

doxorubicin was incorporated into the synthesized nanoparticles. Drug loading capacity was calculated by weight percent (wt%) to be 10.1%.

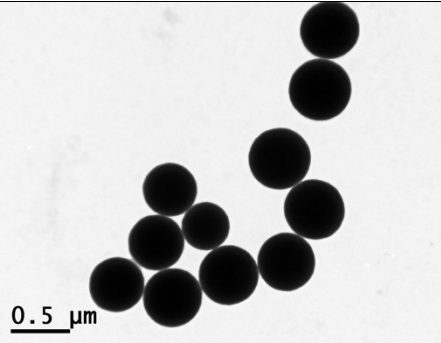
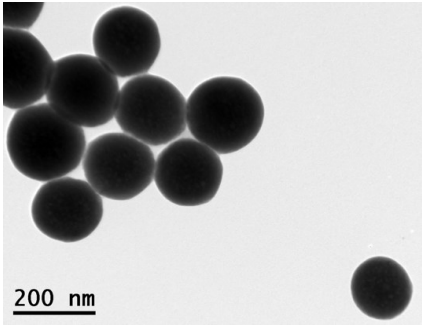
The formulation described here was optimized and used to produce nanoparticles for all the following *in vitro* assays and *in vivo* experiments, unless otherwise indicated. It was determined that a  $\text{GdCl}_3$  solution could be used in place of the  $\text{Gd}(\text{NO}_3)_3$  solution in the reaction process. Theoretically, other safe solutions that can act as a source for Gd ions could be used in the same manner. The morphology and size (the most crucial characteristics) of the nanoparticles are very sensitive to all the initial reaction parameters. The ratio of urea and glycerol are critical factors in the development of homogeneous spherical precipitates and in controlling their size. The adding of doxorubicin into the reaction mixture also decreased the size of the final product (see Table 3-1), similar to what was observed in the  $\text{Gd}(\text{OH})_3\text{:Mn-Dox}$  nanorods synthesis described in Chapter 2. The appearance of the final product changed from white to purple with the addition of the doxorubicin.



**Figure 3-2.** a: Synthesized white Gd:Mn nanospheres and purple doxorubicin-loaded (Gd:Mn-Dox) nanospheres suspended in ddH<sub>2</sub>O; b, c, d: TEM images of Gd:Mn-Dox nanospheres of various sizes, which were achieved by varying the ratio of glycerol:urea – in the figure, the ratios used were 0.8:1.5, 0.4:2, and 0.4:1.5, respectively); e, f: SEM images of Gd:Mn-Dox nanospheres.

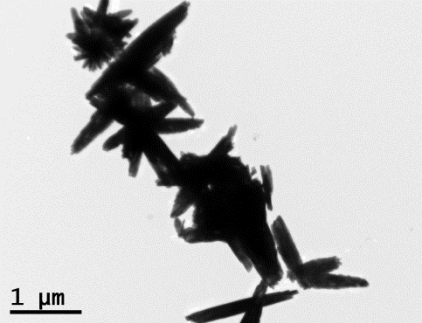
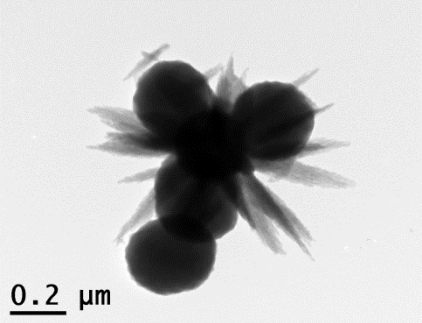
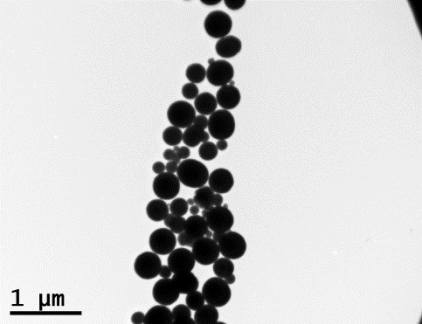
**Table 3-1. a:** The synthesized nanospheres showed a decreased diameter after doxorubicin was added to the reaction system; b: different ratios of glycerol:urea affected the morphology and diameter of the final products.

a:

	TEM image of synthesized nanospheres	Mean size of nanospheres in the TEM image (nm) **	Number of Samples (n)
No doxorubicin added		517 ± 26	11
Doxorubicin added		176 ± 12	10

\*\* The mean sizes of these two batches of nanospheres are significantly different ( $P < 0.0001$ ).

b:

Glycerol solution (mL)	Urea solution (mL)	TEM images of final products
2.5	7.5	
2.5	5	
5	5	

*Preparation of Partially Modified Poly- $\alpha$ , L-Glutamic Acid (mPGA)*

Thirty-two samples were received from Dr. Justin Jiang. Based on the samples' stability and sensitivity to radiation (see Chapter 4), two candidates (NO. 128A, NO. 132) were further selected and tested in Chapter 4 for use as coating materials.

The purpose of grafting a lipophilic group onto the polymer side chain was to reduce the hydrolysis rate of PGA molecules. Because natural PGA, which was planned to be used as a protective coating material for the nanospheres, undergoes hydrolysis in aqueous solutions, the PGA-coated nanospheres could lose their PGA coating before reaching the target tumor site, unless the PGA was partially modified. Thus, a lipophilic substituent group was introduced to the side chains to reduce the hydrolysis rate of PGA molecules, thus keeping the coating material intact to protect the nanospheres while they travel through the blood. The intention was to make them hydrolysable again once they reached their target, allowing them to resume biodegradation when and where needed. The selected lipophilic substituents used for this modification, therefore, were required to be chemical structures that could be removed by external x-ray irradiation post-modification, creating coating materials that were radiolysis-activated. The chemical bonds between the carboxyl groups on the side chains of PGA molecules and the lipophilic substituents selected for hydrophobic modification are radiation-activated (see Figure 3-3). For example, structures having a 2-oxoalkyl group as their functional group for this modification reaction readily undergo a one-electron reduction in a hypoxic environment (e.g. in a tumor microenvironment) in aqueous solution to release the 2-oxoalkyl group when external x-ray irradiation is applied<sup>197</sup>.

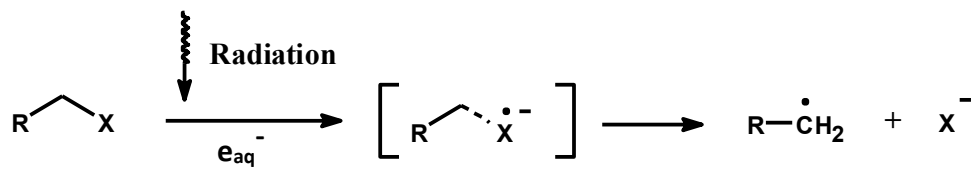


**Figure 3-3.** Schematic diagram of the radiolytic process. RCH<sub>2</sub> = selected lipophilic substituents; x = carboxyl group on the side chains of a PGA molecule.

### *Fabrication of mPGA@Gd:Mn and mPGA@Gd:Mn-Dox*

As the mPGA molecules are negatively charged and the nanospheres are positively charged, the mPGA molecules were grafted on the surface of the nanospheres through electrostatic force during the coating process (as illustrated in Figure 3-4). Figure 3-5 shows nanospheres (Figure 3-5a, b) with the mPGA (NO. 132) coating. They have a layer of mPGA coating wrapped around the nanospheres' surfaces. The Gd:Mn nanospheres (a) had a thicker coating (size increase) compared with the Gd:Mn-Dox nanospheres, as indicated in Table 3-2 (n=20, represented as mean  $\pm$  standard deviation). This is likely due to the Gd:Mn nanospheres having a stronger charge than the Gd:Mn-Dox nanospheres, as the doxorubicin molecules are negatively charged and could reduce the positive charge on the Gd:Mn nanospheres when incorporated into them.

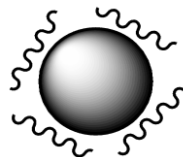


**Figure 3-4.** A schematic diagram showing a nanosphere surface coated with mPGA molecules.

 represents mPGA molecules, and  represents Gd:Mn or Gd:Mn-Dox nanospheres.

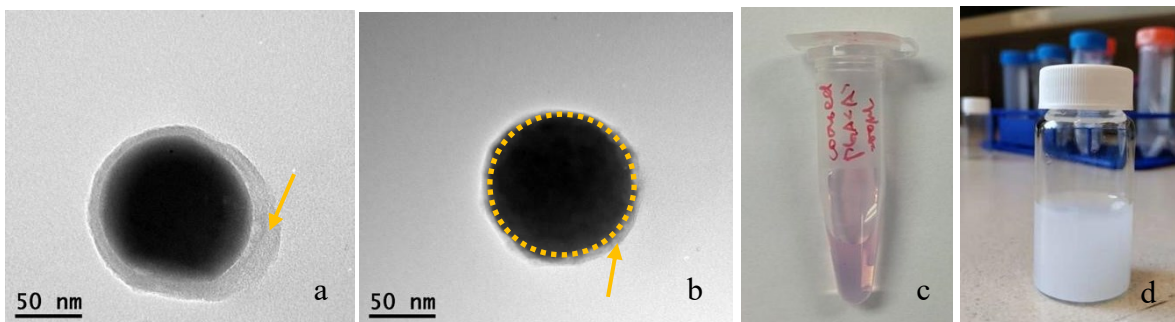


**Figure 3-5.** TEM images of mPGA (NO. 132) coated nanospheres. a and b show mPGA-coated Gd:Mn (a) and Gd:Mn-Dox (b) nanospheres; the arrows indicate layers of the polymer coating and the dashed circle shows the nanosphere core. c and d show mPGA coated Gd:Mn-Dox (c) and Gd:Mn (d) nanospheres suspended in ddH<sub>2</sub>O.

**Table 3-2.** Particles size of nanospheres before and after the coating procedure.

	Particle size (nm)	
	Gd:Mn	Gd:Mn-Dox
<b>Initial nanospheres</b>	114 ± 6	107 ± 18
<b>Coated nanospheres</b>	142 ± 29	128 ± 13

## Conclusions

In this chapter, doxorubicin loaded Gd:Mn-Dox nanospheres and surface coated mPGA@Gd:Mn and mPGA@Gd:Mn-Dox nanocomplexes were successfully synthesized, using a simple hydrothermal homogeneous coprecipitation method. Morphology and size were characterized via TEM and SEM. Near-spherical shaped monodisperse nanoparticles were produced. The effects of adding doxorubicin and varying the ratio of glycerol:urea on the final

products were explored. The synthesized nanospheres showed a decreased diameter after doxorubicin was added to the reaction system; while different ratios of glycerol:urea resulted in different morphologies and diameters of the final products.

## Chapter 4 – *In Vitro* Characterization of Fabricated Nanospheres

### Introduction<sup>2</sup>

Research in other labs has showed that lanthanide complexes, such as those containing gadolinium, are very promising in theranostics due to their versatility in biomedical application. Among the lanthanides, gadolinium is the most well-known element used for medical purposes. Gadolinium-based MRI contrast agents were first approved in the 1980s and are currently used at a rate of more than 30 million injections annually, which accounts for about 40% of the MRI investigations performed globally<sup>75</sup>. Gadolinium has seven unpaired electrons and a slow electron spin relaxation, which gives gadolinium the highest relaxation efficiency of all metals<sup>75</sup>. MR images are based on water proton densities in different tissues, and are obtained based upon the water proton relaxation rate differences in  $1/T_1$  (longitudinal) or  $1/T_2$  (transverse). Gadolinium can shorten the nuclear relaxation time through dipolar interactions with water protons both in  $T_1$  and  $T_2$  weighted MRI, and thereby significantly enhance the image contrast<sup>204</sup>.

Since radiation therapy relies heavily on imaging contributions, clinical strategies have already included MRI as a part of personalized cancer radiation therapy and assessment of cancer responses to the applied radiation dose and post-treatment management<sup>205</sup>. Furthermore, the idea of merging the radiotherapeutic capability of a linear accelerator (LINAC) with the visualizing capability of an MRI instrument (MR-LINAC – Magnetic Resonance Imaging Guided Linear Accelerator) has become a reality very recently. The first patient (with a glioblastoma) in Canada to be treated with MR-LINAC was treated in August 2019 at Sunnybrook Health Sciences Centre. For such strategic therapies to become part of regular practice, there will be an advancing need for novel agents that can perform both as imaging contrast agents and radiosensitizers. The

---

<sup>2</sup> Portions of this chapter were published in: Yuan *et al.*, 110s | CSPS/CC-CRS Conference 2016, Vancouver, BC, Canada.

successful development of such novel multi-role agents thereby could significantly advance this field of therapy.

Although the mechanisms behind how radiosensitizers act are not fully described yet, elements with high  $Z$  value (atomic number) have been the focus for development of radiosensitizers and have exhibited significant radiosensitization efficiency<sup>71-73</sup>. Among these elements, gadolinium appears to be a very attractive candidate for designing such multi-role nanocomplexes, due to its high  $Z$  value ( $Z = 64$ ) and paramagnetic property<sup>40</sup>. Nanocomplexes based on gadolinium chelates and nanocomplexes made of crystalline cores based on gadolinium have been fabricated and tested for MRI and/or radiosensitization<sup>82-87</sup>. In these previously reported studies, the grafted gadolinium chelates and gadolinium-based crystalline nanoparticles displayed the potential to significantly enhance MRI image contrast and inherited distinct properties from their nanoformulations, including prolonged half-lives, distinct biodistribution and specific excretion pathways. Many of the reported studies were devoted to either image contrast enhancement or multimodal imaging, but research focused on theranostic applications has started growing and it is believed that the use of gadolinium-based nanocomplexes in these applications could be cost-effective and hold great clinical potential<sup>40,88</sup>.

The multifunctional properties of gadolinium-based nanocomplexes developed in Chapter 3 are addressed in this chapter. *In vitro* measurements and experiments were carried out in this chapter to characterize the Gd:Mn, mPGA@Gd:Mn, Gd:Mn-Dox, and mPGA@Gd:Mn-Dox nanospheres fabricated in the previous chapter. The fabricated Gd:Mn and Gd:Mn-Dox nanospheres were subject to x-ray powder diffraction and Energy Dispersive X-ray Spectroscopy (EDXS) for crystalline structure and elemental analysis, respectively. Ultraviolet-visible (UV-Vis) spectroscopy was used to monitor changes during the process for synthesis of Gd:Mn-Dox

nanospheres. Irradiation-activated mPGA disintegration was assessed by measuring the absorbance changes of mPGA solutions before and after irradiation treatments using UV-Vis spectroscopy. The feasibility and potential of irradiation-activated low-pH-responsive doxorubicin release from mPGA@Gd:Mn-Dox nanocomplexes was investigated by measuring the doxorubicin cumulative release profile of radiation-treated mPGA@Gd:Mn-Dox nanocomplex samples in an acidic release medium. TEM, confocal microscopy and ICP-MS were employed to assess the *in vitro* cellular uptake of these nanocomplexes by human breast cancer cells. MTT and clonogenic assays were used for evaluating the synergistic anticancer efficacy of gadolinium and doxorubicin that are incorporated in the nanocomplexes. Flow cytometry was used for assessing the apoptosis rate of human breast cancer cells induced by the doxorubicin-loaded nanocomplexes. The *in vitro* MRI traceability of doxorubicin-loaded and non-loaded nanocomplexes were also explored via testing in clinical MRI and PET-MRI facilities.

## **Materials and Methods**

### *Materials*

Methanol, concentrated HCl (36.5 - 38.0%), agarose, MTT and cell culture dishes were purchased from Fisher Scientific. DMEM (Dulbecco's Modified Eagle Medium), FBS (fetal bovine serum), Trypsin-EDTA (ethylenediaminetetraacetic acid, 0.25%), Oregon Green 488, LysoTracker Green, and Annexin V were purchased from Invitrogen. Cell culture flasks were purchased from Corning. Ethanol (100%) was purchased from the University of Alberta Biochemistry Stores. Ethyl acetate, isopropanol, paraformaldehyde, OsO<sub>4</sub>, penicillin G and streptomycin were purchased from Sigma Aldrich. Gadavist was purchased from Bayer. USP

(United States Pharmacopeia) standard PBS solutions (phosphate buffer, pHs 4.5, 6.8 and 7.4) were supplied by the GLP (Good Laboratory Practice) lab at the University of Alberta. mPGA candidates selected were NO. 128A and NO. 132. The other materials used in this chapter were sourced as described in Chapters 2 and 3.

### *X-ray Powder Diffraction*

X-ray powder diffraction (XRD) analysis of the fabricated Gd:Mn nanospheres and Gd:Mn-Dox nanospheres was carried out on an Ultima IV Rigaku x-ray powder diffraction platform at 38 kV and 38 mA with a cobalt tube. The scan range ( $2\theta$ ) was from 5 to 65 degrees with a scan speed of  $2^\circ/\text{min}$ . Prior to XRD analysis, the nanosphere samples, made as described in Chapters 2-3, were dried in a vacuum oven and ground to powder prior to XRD analysis, as described in Chapter 2.

### *Elemental Analysis via Energy Dispersive X-ray Spectroscopy (EDS) and UV-Vis Spectroscopy of the Obtained Nanodispersions*

*Energy Dispersive X-ray Spectroscopy (EDS).* Gd:Mn-Dox nanosphere samples were analyzed using a Bruker Energy-Dispersive X-ray Spectroscopy (EDS) system mounted onto the Zeiss Sigma Field Emission Scanning Electron Microscope (Zeiss Sigma 300 VP-FESEM) that was used for the SEM studies described in Chapter 3.

*UV/Vis Spectroscopy Analysis.* The UV/Vis absorbances of the doxorubicin hydrochloride solution (used for fabricating Gd:Mn-Dox nanospheres), a mixed solution of  $\text{Gd}(\text{NO}_3)_3$  and doxorubicin hydrochloride solution – the reaction mixture used to create the

Gd:Mn-Dox nanospheres, and the final Gd:Mn-Dox nanodispersion were measured on a Beckman Coulter (DU730) UV/Vis spectrophotometer in the range of wavelengths from 400 nm to 750 nm. Brand™ standard plastic disposable cuvettes were used in this study and ddH<sub>2</sub>O was used for blank controls.

#### *Radiolytic Activation of the Modified PGA Candidates*

The received modified PGA (mPGA) candidates described in Chapter 3 were diluted to 0.2 mg/mL in ddH<sub>2</sub>O. 5 mL of each of the diluted mPGA sample solutions was transferred into a well of 6-well plates. Each sample was purged with argon gas for 15 minutes prior to applying irradiation. The mPGA samples were exposed to x-ray irradiation at different dose levels (from 0 to 30 Gy) using a Pantak Therapax3 orthovoltage irradiator (DXT-300). Once the irradiation treatment was done, 5 mL of ethyl acetate was added to each treated sample to extract the degraded lipophilic fragments that had previously been grafted onto the side chains of the PGA molecules. Quantitative analysis of the degraded lipophilic fragments was carried out on a Beckman Coulter UV/Vis spectrophotometer (DU-730) using ethyl acetate as a blank control. The original absorbance data (wavelengths measured from 250 to 400 nm) were integrated and normalized against the 0 Gy treatment group.

#### *In Vitro Low pH-Responsive Doxorubicin Release from mPGA-Coated Gd:Mn-Dox Nanospheres via Radiolytic Activation of the mPGA Coatings*

Gd:Mn-Dox nanospheres coated with two different mPGA coating materials (NO. 128A and NO. 132) were studied for x-ray irradiation-activated doxorubicin release in a low pH environment. mPGA@Gd:Mn-Dox nanospheres were dispersed in phosphate buffered saline

(PBS) at pH 4.5 (to mimic the acidic environment within a lysosome), in distilled water, and in PBS at pH 7.4, and then separated into the x-ray treatment group and non-x-ray control. The x-ray treatment group received a 30 Gy x-ray irradiation treatment, and the non-x-ray control group was brought with the x-ray treatment group to the radiation facility but did not receive x-ray irradiation. The samples were then kept at 37°C to allow for doxorubicin release. A Beckman Coulter UV/Vis spectrophotometer (DU-730) was used for quantifying doxorubicin release at 3, 6 and 9 days, as described above. The absorbances of each experimental group at 500 nm were converted to % Dox release by using the absorbance data at 500 nm for same quantity of Gd:Mn-Dox nanospheres fully dissolved in HCl as a reference point for 100% Dox release.

#### *Doxorubicin Stability Study*

The same solution containing doxorubicin, gadolinium and manganese used for Gd:Mn-Dox nanosphere fabrication was kept in the Teflon lined autoclave tube and placed into the oven for a day at the reaction temperature (120°C) at atmospheric pressure to test the stability of doxorubicin over the course of the reaction. The resulting solution was analyzed via HPLC (SHIMADZU SPD-M10AVP DAD) using the same method as described in Chapter 3 and compared with a freshly mixed solution for a similarity analysis. Another study was performed at a higher reaction temperature (130-140°C) using ICP-MS (inductively coupled plasma mass spectrometry) for the similarity study to analyze the stability of the doxorubicin under these conditions and check for its possible derivatives.

*In Vitro Cellular Uptake of Gd:Mn Nanospheres, Doxorubicin-Loaded Gd:Mn-Dox Nanospheres and Radiation Activated/Non-Activated mPGA@Gd:Mn-Dox Nanospheres using Confocal Laser Scanning Microscopy and Transmission Electron Microscopy*

*In vitro cell lines and cell culture conditions.* Human breast cancer cell lines (MCF-7 and MDA-MB-231) purchased from ATCC (American Type Culture Collection) were used for the investigation. DMEM (Dulbecco's Modified Eagle Medium, Invitrogen) fortified with fetal bovine serum (10%, Invitrogen), 100 UI penicillin G and 100 µg/mL streptomycin (1%, Sigma) were used for culturing the cells. The cells were maintained at 37°C and 5% CO<sub>2</sub> in Corning flasks in a humidified incubator. A Beckman Coulter cell counter was used for cell counting. Human breast cancer cells used throughout the investigation were all cultured in the same manner, unless otherwise specified.

*In Vitro Cellular Uptake Analysis of mPGA@Gd:Mn Nanospheres.* ICP-MS (inductively coupled plasma mass spectrometry) and TEM (transmission electron microscopy) were employed for studying the *in vitro* cellular uptake of the mPGA@Gd:Mn nanospheres coated with mPGA NO. 132.

2×10<sup>6</sup> MCF-7 cells were plated per 100 mm cell culture dish and incubated to reach 70% confluence. Then the cells were incubated with either mPGA@Gd:Mn nanospheres or x-ray activated mPGA@Gd:Mn nanospheres for two hours. After treatment, the cells were washed twice with PBS (pH 7.4) to remove any free nanospheres that had not been taken up by the cells. Then the cells were detached using 0.5 mL of 0.25% Trypsin-EDTA and washed and resuspended in PBS to a final volume of 5 mL prior to the addition of 5 mL hydrochloric acid

(30%, Fisher Brand). The cells, and nanospheres internalized inside the cells, were allowed to dissolve overnight. The gadolinium content in each sample was analyzed using ICP-MS (Elan6000, PerkinElmer). For the cellular uptake study by means of TEM, the treated cells were gathered by centrifugation (Thermo IEC CL3R, at 200xg for 5 min). and fixed in precooled formaldehyde (4°C, 4% v/v, Sigma) for four hours at 4°C. The preparation and staining procedures were carried out as previously described<sup>29</sup>: Briefly, the cells were washed and resuspended in OsO<sub>4</sub> (1% in pH 7.4 PBS) and incubated for one hour at ambient temperature; the cells were then washed twice with PBS (pH 7.4), resuspended in pre-warmed agarose (2% w/v) and spread on the surface of glass slides to cool down. The small cooled pieces of gel containing the cells were harvested and dehydrated with gradient ethanol prior to being embedded and infiltrated with Spurr's resin. A Leica ultramicrotome (EM UC6) was used to section the cell-embedded resin. The sliced sections were then stained with uranyl acetate and lead citrate prior to the final TEM characterization as described above.

*In Vitro Cellular Uptake Analysis of Gd:Mn-Dox Nanospheres.* TEM and CLSM (confocal laser scanning microscope, Zeiss LSM 710) were employed for studying the *in vitro* cellular uptake of the Gd:Mn-Dox nanospheres.

TEM characterization of the cellular uptake of Gd:Mn-Dox nanospheres was carried out using the same method as described above.

For the CLSM study, MCF-7 cells were seeded on coverslips placed in 6-well plates, and incubated overnight prior to treatments, as described above. The cells were treated with Gd:Mn-Dox nanospheres for select periods of time (6, 24 and 72 hours) before the cells were washed with phosphate-buffered saline (PBS, pH 7.4) and fixed in paraformaldehyde (PFA, 4% v/v).

The fixed cells were stained with either Oregon Green 488 (cell membrane dye from Invitrogen) or LysoTracker™ Green (lysosome dye from Invitrogen). The staining procedures were carried out following manuals & protocols for Oregon Green 488 or LysoTracker™ Green. A mounting medium fortified with DAPI (cell nucleus dye) was used to mount the samples on glass slides for confocal microscopy studies as previously described<sup>83</sup>. Control groups were incubated with either doxorubicin solution or Gd:Mn nanospheres that did not have doxorubicin. In the Gd:Mn-Dox nanospheres treated group, the LysoTracker™ Green, a molecular fluorescence dye that actively binds with cell lysosomes, was used to track the cell lysosomes to help determine the subcellular location of the internalized nanospheres.

#### *In Vitro Cytotoxicity and Biocompatibility Studies*

##### *Biocompatibility of Gd:Mn Nanospheres and the Selected mPGA Using MTT Assay.*

Cells were seeded at a density of 3000 per well with 200  $\mu$ L culture medium in 96-well plates. Once the cells reached 70% confluence, the culture medium was replaced with 150  $\mu$ L of fresh medium containing either mPGA (NO. 132), Gd:Mn nanospheres, or mPGA@Gd:Mn nanospheres at select concentrations (mPGA: from 10 to 300  $\mu$ g/mL, nanospheres: from 0 to 700  $\mu$ g/mL). The culture medium was removed again after 48 hours of incubation prior to adding 100  $\mu$ L of MTT (3-(4,5-Dimethylthiazol-2-yl)-2,5-diphenyltetrazolium bromide)-containing (1.2 mM MTT) culture medium. After three hours of further incubation with MTT, the MTT-containing medium was replaced with 100  $\mu$ L of 0.1 N HCl in isopropanol. A plate reader (Bio-Tek EL 808) was used to assess the absorbance of each well at a test wavelength of 550 nm. Absorbance values were normalized to percent viability against the control (untreated) group.

*In Vitro Radiation Enhancement Effect of Activated mPGA@Gd:Mn Nanospheres (mPGA NO. 132).* A clonogenic cell survival assay and an MTT cell viability test were employed to test the radiation enhancement effect of non-doxorubicin loaded Gd:Mn nanospheres. For the clonogenic assay, cells were seeded as 400 cells per Petri dish (100 mm) and left in an incubator overnight. A saline control group was treated with saline while the radiation control group was treated with 5 Gy x-ray irradiation only. The other two groups were treated with either mPGA@Gd:Mn nanospheres or activated mPGA@Gd:Mn nanospheres followed by a 5 Gy irradiation one day after the nanosphere treatment. All cells were further incubated for a week prior to being fixed with methanol (Fisher Scientific) and stained with crystal violet (0.5%), as described previously<sup>83</sup>. Cell colony numbers were counted using FIJI ImageJ image processing software<sup>177</sup>. For the MTT test, a typical MTT assay procedure was used, as described above. The experimental groups were the same as the groups used in the clonogenic assay described in this section. Nanosphere-containing medium was removed and replaced with fresh culture medium after two hours of incubation. The cells were incubated for 48 hours after the irradiation treatment prior to the final measurement.

*In Vitro Cytotoxicity and Biocompatibility of Doxorubicin-Loaded Gd:Mn Nanospheres.* For the cytotoxicity testing of Gd:Mn-Dox and mPGA@Gd:Mn-Dox nanospheres, a cell apoptosis assay using Annexin V staining was performed. 500,000 cells were seeded in each Corning T-25 flask and incubated overnight before being treated with saline or 500 µg/mL of Gd:Mn-Dox or mPGA@Gd:Mn-Dox nanosphere dispersions. After three days of incubation under the same conditions, dead cells floating in the culture medium were collected and counted by a Beckman Coulter cell counter. The rest of the cells remaining attached to the flasks were

treated with 0.25% trypsin-EDTA in order to detach them. The detached cells were collected and stained with allophycocyanin Annexin V conjugate (Invitrogen) for cell apoptosis analysis carried out on a Becton Dickinson flow cytometer (FACS Canto II) using the FITC and APC channels.

#### *In Vitro Magnetic Resonance Imaging (MRI)*

*In vitro* T<sub>1</sub>-weighted magnetic resonance imaging (MRI) of Gd:Mn nanospheres was carried out in a 1.5 T Siemens Medical System using a spin-echo sequence (TE: 9.6 ms; TR: 401 ms) at the University of Alberta Cross Cancer Institute MRI facility. *In vitro* T<sub>2</sub>-weighted magnetic resonance imaging of Gd:Mn-Dox nanospheres was performed in a 3 T Siemens Medical System Positron Emission Tomography (PET)-MRI facility using a spin-echo sequence (TE: 13 ms; TR: 750 ms). Prior to performing the MRI scans, nanosphere dispersion samples were diluted with PBS containing 1% agarose to concentrations as indicated in Figure 4-11.

A proof-of-concept study examining the pH-sensitivity of gadolinium release was performed on a 1.5 T Siemens Medical System at the University of Alberta Cross Cancer Institute MRI facility using the same settings. Gd:Mn-Dox nanospheres were suspended in either HCl (3.6 – 3.8%) or PBS (pH 4.5) for MRI scans alongside water and Gadavist (Bayer). The pH 4.5 buffer was used to mimic the acidic environment in lysosomes, where nanospheres that have been internalized by cells would be located.

## Results & Discussion

### *X-ray Powder Diffraction*

Broad diffraction peaks were obtained during the XRD analysis of both the Gd:Mn nanospheres and the Gd:Mn-Dox nanospheres. No crystalline diffraction peaks were detected in the study. The diffraction patterns of both types of nanospheres are shown in Figure 4-1. Both types of nanospheres had weak scattering spread throughout the reciprocal space. All this indicated that the synthesized Gd:Mn nanospheres and Gd:Mn-Dox nanospheres are amorphous substances.

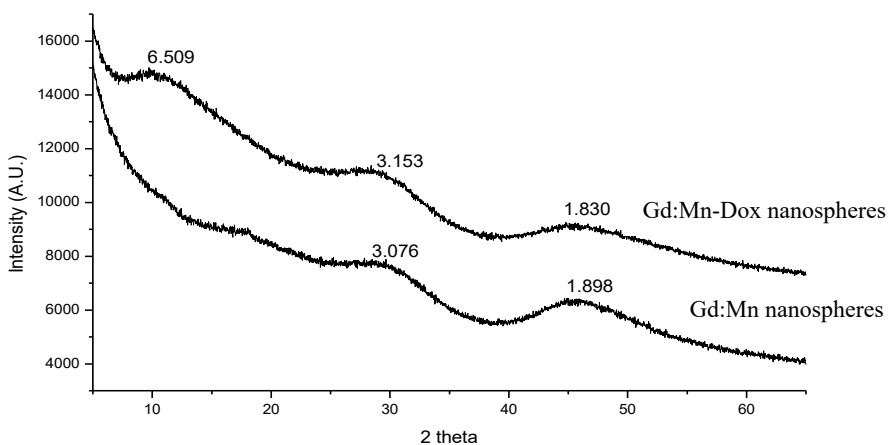


**Figure 4-1.** X-ray powder diffraction patterns of Gd:Mn nanospheres and Gd:Mn-Dox nanospheres.

Since the Gd:Mn-Dox nanospheres were designed to be responsive to acidic pH and to thus trigger the release of the payload (the Gd<sup>3+</sup>-Dox drug-metal complexes) as the nanospheres dissolve, the solubility or the dissolution rate is a crucial factor which governs the final effect of the payload. Unlike the Gd(OH)<sub>3</sub>:Mn series of nanorods and nanocomplexes developed in

Chapter 2, which were crystalline substances (see their XRD patterns in Chapter 2), these newly developed amorphous nanospheres have favourable characteristics for the intended application: Amorphous substances do not possess the long-range order of crystalline structures, and therefore require less energy to be dissolved, resulting in an innate better solubility than crystalline forms<sup>201,202</sup>.

*Elemental Analysis via Energy Dispersive X-ray Spectroscopy (EDS) and UV/Vis spectroscopy of the Obtained Nanodispersions*

*Energy Dispersive X-ray Spectroscopy (EDS).* The EDS elements mapping data, shown in Figure 4-2, indicated that gadolinium was present and evenly dispersed in the Gd:Mn-Dox nanospheres.

a:

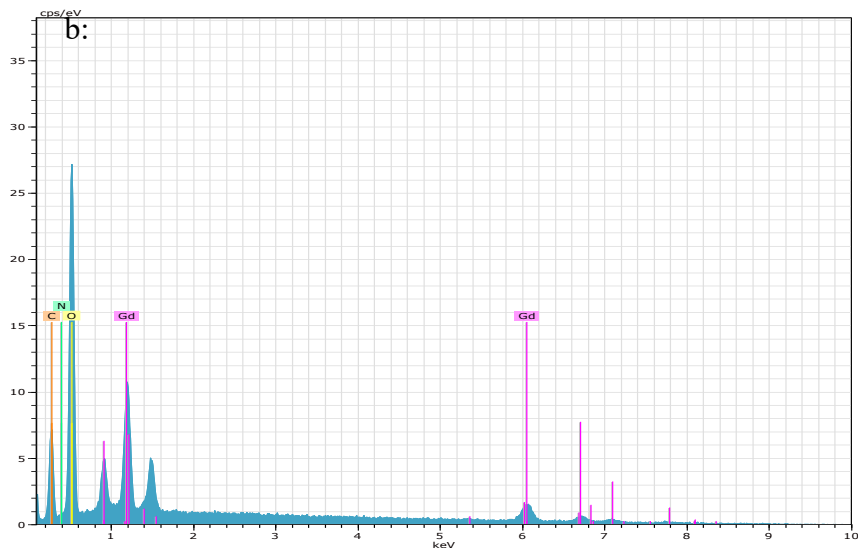
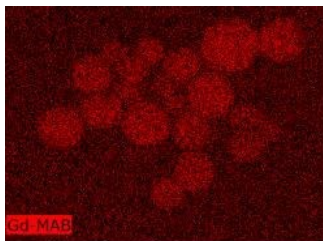


**Figure 4-2.** Energy-dispersive x-ray spectroscopy (EDS) elements mapping of the synthesized Gd:Mn-Dox nanospheres. a: gadolinium mapping; b: EDS element spectra. Note: The Mn was not detected as it is present at trace levels in the nanospheres.

*UV/Vis Spectroscopy Analysis of the Obtained Gd:Mn-Dox Nanodispersion.* In Figure 4-3, in comparison with the pure doxorubicin solution UV/Vis spectrum (red curve), the adding of the gadolinium solution did not make any change to the spectrum (orange curve). The further addition of urea and glycerol solutions to the mixture of gadolinium and doxorubicin, to create the final reaction mixture, resulted in the appearance of a small absorbance peak to the spectrum

(green curve) at around 575 nm. Once the reaction was complete, the absorbance peaks flattened (purple curve) as the doxorubicin was integrated into the synthesized solid nanospheres.

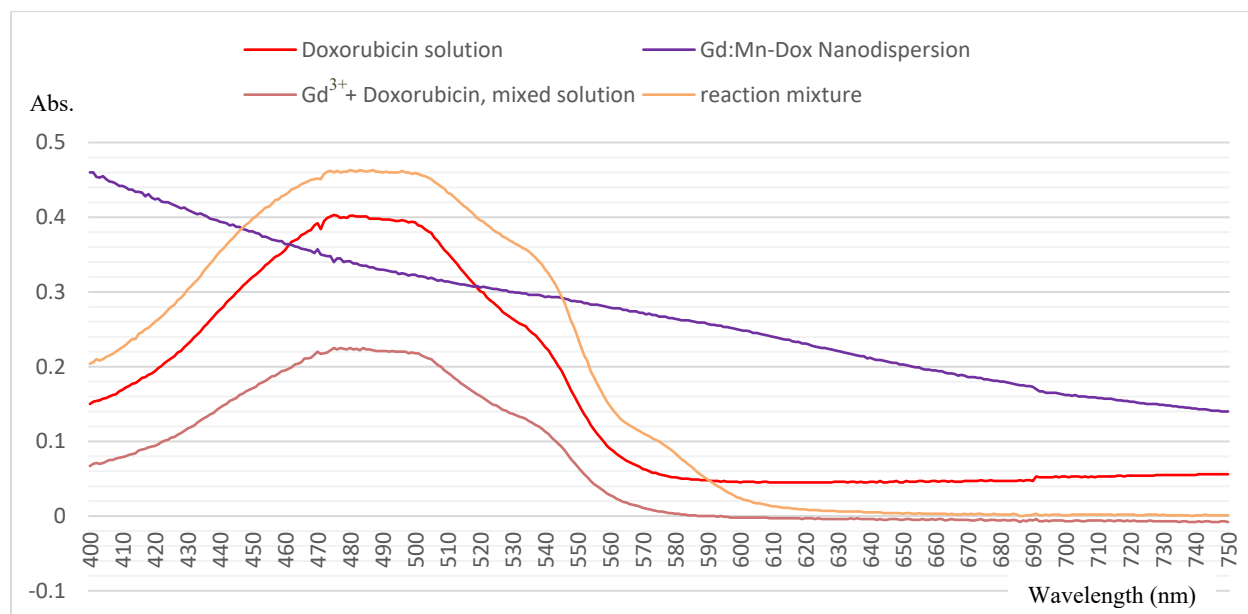
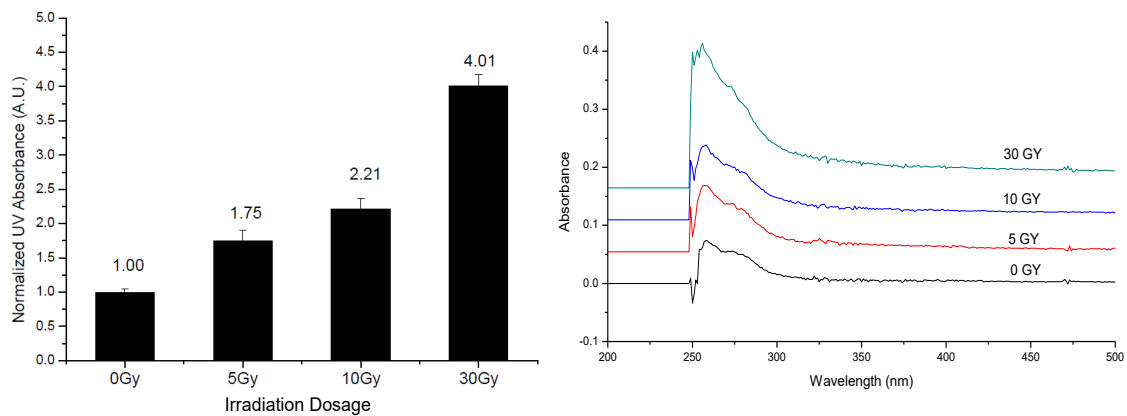


**Figure 4-3.** UV/Vis absorption spectra of doxorubicin hydrochloride solution (red), Gd(NO<sub>3</sub>)<sub>3</sub>+doxorubicin mixed solution (orange), the final reaction mixture (green), and the resulting Gd:Mn-Dox nanodispersion (purple).

#### *Radiolytic Activation of the Modified PGA Candidates*

Two mPGA candidates (NO. 128A, NO. 132) were selected from the test samples to demonstrate the x-ray irradiation-induced reduction of the modified PGA. Figure 4-4 shows the UV/Vis spectrum of each irradiated/degraded sample after different irradiation doses; the bar graphs show the degree of radiolysis of each sample after receiving different irradiation doses. A higher dose of irradiation means more energy was applied to the test samples, thereby inducing a higher degree of activation/degradation. This experiment demonstrated the feasibility of removing the coating material using external irradiation.

**a:**



**b:**

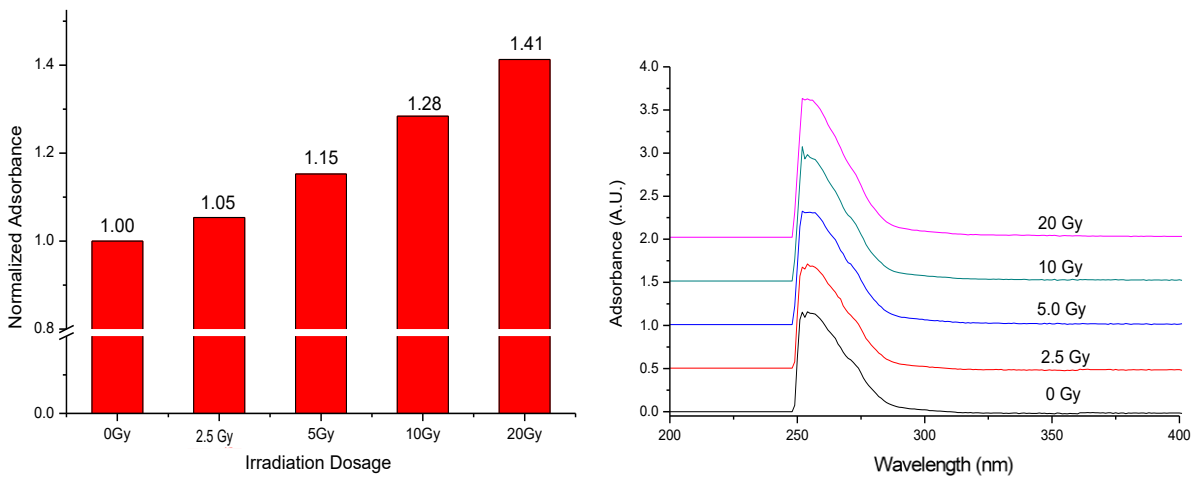


**Figure 4-4.** Impact of different doses of x-ray irradiation on irradiation-induced degradation of selected mPGA candidates (**a:** NO. 132 & **b:** NO. 128A). The bar graphs on the left plot normalized absorbance at 258 nm after different irradiation doses, and the full absorbance scan after different irradiation doses is shown on the right for **a** (top) and **b** (bottom).

*In Vitro Low pH-Responsive Doxorubicin Release from mPGA-Coated Gd:Mn-Dox Nanospheres via Radiolytic Activation of the mPGA Coating*

For the release studies carried out at pH 7.4 and in ddH<sub>2</sub>O, no detectable quantity of doxorubicin was released, which suggests high stability in a physiological pH environment, which may improve the biocompatibility of the mPGA-Coated Gd:Mn-Dox nanospheres by preventing premature release of the active agent. Figure 4-5 shows the release profile of doxorubicin from the mPGA (NO. 128A, NO. 132)-coated Gd:Mn-Dox nanospheres in the pH 4.5 phosphate buffered saline. The nanospheres provided a sustained release of doxorubicin, as desired, with limited premature release. In comparing the x-ray treated group to the untreated group, the x-ray treatment activated a significant increase in the release of doxorubicin due to the radiolytic activation of the surface coating. Together, these results suggest that the mPGA@Gd:Mn-Dox nanospheres can be activated at a desired location by precisely applied external irradiation, allowing the nanospheres to release the active agent into the acidic environments present in lysosomes and tumour microenvironments<sup>206,207</sup>. This should reduce toxic effects on healthy tissues that would occur if the doxorubicin was released prior to irradiation at the tumour site and was able to act throughout the body.

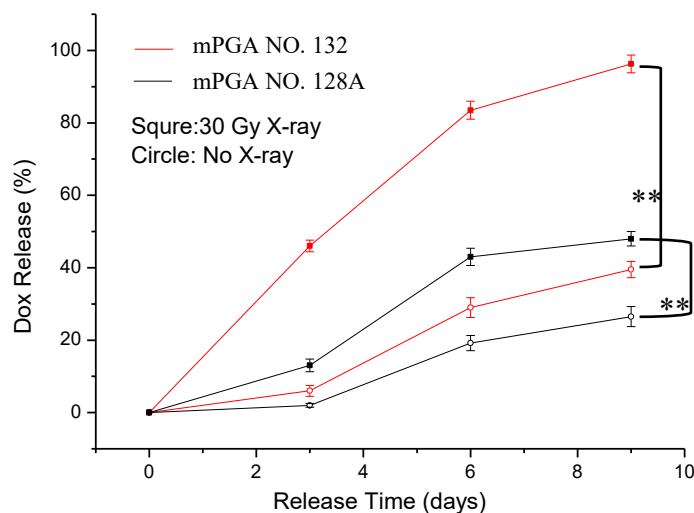


**Figure 4-5.** Release profiles of doxorubicin from two different types of mPGA coated Gd:Mn-Dox nanospheres with or without 30 Gy of x-ray irradiation in pH 4.5 phosphate buffered saline, over a nine day period. \*\* The mean values of the two groups indicated are significantly different ( $p < 0.0001$ ).

#### *Doxorubicin Stability Study*

The similarity between the freshly made solution and the solution kept under reaction conditions was 1.0000 according to the analytical result from the HPLC detector, which meant the doxorubicin was stable for one day of exposure to the reaction conditions. The same result was observed from the test analyzed via mass spectrometry.

*In Vitro Cellular Uptake of Gd:Mn Nanospheres, Doxorubicin-Loaded Gd:Mn-Dox Nanospheres and Radiation Activated/Non-Activated mPGA@Gd:Mn-Dox Nanospheres using Confocal Laser Scanning Microscopy and Transmission Electron Microscopy*

*In Vitro Cellular Uptake Analysis of mPGA@Gd:Mn Nanospheres using mPGA NO. 132.*

The subcellular locations of the internalized nanospheres were visualized using TEM. The micrographs in Figure 4-6 are TEM images of cells showing that the nanospheres were internalized and retained inside the cells. Most of the internalized nanospheres were observed in vesicular subcellular structures inside the cell plasma. Figure 4-6E shows the ICP-MS quantitative results for gadolinium in the cell lysate samples, and reflects the quantity of internalized nanospheres in each experimental group. The control group had no gadolinium, as it was only treated with PBS. After two hours of exposure to the treatments, the average gadolinium content was 1.78  $\mu\text{g}$  in the mPGA@Gd:Mn treated group and 4.96  $\mu\text{g}$  in the x-ray activated mPGA@Gd:Mn treated group. Thus, an increased uptake was measured in the x-ray activated mPGA@Gd:Mn nanospheres. Note that the only change in this group was the activation of the nanospheres. It is hypothesized that by promoting the breakdown of the mPGA coating, x-ray activation helped expose the positively charged Gd:Mn nanosphere cores, promoting interaction with the negatively charged cell membranes<sup>208,209</sup>, and thereby resulting in the increased uptake. Other possible reasons for the increased uptake also can be deduced: The mPGA residues on the surface of the activated nanoparticles could also help promote the interactions between the nanosphere and the cell membrane, as electrostatic interactions appeared to promote adherence of most of the activated nanospheres to the cell membrane during the washing process, whereas the non-activated nanospheres retained the negative surface charge

and the hydrophilic mPGA surface coating, which could promote the washing away of the non-activated mPGA@Gd:Mn nanospheres.

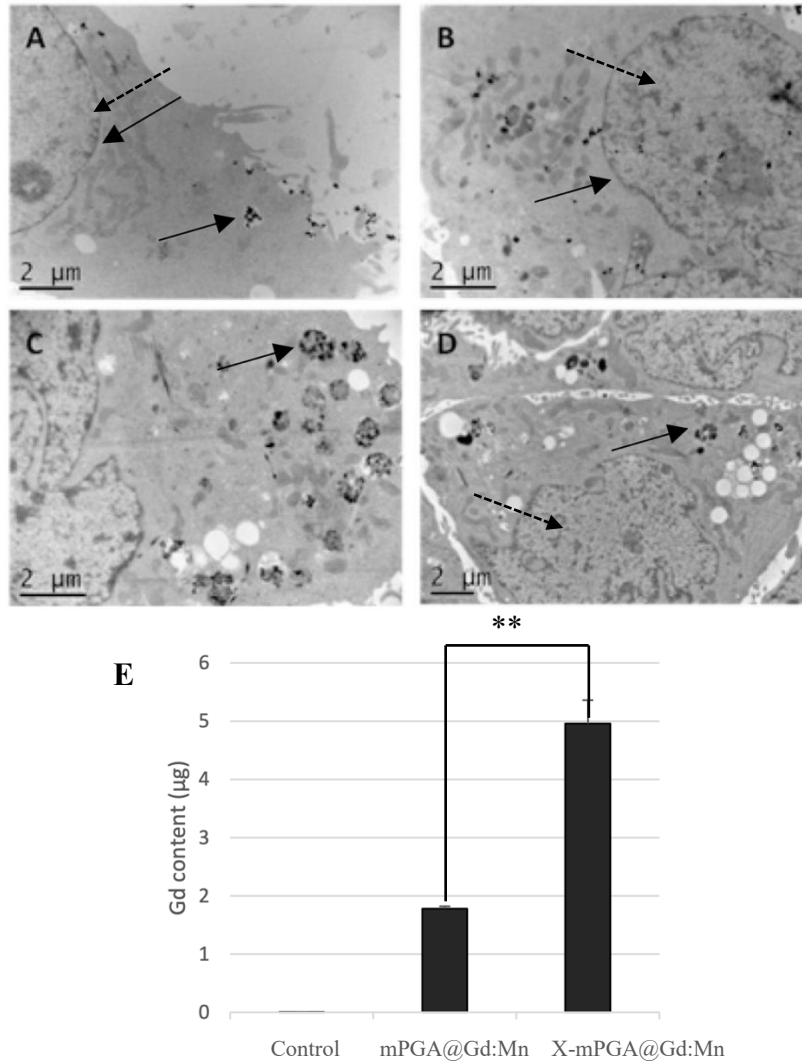


**Figure 4-6.** TEM images of cellular uptake of mPGA@Gd:Mn nanospheres (A, B) and x-ray activated mPGA@Gd:Mn (x-mPGA@Gd:Mn) nanospheres (C, D). Dotted and black arrows indicate cell nuclei and nanospheres (solid black spheres), respectively, internalized in vesicular structures within the cytoplasm, i.e. at a subcellular level. E shows the ICP-MS results measuring the quantity of internalized gadolinium in the control (non-treated) group, mPGA@Gd:Mn nanospheres treated group, and activated x-mPGA@Gd:Mn nanospheres treated group. \*\* The mean values of these two groups are significantly different ( $p < 0.0001$ ).

*In Vitro Cellular Uptake Analysis of Gd:Mn-Dox Nanospheres.* The Gd:Mn nanospheres control group, which did not include doxorubicin, did not have any fluorescence signal detected by CLSM (Figure 4-7A, right) other than DAPI, which stains cell nuclei, as the Gd:Mn nanospheres do not have the ability to emit fluorescence. In the doxorubicin solution (2 mg/mL, 5  $\mu$ L) treated control group, doxorubicin signals (red) and DAPI (blue) were detected (Figure 4-7A, left). Figure 4-7B shows confocal fluorescence micrographs from the experimental groups incubated with Gd:Mn-Dox nanospheres for a various time periods. After the longer incubation time of 24 hours (Figure 4-7B, right), a considerable number of Gd:Mn-Dox nanospheres had been internalized by the cells, relative to the 6 hour incubation group (Figure 4-7B, left), as indicated by the red fluorescence located within the cells. Both the micrographs were taken as representatives from a 3D Z-stack scan of the samples, which also indicated that all the fluorescence signals were coming from inside the cells. TEM results (Figure 4-7C) also confirmed the cellular uptake of the Gd:Mn-Dox nanospheres, with the nanospheres being distributed within vesicular structures in the cytoplasm. In the Gd:Mn-Dox nanospheres treated group, LysoTracker Green, a molecular fluorescence dye that actively binds with cell lysosomes, was also used to locate the cell lysosomes, in order to confirm the subcellular location of the internalized nanospheres. As demonstrated in Figure 4-7D, the doxorubicin signal (red) overlapped with the LysoTracker signal (green), which indicated that the Gd:Mn-Dox nanospheres were internalized by the cells through the endocytic pathway, resulting in their presence in cell lysosomes. All these data, taken together, demonstrate that the Gd:Mn-Dox nanospheres are readily internalized by MCF-7 human breast cancer cells through endocytosis.

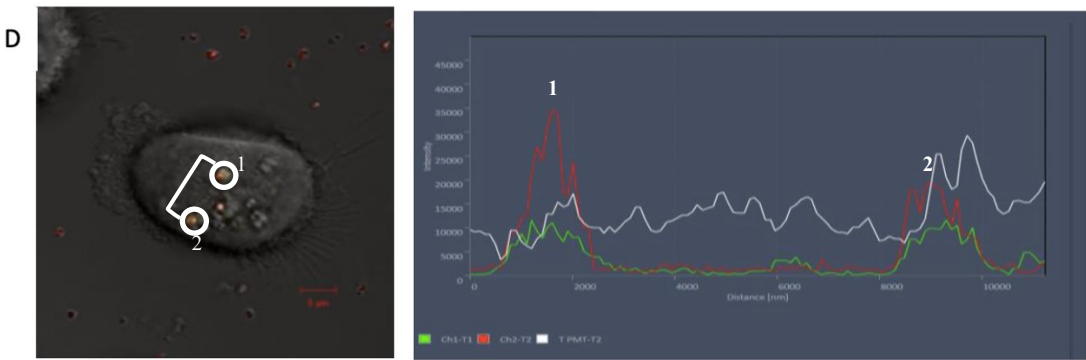
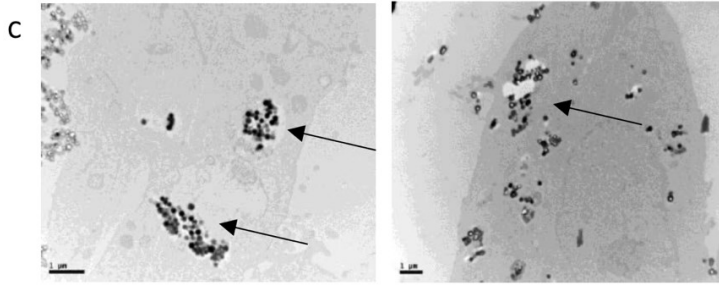
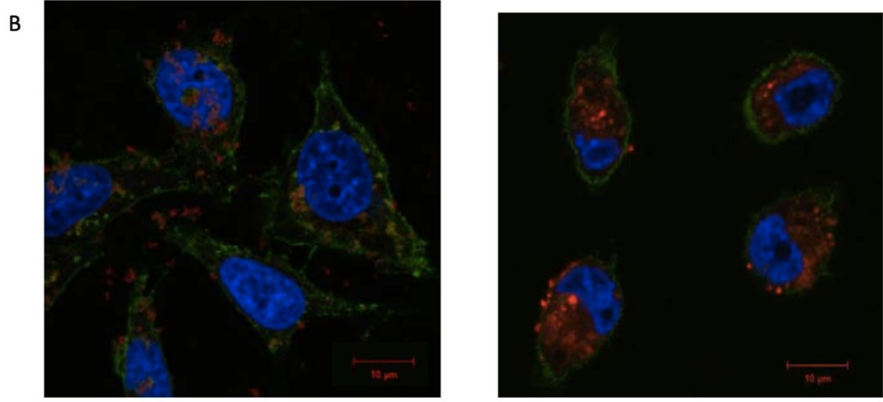
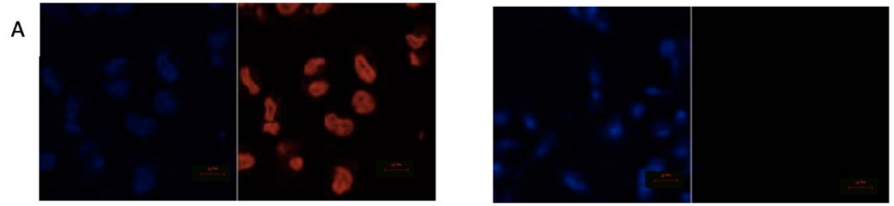


**Figure 4-7.** CLSM (A, B and D) and TEM (C) analysis of cellular uptake of Gd:Mn-Dox nanospheres. A: Control cells treated with doxorubicin solution (two micrographs on the left) and Gd:Mn nanospheres without doxorubicin (two micrographs on the right). B: Cells incubated with Gd:Mn-Dox nanospheres for 6 hours (left) and 24 hours (right). C: Black arrows indicate the internalized Gd:Mn-Dox nanospheres (small black spheres) in the vesicular structures within cell cytoplasm. D: Fluorescence profile analysis from point 1 to point 2. Points 1 and 2 are two lysosomes containing Gd:Mn-Dox nanospheres (as indicated by the overlapping doxorubicin red and LysoTracker Green signals). Fluorescence signals: Blue = DAPI, Red = Doxorubicin (in A) or Gd:Mn-Dox nanospheres (in B), Green = Oregon Green (in B) or LysoTracker Green (in D).

#### *In Vitro Cytotoxicity and Biocompatibility*

##### *In Vitro Biocompatibility of Gd:Mn Nanospheres and the Selected mPGA (NO. 132)*

*Using an MTT Assay.* Figure 4-8 demonstrates that the mPGA coating material, Gd:Mn nanospheres and mPGA-coated Gd:Mn (mPGA@Gd:Mn) nanospheres were non-toxic at test concentrations. The highest concentration that was tested for both the Gd:Mn and the mPGA@Gd:Mn nanosphere dispersion was 700  $\mu\text{g}/\text{mL}$ . The cell viability in that group was no less than 90%. This agrees with observations by other researchers in biocompatibility studies of modified polyglutamic acid and gadolinium-based nanoparticles<sup>168,196,210–214</sup>.

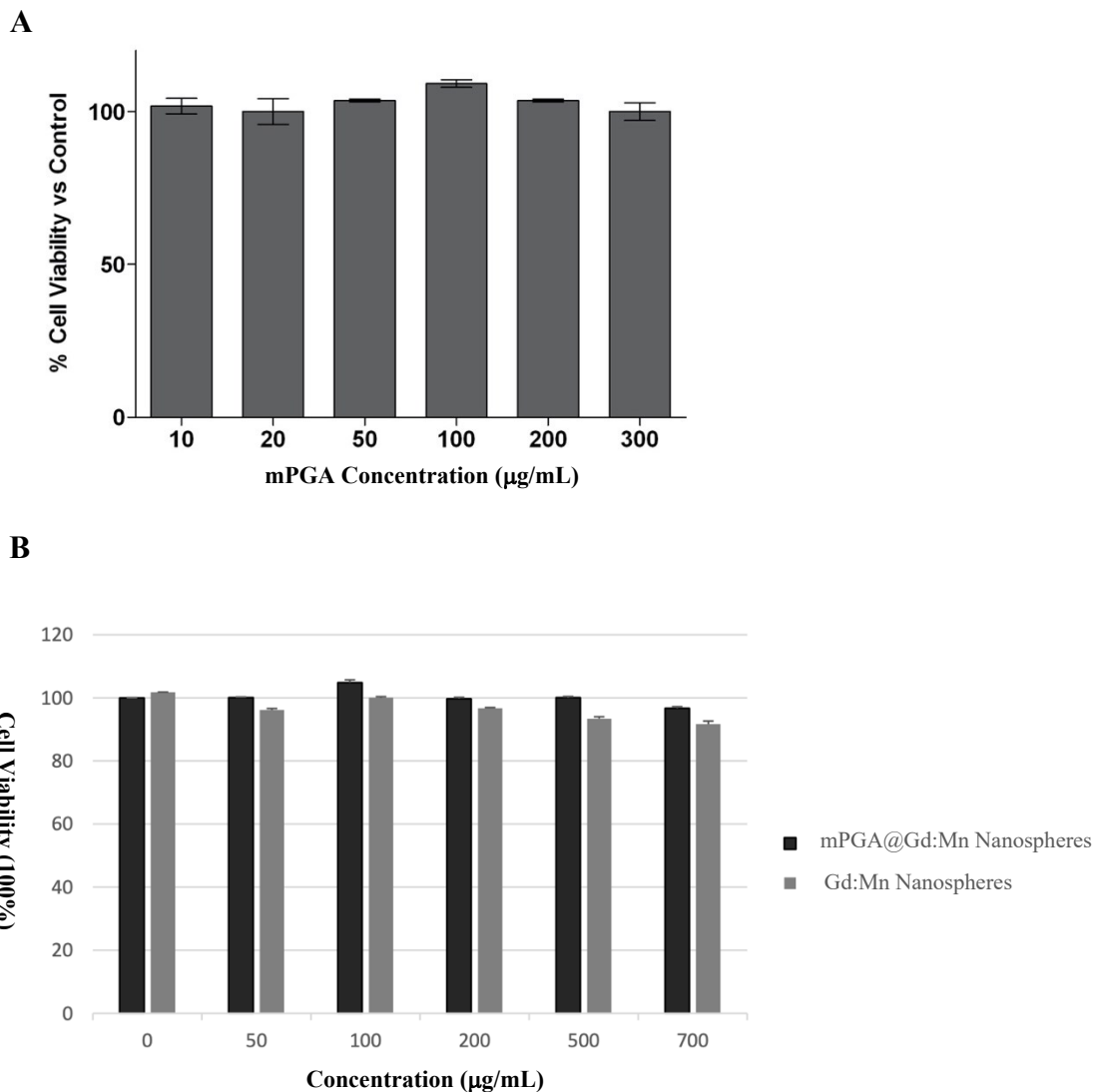


**Figure 4-8.** Biocompatibility study results of mPGA (A), Gd:Mn nanospheres and mPGA@Gd:Mn nanospheres (B) using an MTT assay against an MCF-7 human breast cancer cell line.

*In Vitro Radiation Enhancement Effect of Activated mPGA@Gd:Mn Nanospheres.* The results of both the MTT test and the clonogenic assay were compared to the control groups (see Figure 4-9). The control groups received either saline or x-ray irradiation treatment, while the

experimental groups were treated with either mPGA@Gd:Mn nanospheres or activated mPGA@Gd:Mn (x-mPGA@Gd:Mn) nanospheres followed by 5 Gy irradiation. The MTT test was used for cell viability testing (Figure 4-9A), and the clonogenic assay was used to test for cell proliferation (Figure 4-9B). Compared with the saline control group and the x-ray control group, the irradiated experimental treatments inhibited cell viability and proliferation, with the activated nanospheres showing a stronger inhibition than the ones which had not been activated. The biocompatibility study (see Figure 4-8) indicated that both the mPGA and Gd:Mn nanospheres were relatively biologically inert. In addition, gadolinium has been extensively studied for use as a radiation sensitizer<sup>67,73,211</sup>. The increased inhibitory effect, seen in the nanospheres which had not been activated, could be the result of gadolinium-based nanospheres locally enhancing the radiation that was applied to the cells, thus amplifying the inhibitory effect from the irradiation. The fact that the x-mPGA@Gd:Mn (activated) group exhibited stronger inhibitory effects comparing with the mPGA@Gd:Mn (non-activated) group may be because the cells in the activated group had a larger quantity of internalized nanospheres, as was observed in the cellular uptake study (see Figure 4-6). Also, since the gadolinium-based core was caged by the mPGA coating, the polymer may have prevented interaction between the gadolinium and surrounding water molecules prior to radiation.

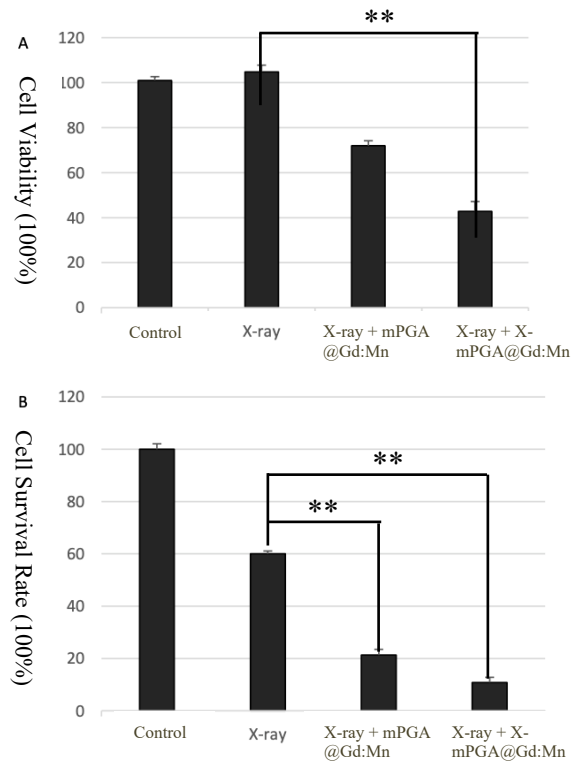


**Figure 4-9.** *In vitro* radiation enhancement effect of unloaded Gd:Mn nanospheres using an MTT test (A) and a clonogenic assay (B). Results are shown for the saline (Control), x-ray (X-ray), x-ray plus mPGA@Gd:Mn nanospheres (X-ray + mPGA @Gd:Mn) and x-ray plus x-ray activated mPGA@Gd:Mn nanospheres (X-ray + X-mPGA@Gd:Mn) treated groups. \*\* The mean values of the indicated groups are significantly different ( $p < 0.0001$ ).

*In Vitro Cytotoxicity and Biocompatibility of Doxorubicin-Loaded Gd:Mn Nanospheres.*

Figure 4-10 compares the percentage of cells undergoing apoptosis between the experimental groups and a PBS control. The apoptosis rate in the Gd:Mn-Dox nanospheres treated group increased proportionally with increasing concentration of the nanospheres. Since the Gd:Mn

nanospheres are relatively non-toxic, the induction of apoptosis was likely due to the release of doxorubicin. In the mPGA@Gd:Mn-Dox treated group, no trend was observed with increased concentration of the nanospheres, and the cells tolerated the nanospheres at all test concentrations much better than the nanospheres that were not coated with mPGA. The coating material itself is non-toxic. Based on the release profile (see Figure 4-5), doxorubicin release from the coated nanospheres was minimal over a three-day time period. Thus, the lower toxicity in the mPGA@Gd:Mn-Dox relative to the Gd:Mn-Dox was likely because the surface coating slowed down the dissolution of the caged Gd:Mn-Dox nanosphere core, preventing release of the doxorubicin payload.

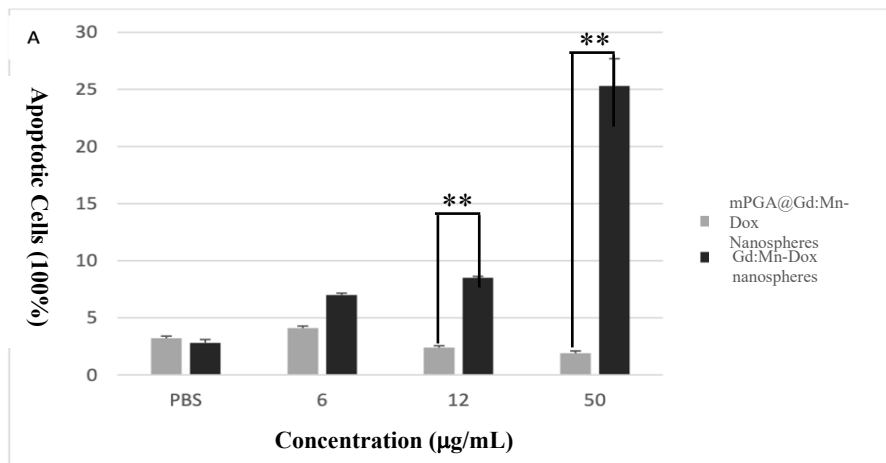


**Figure 4-10.** Percentage of MCF-7 cells undergoing apoptosis after three days exposure to various concentrations of Gd:Mn-Dox and mPGA@Gd:Mn-Dox nanospheres. \*\* The mean values of the indicated groups are significantly different ( $p < 0.0001$ ).

### *In Vitro Magnetic Resonance Imaging (MRI)*

Since gadolinium can shorten both  $T_1$  and  $T_2$  relaxation times in MRI, the  $T_1$  shortening effect of the Gd:Mn nanospheres and the  $T_2$  of the doxorubicin-loaded nanospheres were measured (Figure 4-11). In both  $T_1$  and  $T_2$  weighted MRI experiments, the gadolinium-based nanospheres demonstrated concentration-dependent shortening effects on relaxation times when comparing the experimental groups with the water control group. In  $T_1$  weighted images (Figure 4-11A), the image brightness level (which refers to image contrast in  $T_1$ ) increased as the concentration of the Gd:Mn nanospheres increased, while the image darkness level (which refers to image contrast in  $T_2$ ) increased as the concentration increased in the  $T_2$  weighted images (Figure 4-11B).

Figure 4-11C shows the MRI signal intensity of the tested Gd:Mn-Dox nanospheres. pH 4.5 buffer was used to mimic a situation in which the nanospheres were internalized and trapped in cell lysosomes. Gd:Mn-Dox nanospheres were wholly dissolved in HCl as a control group. Similar signal intensities were observed in both the experimental group (pH 4.5), and the control group (HCl) at the concentration range tested, which suggests the acidic environment in cell lysosomes with a pH of 4.5 could fully unleash the MRI contrast enhancement effect of the Gd:Mn-Dox nanospheres.

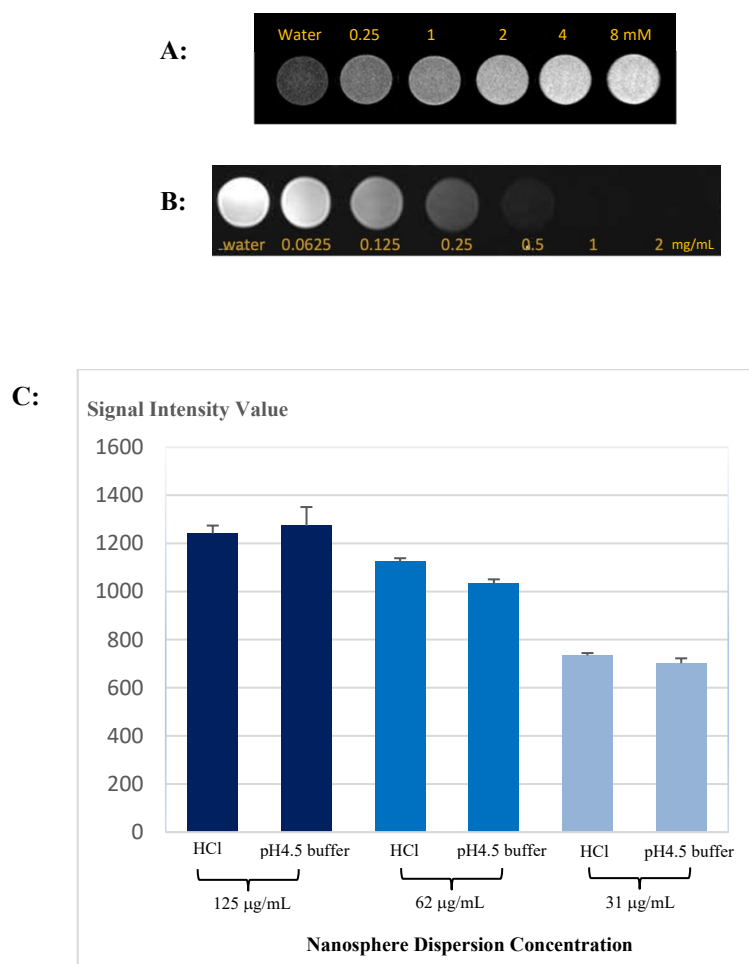


**Figure 4-11.** T<sub>1</sub>-weighted MRI images of Gd:Mn nanospheres (A) and T<sub>2</sub>-weighted MRI images of Gd:Mn-Dox nanospheres (B) at concentrations noted on the figures. The bar graph (C) shows the MRI signal intensity produced by the Gd:Mn-Dox nanospheres in different acidic environments (HCl solution control or pH 4.5 buffer test solution). The pH 4.5 buffer was used to mimic the lysosome environment.

## Conclusions

In conclusion, this chapter described the *in vitro* characterization of multiple bio-activities and features of the synthesized gadolinium-based nanocomplexes. Physicochemical features of the synthesized gadolinium-based nanocomplexes were characterized, including demonstrating that the gadolinium-based nanocomplexes did not have a crystalline structure – they were amorphous; that the gadolinium was evenly dispersed in the nanocomplexes, as determined by elemental analysis; and that they have good MRI traceability, as determined using *in vitro* MRI tests. Understanding of the synthesis process of Gd:Mn-Dox nanocomplexes was improved by using UV-Vis spectroscopy to examine the UV-Vis absorbance of various components of the reaction individually or mixed, as well as the final product.

External irradiation-activated mPGA disintegration was observed and mPGA candidate NO. 132 was selected for subsequent studies. The external irradiation-activated low-pH-responsive *in vitro* doxorubicin release from mPGA (NO. 128A, NO. 132) coated Gd:Mn-Dox nanocomplexes was observed in a lysosomal pH environment (pH 4.5). The doxorubicin encapsulation was determined to be stable, since a significant doxorubicin release was only observed with clinically relevant doses of irradiation. It is anticipated that the use of other hydrophobic chemical groups as modifiers of PGA may also be successful in preventing premature drug release and in responding in an irradiation-sensitive manner.

The *in vitro* cellular uptake of the nanocomplexes by human breast cancer cells was confirmed by means of TEM, confocal microscopy and ICP-MS.

MTT assay results showed that the mPGA and non-Dox loaded nanocomplexes were biocompatible. A synergistic anticancer effect of the gadolinium plus doxorubicin incorporated in the nanocomplexes was also demonstrated in MTT and clonogenic assays.

The *in vitro* MRI traceability of doxorubicin loaded and non-loaded nanocomplexes was confirmed using clinical MRI and PET-MRI. The *in vitro* low-pH-responsive gadolinium release from Gd:Mn-Dox nanospheres was also confirmed using this method. Overall, irradiation-sensitive polymer coatings combined with inorganic multifunctional low-pH-responsive nanospheres have exciting clinical implications, as they represent a possible approach to delivering chemotherapeutic agents, imaging contrast agents, and radiosensitizing agents together in a safer and more controlled manner.

## Chapter 5 – *In Vivo* Animal Studies Using a Rat Model

### Introduction

Most human breast cancer xenograft models in animals were developed in mice, and have been frequently used to study the efficacy of newly invented treatments<sup>215,216</sup>. However, in this chapter, a rat model was more ideal due to enhanced spatial resolution of MRI as compared with a mouse model.

Published works about gadolinium-based nanocomplexes have generally reported that gadolinium-based nanocomplexes are biocompatible and well tolerated in animal models or human patients, with no obvious acute or long term toxicities demonstrated in animal models<sup>67,168,217,218</sup>.

The three main components of the nanocomplexes being tested in this chapter were: Doxorubicin, gadolinium, and poly-L-glutamic acid. Poly(L-glutamic acid) is a well-studied polymer that possesses valuable properties for this application, including biocompatibility, biodegradability, and water solubility<sup>194–196</sup>. Poly(L-glutamic acid) has already been approved for use as a drug carrier to form the water-soluble poly(L-glutamic acid)-paclitaxel drug conjugates known as Opaxio®.

Doxorubicin (Dox) is a type of anthracycline drug that is commonly used in cancer chemotherapy, and remains an important first line chemotherapeutic agent against certain types of tumours clinically<sup>219,220</sup>. When doxorubicin is administered alone, it causes cumulative dose-dependent cardiotoxicity, and can induce cardiomyocyte death, therefore resulting in left ventricular dysfunction and irreversible heart failure<sup>220</sup>. Since doxorubicin has poor organ selectivity, doxorubicin nano-formulations or delivery systems were developed, and approved, for the purpose reducing its cardiotoxicity by reducing the accumulation of doxorubicin in the

heart, while maintaining its intended bioactivity<sup>221</sup>. Thus, in terms of doxorubicin's cardiotoxicity, the nano-formulations were developed to have better biocompatibility than free doxorubicin when used at same dosage. Also, because of the side effects typically seen with free doxorubicin, assessment for cardiac tissue damage should always be included in the toxicity assessment of doxorubicin-carrying nanocomplexes.

Gadolinium-based medical MRI contrast agents were first approved in the 1980s and are currently used at a rate of more than 30 million injections annually, which means that they are currently used in about 40% of the MRI investigations performed globally<sup>74,218</sup>. Clinically, gadolinium chelate solutions (such as Gadavist<sup>®</sup>) are the most commonly used paramagnetic medical imaging contrast agents for MRI<sup>49,76</sup>. The most widely used intravenous MRI contrast agents are composed of gadolinium (III) chelates, which are also called T<sub>1</sub> or positive contrast agents<sup>45,59</sup>. Ionic gadolinium is also used in a chelated form to ensure its safe use while maintaining its paramagnetic properties, as there is a risk of a rare nephrogenic systematic fibrosis developing when using free gadolinium ions in patients with severe kidney failure. The possible toxicities associated with gadolinium and chelating agents are effectively contained through the complexation<sup>77</sup>. These gadolinium chelates for MRI, due to their small size and the fact that they are molecular solutions, have relatively short blood circulation half-lives for data acquisition and for non-specific biodistribution in tissues<sup>64,65</sup>. Rapid excretion from the body and lack of specificity have limited the use of gadolinium chelated MRI contrast agents to make further advances in detection and therapy management in oncology<sup>66</sup>.

*In vivo* reports on gadolinium-based nanocomplexes that have similar matrices to the nanocomplexes described in this work showed that gadolinium-based nanocomplexes effectively enhanced MRI of liver tumours, gliosarcoma, and brain metastases in animals or human patients

with good biocompatibility, which confirmed their potential application for imaging-guided-therapy and MR-LINAC<sup>67,217,222</sup>. The gadolinium oxide nanoparticles with the brand name of AGuIX<sup>®</sup> were shown not to accumulate in the liver, spleen, or lungs, and mostly accumulated in the kidneys and urine, and thus were eliminated from the animal model through a renal pathway<sup>84</sup>. Rod-shaped gadolinium hydroxide nanocomplexes were reported to predominantly accumulate in the spleen, followed by the liver, of tested animals<sup>168</sup>.

Looking at the broader scope of cancer nanomedicine, the majority of reports on biocompatibility of nanomedicines have indicated that the nanomedicines were captured by the liver and spleen after injection, which would be anticipated since the liver and spleen are major organs to eliminate foreign materials from the blood. Based on 117 published papers, the median intratumoural accumulation of the reported nanomedicines is only 0.7% of the total injected dose, independent of whether the nanomedicines were designed for passive or active targeting strategies<sup>223</sup>. It is proposed here that making less complex but more sophisticated nanomedicines with smart strategies to improve nanomedicine delivery efficiency based on mechanisms that are applicable to a variety of agents would be an important direction for work in this field.

In this chapter, a human breast cancer xenograft tumor model was established in immunodeficient rats. The drug accumulation in organs, acute toxicity, maximum tolerated dose and MRI enhancement effectiveness of the nanocomplexes were studied in the same species of rat.

## Materials and Methods

### *Materials*

Immunodeficient outbred female RNU rats (CrI:NIH-Foxn1<sup>mu</sup>) were purchased from Charles River Laboratories. Saline (0.9% NaCl, sterile sodium chloride) injections were purchased from Baxter. MCF-7 cells, HCl, formaldehyde and Gadavist® were sourced as described in previous chapters. mPGA NO. 132 was used as the coating material in this chapter and is referred to as mPGA throughout.

### *Xenograft Human Breast Cancer Tumour-Bearing Rat Model*

Immunodeficient outbred female RNU rats (CrI:NIH-Foxn1<sup>mu</sup>, 4 weeks of age) purchased from Charles River Laboratories (USA) were used to establish xenograft human breast cancer tumour models to be used in the studies in this chapter. The *in vivo* human breast cancer model described by<sup>224</sup> Direcks *et al* was adapted in this study. Six rats were used. Each rat was injected in the flank subcutaneously with 10<sup>7</sup> MCF-7 human breast cancer cells (cultured as described in Chapter 4). The animals were maintained in a sterile living environment with a standardized light/dark cycle. Sufficient water and food were supplied at all time (*ad libitum*). Tumour sizes, clinical signs, and body weights were monitored 2-3 times a week as the xenografted tumour growth progressed. The measurements were performed by the same person throughout the study for consistency. Tumour size calculation followed the formula: *Tumour volume = (length \* width \* height)/2*. This is the equivalent of treating the tumors as spheroids. Subsequent treatment was carried out once a tumour volume of 750 mm<sup>3</sup> was achieved.

### *In Vivo Biodistribution Study of mPGA@Gd:Mn-Dox Nanospheres Using mPGA NO. 132*

Five female rats (including the rats from the study on developing the xenograft human breast cancer tumour-bearing rat model above) were dosed with an mPGA@Gd:Mn-Dox nanosphere dispersion via tail vein (8 mg/kg), and euthanized at 2 hours, 4 hours, 8 hours, 48 hours, or 72 hours post-injection. Major organs (blood, heart, lungs, liver, spleen, kidneys, tumour and brain) were then harvested and prepared by dissolution in 37% HCl (Fisher Chemical, in ddH<sub>2</sub>O) for gadolinium content analysis using inductively coupled plasma mass spectroscopy (ICP-MS, Thermo Scientific ICAP-Q quadrupole ICPMS, in the University of Alberta Department of Earth and Atmospheric Sciences). Two of the rats from the study on developing the tumour model were used for a pilot study examining the biodistribution profile of non-coated Gd:Mn-Dox nanospheres at 2 hours and 8 hours post-injection, following the same procedure.

### *In Vivo Toxicity Testing of Gd:Mn, Gd:Mn-Dox and mPGA@Gd:Mn-Dox Nanospheres*

The *in vivo* acute toxicity study<sup>225</sup> using the “up-and-down” method was based on the Organisation for Economic Co-operation and Development (OECD) Guideline (#425, Oct. 2008) and four other reported works<sup>168,226–228</sup>. Female RNU rats purchased from Charles River Laboratories were used for this acute toxicity/maximum tolerated dose study. The healthy experimental animals were maintained in a sterile living environment with a standardized light/dark cycle. Sufficient water and food were supplied at all time (*ad libitum*). The animals were anesthetized using isoflurane (3%) mixed in oxygen and then nanodispersions were administered intravenously (i.v.) via the tail vein while the experimental animals remained anesthetized. One rat was used per dose, and each successive animal was dosed at a higher dose

based on the outcome of the previously treated animal. The first animal was treated with Gd:Mn-Dox at a starting dose of 24 mg/kg. Then the dose was escalated for each successive animal once the first or previous treated animal had survived for 24 hours and appeared to be in normal physical condition: The first rat was dosed at 24 mg/kg, and then the second and third rats were dosed at 72 mg/kg and 240 mg/kg, respectively. The highest dose used was 240 mg/kg. The highest dose tested for Gd:Mn-Dox was then used for rats tested with Gd:Mn and mPGA@Gd:Mn-Dox nanospheres - one rat was used per material, and was tested at the same weight of gadolinium as that used in the highest dose of the initial testing. Following treatment, experimental animals were closely monitored for 42 days with the aim of observing any delayed-onset symptoms of toxicity, as well as of allowing sufficient time for assessment of the severity of any physical signs of toxicity. Both acute and chronic signs of toxicity were assessed based on the rats' physical condition scores and body weight. A gross score exceeding 7, as per the scoring system (Table 5-1), was considered toxic. After the 42-day monitoring period, the animals were euthanized using carbon dioxide. Major organs of interest (the lungs, heart, spleen, liver, and kidneys) were harvested and fixed in 4% neutral buffered formaldehyde. These tissues were then trimmed, placed into cassettes embedded in paraffin, processed into paraffin blocks, and stained with hematoxylin and eosin (H&E) following standard methods for histological preparation. The tissue slides were observed under an optical microscope and a histopathological examination was performed by a board-certified veterinary pathologist who was blinded as to the treatment received by each experimental animal.

**Table 5-1.** Experimental animal body sign scoring sheet.

Indicators	Scoring of Independent Variables
<b>General Health</b>	An assessment with a score of 3 in any one category below will be immediately euthanized.
<b>Eating</b>	<ol style="list-style-type: none"> <li>0. Drinking and eating well.</li> <li>1. Change in eating or drinking habits.</li> <li>2. Inappetence.</li> <li>3. Not eating/drinking, severely dehydrated, malocclusion.</li> </ol>
<b>Behavior</b>	<ol style="list-style-type: none"> <li>0. Normal.</li> <li>1. Minor: Limping.</li> <li>2. Abnormal: Aggressive or huddled in a corner, reduced mobility, restlessness.</li> <li>3. Unsolicited vocalization, severe distress, immobile, self-trauma.</li> </ol>
<b>Tumour Size and Other</b>	0. Normal.
<b>Tumour-Related</b>	1. Palpable (< 750 cm <sup>3</sup> ).
<b>Indications</b>	<ol style="list-style-type: none"> <li>2. Visible (&gt; 750 to &lt; 2000 cm<sup>3</sup>).</li> <li>3. Large (≥ 2000 cm<sup>3</sup>), or visible signs of ulceration, necrosis, or infections of tumours.</li> </ol>
<b>Respiration</b>	0. Normal.

---

	<ol style="list-style-type: none"> <li>1. Laboured breathing (clicking noises).</li> <li>2. Respiratory distress.</li> <li>3. Severe respiratory distress.</li> </ol>
<b>Appearance</b>	<ol style="list-style-type: none"> <li>0. Normal.</li> <li>1. Ruffled fur, evident of lack of grooming.</li> <li>2. Rough hair coat, animal appears depressed, reluctant to move, discharge from eyes and nose.</li> <li>3. Very rough hair coat, animal appears severely depressed, prolonged abnormal posture.</li> </ol>
<b>Weight Loss Compared to Initial Body Weight</b>	<ol style="list-style-type: none"> <li>0. Normal.</li> <li>1. 5 – 10%.</li> <li>2. 15 – 20%.</li> <li>3. &gt; 20%.</li> </ol>
<b>Other Immediate Indications for Euthanasia</b>	<p>Discoloration/blood in urine or feces; paralysis; unconsciousness; inability reach food or water for more than 24 hours; inability to urinate or defecate.</p> <p>The detection limits of cTnI (Cardiac Troponin I) varies with different companies. Hence, fold increases in cTnI values compared to the baselines were used for evaluation, rather than specific concentrations in blood. Rats with a 2-fold increased cTnI value compared to baseline (Day 0) will be monitored closely. Rats demonstrating a 4-fold level</p>

---

increase of cTnI compared to baseline will be immediately euthanized.

### **Total Score\***

---

#### **\*For an assessment based on total score:**

0 = normal, no action necessary; 1 – 6 = moderate changes; 7 – 12 = significant changes, monitor closely; > 12 = immediately euthanize.

#### *In Vivo MR Imaging*

*In vivo*  $T_1$  &  $T_2$  weighted MR imaging of experimental animals (described below) was carried out in a SIEMENS Medical System 3.0 T (Tesla) PET-MR imaging facility. Rats were anesthetized with 3% isoflurane in oxygen and kept under general anesthesia using isoflurane (3%) mixed in oxygen during the imaging process. One rat was used for testing each material. Gd:Mn-Dox and mPGA@Gd:Mn-Dox nanospheres, as well as Gadavist®, were dispersed in 0.9% saline onsite. The injection dose for each rat was 0.1 mmol Gd/kg. Saline and Gadavist® control groups were injected with saline (1 mL) and Gadavist® (0.1 mmol Gd/kg), respectively.  $T_1$  &  $T_2$  weighted MRI measurements were made before and up to 0.5 hours after intravenous injections were made. Saline, Gadavist® and Gd:Mn-Dox nanosphere-treated rats were subject to  $T_1$  enhancement assessment. The mPGA@ Gd:Mn-Dox nanosphere-treated rat was subject to  $T_2$  enhancement assessment.

## Results & Discussion

### *Xenograft Human Breast Cancer Tumour-Bearing Rat Model*

Although initial *in vivo* studies of anti-cancer nanomedicines have been mostly carried out in mice<sup>215,216</sup>, the selected rat model was chosen in the present study with the aim of enhancing spatial resolution when using an MRI scanner relative to the smaller mouse model. In the present study, four rats out of the six successfully developed a tumour in the flank. The tumour engraftment rate was thus determined to be 66%, which was consistent with the 68% tumour engraftment rate previously determined in the reference<sup>224</sup>. In this study, the tumour doubling time was 6 days (Table 5-2), which was aligned to the 6-day doubling time in the reference<sup>224</sup>. In order not to waste experimental animals, the six rats were used for the biodistribution study below.

**Table 5-2.** The established tumour model growth rate.

Measurement	Tumour Volume (mm <sup>3</sup> )		
	# 1	# 2	# 3
<i>1<sup>st</sup></i>	264	152	81
<i>7 Days Later</i>	896	435	180
<i>14 Days Later</i>	1465	938	296*
<i>Doubling Time (days)</i>	6	5	6

\*This measurement was performed 12 days later.

### *In Vivo Biodistribution of mPGA@Gd:Mn-Dox Nanospheres*

As demonstrated in Figure 5-1, the gadolinium content in the selected organs was calculated against the organ weight as a percentage of the injected dose per gram. The detected gadolinium content in the blood was fairly low at all the tested time points, indicating that the injected nanospheres were cleared from the blood circulation within 2 hours after being administered through the tail vein. The early high levels of gadolinium in the lungs, liver, and spleen indicated that the injected nanospheres predominantly accumulated in these organs at the 2-hour timepoint. At 4 hours, a much larger uptake by the liver relative to the rest of the analyzed organs was observed, which is possibly partially due to the fact that the liver, being the largest organ and having the largest blood volume inside the organ, might have a resultant higher uptake of the nanospheres per unit weight. It should also be noted that the lungs, liver, and spleen are major organs in the reticuloendothelial system, which is related to the clearance of nanoparticles from the blood by mononuclear phagocytes. The uptake by the lungs slowed down between 2 and 4 hours, while the uptake by the spleen increased between 2 and 4 hours after treatment. Overall, nanosphere uptake happened mainly in the liver, followed by the spleen and lungs, whereas the gadolinium content detected in the blood, heart, kidneys, tumour and brain was very low. Interestingly, as described in Chapter 2, a similar pattern was reported in the *in vivo* biodistribution study of gadolinium nanorods, except that the spleen accumulated a much larger quantity of the test material relative to the other organs that were analyzed<sup>83,168</sup>. The nanospheres tested in this chapter are mainly different from the reported nanorods in terms of the morphology and the layer of mPGA coating. It could be deduced that the spherical shape and mPGA coating resulted in the observed change in the *in vivo* biodistribution profile of these nanoparticles.

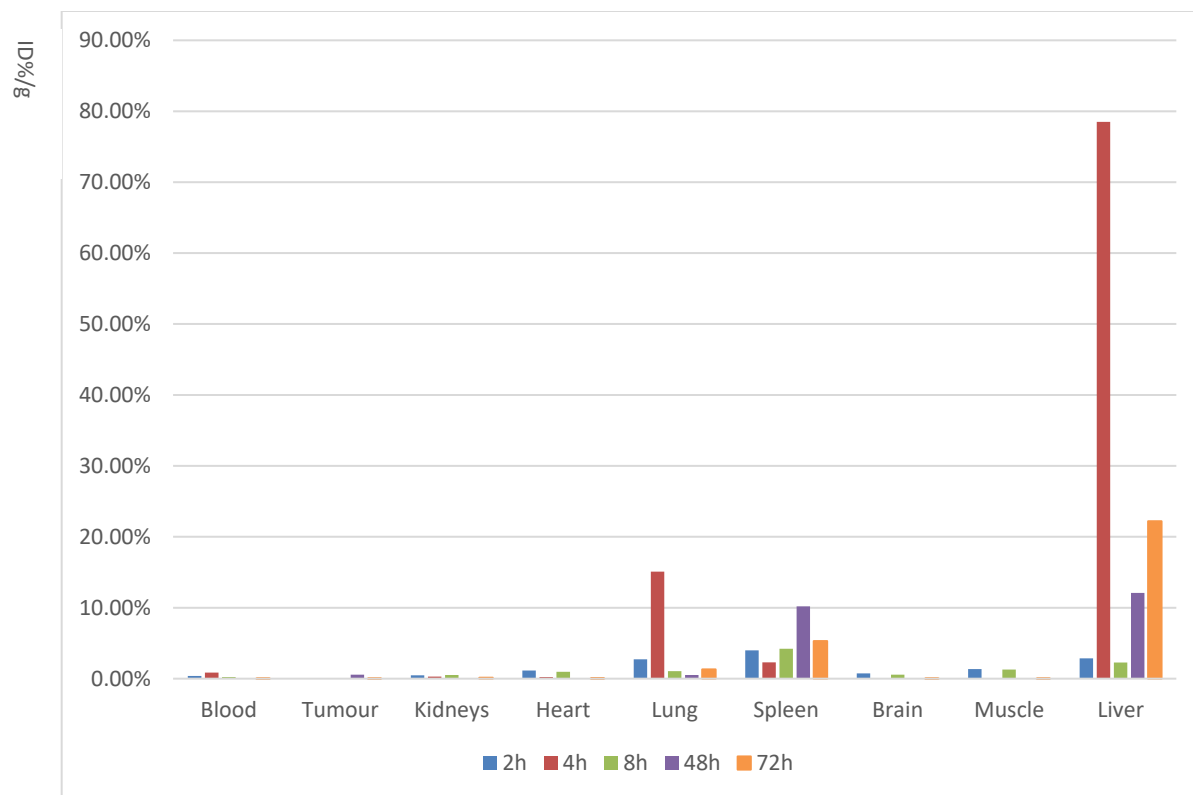


**Figure 5-1.** *In vivo* biodistribution of mPGA@Gd:Mn-Dox nanospheres in major organs of female rats with xenografted human breast cancer tumours.

The results of the *in vivo* biodistribution pilot study for the uncoated spherical Gd:Mn-Dox nanospheres are shown in Figure 5-2. The uncoated nanospheres' uptake by the spleen surpassed the uptake in other tested organs, which is more aligned with the *in vivo* biodistribution pattern of the nanorods in Chapter 2 than with what was observed in this chapter when testing the coated nanospheres. This suggests that the mPGA coating altered the *in vivo* biodistribution profile of Gd:Mn-Dox nanospheres in the female RNU rats.

The goal of this assay was to assess how the selected mPGA coating helps alter the biodistribution pattern of Gd:Mn-Dox nanospheres in experimental animals. Since the mPGA@Gd:Mn-Dox nanospheres were mainly captured by the liver, spleen, and lungs before

they were gradually excreted out of the body, it is important to use histological examination of all the organ tissues to determine whether the mPGA@Gd:Mn-Dox nanospheres could cause any tissue damage, lesions, or inflammation due to toxic exposure, especially in the liver, spleen and lungs, where the highest accumulation was observed.

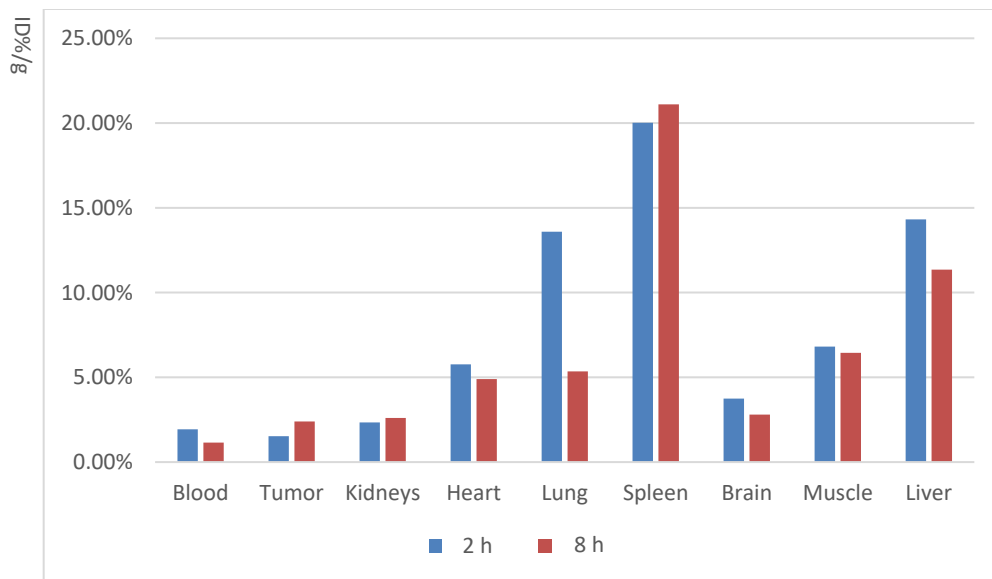


**Figure 5-2.** *In vivo* biodistribution of Gd:Mn-Dox nanospheres, 2 and 8 hours after injection, in major organs of female rats with xenografted human breast cancer tumours.

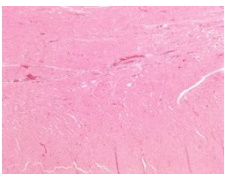
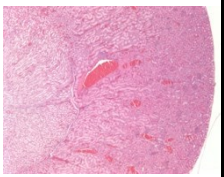
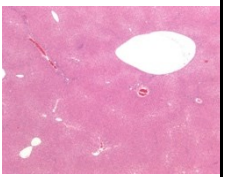
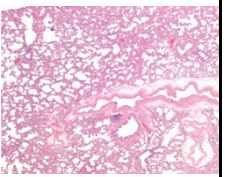
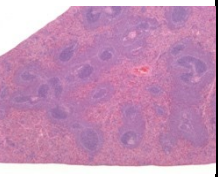
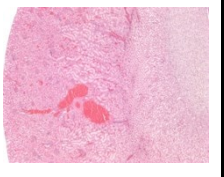
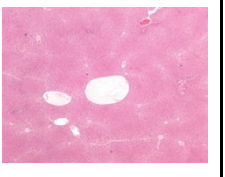
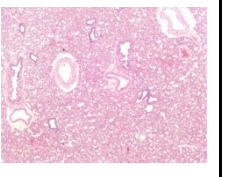
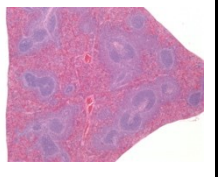
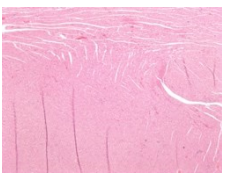
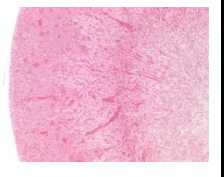
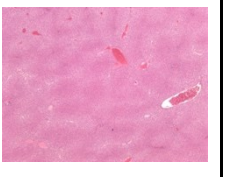
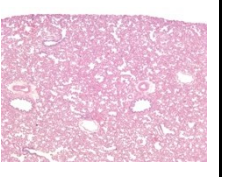
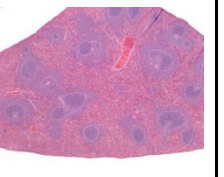
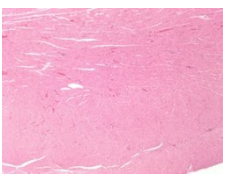
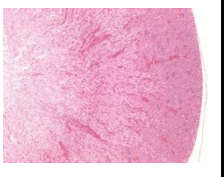
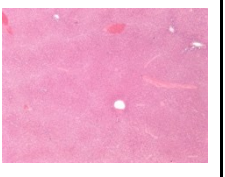
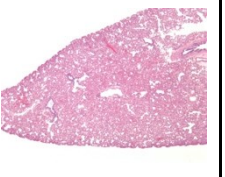
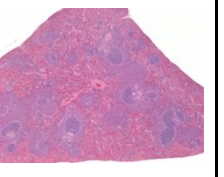
#### *In Vivo Toxicity Testing of Gd:Mn, Gd:Mn-Dox and mPGA@Gd:Mn-Dox Nanospheres*

It was anticipated that if there were any abnormal effects observed at a particular dosage, the Gd:Mn and the mPGA@Gd:Mn-Dox formulas should be less toxic than the Gd:Mn-Dox nanospheres, because the Gd:Mn nanoparticles do not contain Dox, and the mPGA coating on the surface of the mPGA@Gd:Mn-Dox should help prevent premature release of doxorubicin. Thus the highest dose tested for the Gd:Mn-Dox nanospheres was the only dose used for the testing of the Gd:Mn and mPGA@Gd:Mn-Dox nanospheres. By eliminating the low dose studies

using Gd:Mn and mPGA@Gd:Mn-Dox, the number of experimental animals required was reduced. Throughout the study, no abnormal behaviors or physical signs were observed. No animals died or appeared moribund at any studied dose level.

In terms of histological study of the tissues, with one exception (as described below), all tissue samples from the treated rats were found to be microscopically normal. As shown in Figure 5-3, no differences were observed relative to the healthy (saline) control at all doses tested. The saline treated control animal had microscopic evidence of mild chronic inflammation of the bronchi. Given that only the one healthy animal was affected, this inflammation was not related to the test articles. The mPGA@Gd:Mn-Dox nanospheres-treated group had mild chronic bronchitis characterized by mild bronchial epithelial hyperplasia and peribronchial lymphocyte infiltration. It is not possible to say with certainty whether this was test article related or not. The histological images are more suggestive of exposure to inhaled antigens and therefore the bronchitis might not be related to the test article. The healthy control rat had slightly more BALT (bronchus-associated lymphoid tissue) development than is common for cage-housed laboratory rats, but this was still within the normal range. This was only found in one airway in the section examined and a recut of the lung tissue within a few microns of the affected airway revealed completely normal lung. Therefore, this was concluded to be an incidental finding of no pathologic importance. No degeneration, necrosis, congestion, or pulmonary fibrosis was found in any of the experimental groups. If there were any side effects that occurred in the middle of the study without showing any abnormal physical signs, the histology demonstrates that the rats could recover within the test period. As well, any side effects that may have been present, but gone undetected, caused no abnormal impacts on animals' daily lives. All the results indicated a relatively low toxicity of Gd:Mn, Gd:Mn-Dox and

mPGA@Gd:Mn-Dox nanospheres in female RNU rats at a post-exposure time of 42 days. These results suggest that the synthesized gadolinium based nanospheres were tolerated *in vivo* at a dosage of up to 240 mg/kg. The MTD (maximum tolerated dose) of all the treatment arms for female RNU rats was likely no less than 240 mg/kg.

	HEART	KIDNEY	LIVER	LUNG	SPLEEN
Control (Saline)					
Gd:Mn-Dox					
Gd:Mn-Dox					
Gd:Mn-Dox					

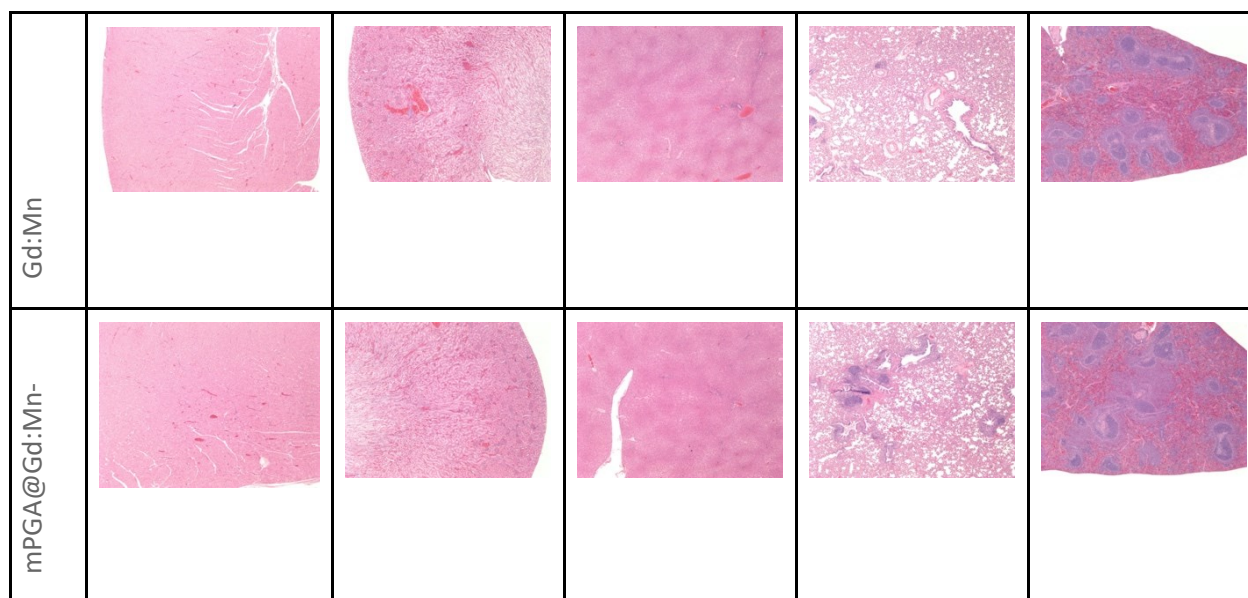
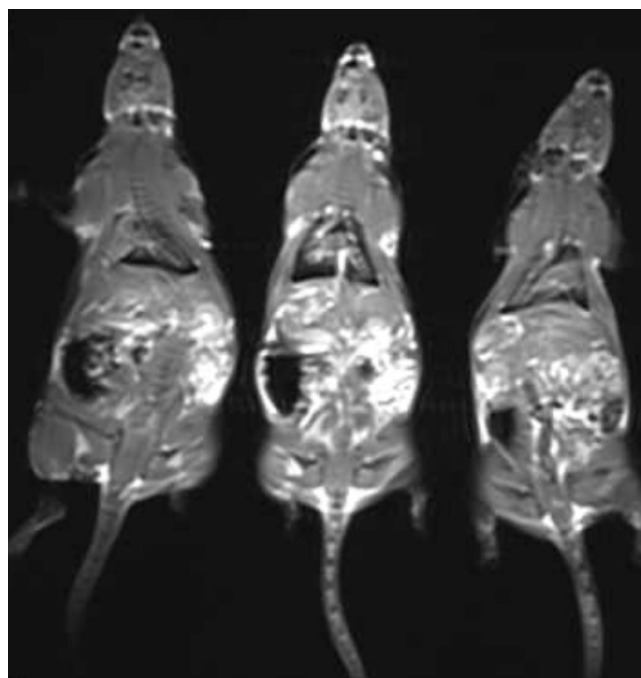


**Figure 5-3.** Examples of micrographs used for histological examination of various H&E stained tissues from female RNU rats treated with saline; Gd:Mn-Dox nanospheres at 24, 72, and 240 mg/kg; Gd:Mn nanospheres at 240 mg/kg; or mPGA@Gd:Mn-Dox nanospheres at 240 mg/kg; all 42 days after treatment.

### *In Vivo MR Imaging*

Gadolinium has the ability to alter both  $T_1$  and  $T_2$  relaxation rates in the MRI process. Both the  $T_1$  and  $T_2$  MRI signal enhancement effects of the gadolinium-based nanospheres were assessed. The  $T_1$  and  $T_2$  weighted MR images are shown in Figures 5-4 and 5-5, respectively. This *in vivo* test was only carried out in healthy rats. This was because the *in vivo* biodistribution data did not show preferred accumulation in the established tumour model, and therefore the tumour would not generate a strong enough signal for analysis at the imaging facility used. Instead, the MRI enhancing effect was evaluated in the liver, which had demonstrated the highest uptake of nanospheres relative to the other organs examined. In Figure 5-4, the Gadavist®-

treated rat (positive control) and saline-treated rat (negative control) showed the highest and the lowest image contrast of rat body and organs, respectively, whereas the Gd:Mn-Dox nanosphere-treated group fell in between. Gd:Mn-Dox nanospheres demonstrated a  $T_1$  enhancement of the rat body that was stronger than saline but weaker than Gadavist®. This indicates that the Gadavist® group had the highest level of effective gadolinium molecules, the Gd:Mn-Dox group had fewer, and the saline group had none. This is possibly because the gadolinium element in Gadavist® is in solution and thus every gadolinium molecule had the opportunity to interact with and further alter the  $T_1$  relaxation rate of surrounding water molecules, while a lower quantity of gadolinium molecules were able to take effect in the Gd:Mn-Dox nanosphere-treated rat. The gadolinium molecules inside the solid core of the Gd:Mn-Dox nanospheres likely did not have a chance to interact with water molecules. Figure 5-5 shows the  $T_2$  weighted images of the rat before (left) and after (right) being injected with mPGA@Gd:Mn-Dox nanospheres. The image on the right, taken after the injection, has stronger image contrast than the one on the left, taken before the injection was performed, which can be observed by comparing the liver in the two images. Both the  $T_1$  and  $T_2$  weighted MRI results indicated that the proposed gadolinium-based nanospheres exhibited the ability to provide contrast enhancement in MRI processes.

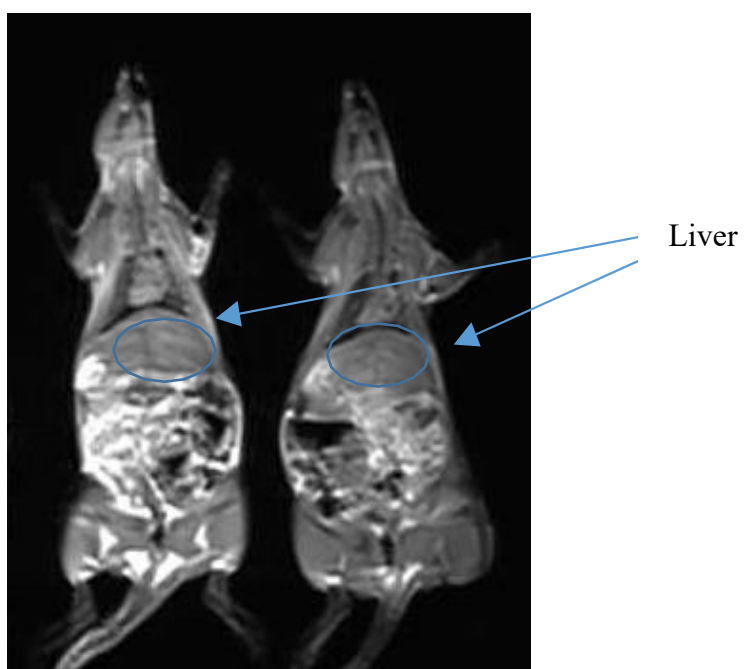


Saline

Gadavist®

Gd:Mn-Dox

**Figure 5-4.** *In vivo*  $T_1$  weighted MR images of saline, Gadavist® and Gd:Mn-Dox nanosphere-treated rats.



Liver

**Figure 5-5.** *In vivo*  $T_2$  weighted MR images of the rat before (left) and after (right) being injected with mPGA@Gd:Mn-Dox nanospheres.

## Conclusions

This chapter describes the *in vivo* characterization of the multifunctional properties of gadolinium-based nanocomplexes developed in Chapter 3. The *in vivo* biodistribution profile, acute toxicity, and MRI contrast enhancement effects of the proposed theranostic nanocomplexes were explored in an immunodeficient rat model. The rats tolerated the injected doses well. The biodistribution of the injected nanocomplexes was mainly in the liver, lungs, and spleen. This is different from the biodistribution of the rod shape nanocomplexes described in Chapter 2, where the spleen accumulated a much larger quantity of the test material relative to the other organs that were analyzed. Based on the current *in vivo* results, the nanocomplexes were tolerated in rats within tested dose range (< 240 mg/kg), with no histological changes observed in tested organs.

## Chapter 6 – Conclusions

### Conclusions

In this thesis, firstly,  $\text{Gd}(\text{OH})_3$  nanorods,  $\text{Gd}(\text{OH})_3\text{:Mn}$  nanorods, and  $\text{Gd}(\text{OH})_3\text{:Mn-Dox}$  nanocomplexes were successfully synthesized using a single-step wet chemical method. The potential to use  $\text{Gd}(\text{OH})_3\text{:Mn-Dox}$  nanocomplexes as a multifunctional nanoplatform was explored. Confocal microscopy was used to confirm the occurrence of, and visualise, the cellular uptake and payload release of  $\text{Gd}(\text{OH})_3\text{:Mn-Dox}$  nanocomplexes in a human breast cancer cell line. The therapeutic efficacy of  $\text{Gd}(\text{OH})_3\text{:Mn-Dox}$  nanocomplexes was assessed by flow cytometry and using a clonogenic assay in the absence and presence of x-ray irradiation. The Dox-mediated formation mechanism of  $\text{Gd}(\text{OH})_3\text{:Mn-Dox}$  nanocomplexes was examined. The results of this first set of studies suggested that  $\text{Gd}(\text{OH})_3\text{:Mn-Dox}$  nanocomplexes could be an efficient multipurpose nanoplatform for synergistic therapy delivery, with the added advantage of ease of fabrication.

Subsequently, amorphous Gd:Mn nanospheres were developed, using a simple hydrothermal homogeneous precipitation method. TEM analyses demonstrated that near-spherical shaped monodisperse particles were produced at varying sizes that could be tuned by changing the quantity of glycerol used in the reaction process. These spherical-shaped particles may have some distinct advantages over the nanorods developed above in terms of their flow dynamics and interactions with cells *in vivo*.

Furthermore, novel doxorubicin-loaded nanospheres (Gd:Mn-Dox nanospheres), as well as surface coated mPGA@Gd:Mn and mPGA@Gd:Mn-Dox nanocomplexes, were successfully synthesized, using simple hydrothermal homogeneous coprecipitation methods. The morphologies and sizes of these novel nanocomplexes were characterized via TEM and SEM.

Near-spherical shaped monodisperse nanoparticles were produced. The effects of adding doxorubicin and varying the ratio of glycerol:urea on the final products were explored. The synthesized nanospheres showed a decreased diameter after doxorubicin was added to the reaction system, while different ratios of glycerol:urea resulted in different morphologies and diameters of the final products.

The *in vitro* characterization of multiple features of the synthesized spherical gadolinium-based nanocomplexes was performed. Physicochemical features of the synthesized gadolinium-based nanocomplexes were characterized. This included demonstrating that the gadolinium-based nanocomplexes did not have a crystalline structure – they were amorphous; that the gadolinium was evenly dispersed in the nanocomplexes, as determined by elemental analysis; and that the nanocomplexes had good MRI traceability, as determined using *in vitro* MRI tests. Understanding of the synthesis process used to make the Gd:Mn-Dox nanocomplexes was improved by using UV-Vis spectroscopy to examine the UV-Vis absorbance of various components of the reaction both individually and mixed, as well as of the final product.

External irradiation-activated disintegration of mPGA candidates NO. 128A and NO. 132 was examined. The external irradiation-activated low-pH-responsive *in vitro* doxorubicin release from mPGA-coated Gd:Mn-Dox nanocomplexes was observed in a lysosomal pH environment (pH 4.5). The doxorubicin encapsulation was determined to be stable, since a significant doxorubicin release was only observed with clinically relevant doses of irradiation. It is anticipated that the use of other hydrophobic chemical groups as modifiers of PGA may also be successful in preventing premature drug release and in responding in an irradiation-sensitive manner. Based on the above testing, mPGA candidate NO. 132 was selected for subsequent studies.

The *in vitro* cellular uptake of these nanocomplexes by human breast cancer cells was confirmed by means of TEM, confocal microscopy, and ICP-MS.

MTT assay results showed that the mPGA and non-Dox loaded nanocomplexes were biocompatible. A synergistic anticancer effect of the gadolinium plus doxorubicin incorporated in the nanocomplexes was also demonstrated in MTT and clonogenic assays.

The *in vitro* MRI traceability of doxorubicin-loaded and unloaded nanocomplexes was confirmed using clinical MRI and PET-MRI. A low-pH-responsive gadolinium release from Gd:Mn-Dox nanospheres was also confirmed *in vitro* using this method. Overall, irradiation-sensitive polymer coatings combined with inorganic multifunctional low-pH-responsive nanospheres have exciting clinical implications, as they represent a possible approach to delivering chemotherapeutic agents, imaging contrast agents, and radiosensitizing agents together in a more controlled manner than what is currently available.

Lastly, *in vivo* characterization of the multifunctional properties of novel gadolinium-based nanocomplexes was performed. The *in vivo* biodistribution profile, acute toxicity, and MRI contrast enhancement effect of the proposed theranostic nanocomplexes were explored in an immunodeficient rat model. The rats tolerated the injected doses well, with the nanocomplexes mainly distributed in the liver, lungs, and spleen. This was different from the biodistribution of the rod shape nanocomplexes described above, where the spleen accumulated a much larger quantity of the test material relative to the other organs that were analyzed. Based on the current *in vivo* results, the spherical gadolinium-based nanocomplexes were tolerated in rats within tested dose range (< 240 mg/kg), with no histological changes observed in tested organs.

There are limitations to the work reported here. First, because of the lack of a gadolinium dielectric constant, the size distributions of final products were only measured through the use of

electronic microscopes (SEM and TEM). The second limitation concerns the understanding of the underlying basic reaction mechanisms of the fabrication process. On a related note, the actual ratio of the components in the final products has not been confirmed yet. Once the reaction mechanisms are thoroughly explored and well understood, it should be possible to significantly improve the loading capacity for doxorubicin and other suitable drugs. Lastly, the mPGA polymer that was selected for the final tests performed did not produce a desirable biodistribution profile, as most of the injected nanocomplexes ended up in the liver, spleen, and lungs. Thus, the dynamic relationship between the distribution profile in specific tissues and the various potential modifications to the PGA should be explored in future studies in order to select an mPGA that combines the strengths of the current mPGA with an improved biodistribution profile. To that end, the use of an animal MRI facility with a much higher magnetic field strength would be a significant asset.

Looking to the future, studies on scale-up of the fabrication process of this gadolinium-based nanoplatform, optimisation of the reactor design, and developing an understanding of the underlying basic reaction mechanisms and reaction kinetics of the fabrication process would be worthwhile. Studies on the basic properties of the gadolinium element, such as its dielectric constant, could help fill the knowledge gap in that area. Improving the understanding of gadolinium and doxorubicin release kinetics is also important and it would be worthwhile to explore the correlation between MRI signal changes as gadolinium dissociates and both doxorubicin release and topical radiosensitization profiles. To that end, a high magnetic field MRI facility would be needed for quantification of MRI signal changes.

In this thesis, the rod-like gadolinium-based crystalline nanocomplexes described in Chapter 2 were upgraded to a new spherical amorphous version with increased doxorubicin

loading capacity, and a radiation-activable surface coating, while maintaining their MRI-radiosensitization property. This new nanoplatform can be generated via a very simple and environmentally-friendly fabrication process. The smart strategy of using a “smart” radiation-activable nanoplatform for delivering gadolinium and doxorubicin for theranostic MRI-radiosensitization and doxorubicin chemotherapy was demonstrated. This proposed nanoplatform represents an increasing trend in cancer nanotheranostics towards the research and development of novel and much more effective drug delivery platforms which pave the way for individualised cancer medicine, particularly for cancer patients deemed ineligible for chemotherapy due to significant medical co-morbidities. Furthermore, successful incorporation of this proposed platform into current clinical practice can be facilitated by the MR-LINAC and external radiation departments, with the hope of improving the survival outcomes of those suffering with cancer.

## Bibliography

1. Freitas RA. Exploratory design in medical nanotechnology: A mechanical artificial red cell. *Artif Cells Blood Substit Immobil Biotechnol.* 1998;26(4):411-430.  
doi:10.3109/10731199809117682
2. Ferrari M. Cancer nanotechnology: Opportunities and challenges. *Nat Rev Cancer.* 2005;5(3):161-171. doi:10.1038/nrc1566
3. Nie S, Xing Y, Kim GJ, Simons JW. Nanotechnology applications in cancer. *Annu Rev Biomed Eng.* 2007;9:257-288. doi:10.1146/annurev.bioeng.9.060906.152025
4. Wang MD, Shin DM, Simons JW, Nie S. Nanotechnology for targeted cancer therapy. *Expert Rev Anticancer Ther.* 2007;7(6):833-837. doi:10.1586/14737140.7.6.833
5. Lasic DD, Papahadjopoulos D. Liposomes revisited. *Science (80- ).* 1995;267(5202):1275-1276. doi:10.1126/science.7871422
6. Barenholz Y. Doxil® - The first FDA-approved nano-drug: Lessons learned. *J Control Release.* 2012;160(2):117-134. doi:10.1016/j.jconrel.2012.03.020
7. Lasic DD. Doxorubicin in sterically stabilized liposomes. *Nature.* 1996;380(6574):561-562. doi:10.1038/380561a0
8. Fang J, Nakamura H, Maeda H. The EPR effect: Unique features of tumor blood vessels for drug delivery, factors involved, and limitations and augmentation of the effect. *Adv Drug Deliv Rev.* 2011;63(3):136-151. doi:10.1016/j.addr.2010.04.009
9. Rahman A, Harris M. Comparative pharmacokinetics of free doxorubicin and doxorubicin

- (DX) entrapped in cardiolipin liposomes. *Proc Am Assoc Cancer Res.* 1985;VOL. 26:2295-2299.
10. Speth PAJ, van Hoesel QGCM, Haanen C. Clinical Pharmacokinetics of Doxorubicin. *Clin Pharmacokinet.* 1988;15(1):15-31. doi:10.2165/00003088-198815010-00002
  11. Xu X, Ho W, Zhang X, Bertrand N, Farokhzad O. Cancer nanomedicine: From targeted delivery to combination therapy. *Trends Mol Med.* 2015;21(4):223-232. doi:10.1016/j.molmed.2015.01.001
  12. Farokhzad OC, Langer R. Impact of nanotechnology on drug delivery. *ACS Nano.* 2009;3(1):16-20. doi:10.1021/nn900002m
  13. Hoelder S, Clarke PA, Workman P. Discovery of small molecule cancer drugs: Successes, challenges and opportunities. *Mol Oncol.* 2012;6(2):155-176. doi:10.1016/j.molonc.2012.02.004
  14. Harris T. Gene and drug matrix for personalized cancer therapy. *Nat Rev Drug Discov.* 2010;9(8):660. doi:10.1038/nrd3181-c1
  15. Schilsky RL. Personalized medicine in oncology: The future is now. *Nat Rev Drug Discov.* 2010;9(5):363-366. doi:10.1038/nrd3181
  16. Cancer nanotechnology: small, but heading for the big time. *Nat Rev Drug Discov.* 2007;6(3):174-175. doi:10.1038/nrd2285
  17. Gradishar WJ. Albumin-bound paclitaxel: A next-generation taxane. *Expert Opin Pharmacother.* 2006;7(8):1041-1053. doi:10.1517/14656566.7.8.1041

18. D’Mello SR, Cruz CN, Chen ML, Kapoor M, Lee SL, Tyner KM. The evolving landscape of drug products containing nanomaterials in the United States. *Nat Nanotechnol.* 2017;12(6):523-529. doi:10.1038/nnano.2017.67
19. Jain KK. *The Handbook of Nanomedicine, Third Edition.* Springer New York; 2017. doi:10.1007/978-1-4939-6966-1
20. Kuncic Z, Lacombe S. Nanoparticle radio-enhancement: Principles, progress and application to cancer treatment. *Phys Med Biol.* 2018;63(2). doi:10.1088/1361-6560/aa99ce
21. van der Meel R, Sulheim E, Shi Y, Kiessling F, Mulder WJM, Lammers T. Smart cancer nanomedicine. *Nat Nanotechnol.* 2019;14(11):1007-1017. doi:10.1038/s41565-019-0567-y
22. Peer D, Karp JM, Hong S, Farokhzad OC, Margalit R, Langer R. Nanocarriers as an emerging platform for cancer therapy. *Nat Nanotechnol.* 2007;2(12):751-760. doi:10.1038/nnano.2007.387
23. Shi J, Kantoff PW, Wooster R, Farokhzad OC. Cancer nanomedicine: Progress, challenges and opportunities. *Nat Rev Cancer.* 2017;17(1):20-37. doi:10.1038/nrc.2016.108
24. Chen H, Zhang W, Zhu G, Xie J, Chen X. Rethinking cancer nanotheranostics. *Nat Rev Mater.* 2017;2(7):1-18. doi:10.1038/natrevmats.2017.24
25. Janib SM, Moses AS, MacKay JA. Imaging and drug delivery using theranostic

- nanoparticles. *Adv Drug Deliv Rev.* 2010;62(11):1052-1063.  
doi:10.1016/j.addr.2010.08.004
26. Kaida S, Cabral H, Kumagai M, et al. Visible drug delivery by supramolecular nanocarriers directing to single-platformed diagnosis and therapy of pancreatic tumor model. *Cancer Res.* 2010;70(18):7031-7041. doi:10.1158/0008-5472.CAN-10-0303
  27. Ponce AM, Viglianti BL, Yu D, et al. Magnetic resonance imaging of temperature-sensitive liposome release: Drug dose painting and antitumor effects. *J Natl Cancer Inst.* 2007;99(1):53-63. doi:10.1093/jnci/djk005
  28. Kaittanis C, Shaffer TM, Ogirala A, et al. Environment-responsive nanophores for therapy and treatment monitoring via molecular MRI quenching. *Nat Commun.* 2014;5.  
doi:10.1038/ncomms4384
  29. Yoo SS, Razzak R, Bédard E, et al. Layered gadolinium-based nanoparticle as a novel delivery platform for microRNA therapeutics. *Nanotechnology.* 2014;25(42):425102.  
doi:10.1088/0957-4484/25/42/425102
  30. Torchilin VP. Multifunctional, stimuli-sensitive nanoparticulate systems for drug delivery. *Nat Rev Drug Discov.* 2014;13(11):813-827. doi:10.1038/nrd4333
  31. Gasselhuber A, Dreher MR, Partanen A, et al. Targeted drug delivery by high intensity focused ultrasound mediated hyperthermia combined with temperature-sensitive liposomes: Computational modelling and preliminary in vivo validation. *Int J Hyperth.* 2012;28(4):337-348. doi:10.3109/02656736.2012.677930

32. Muhanna N, Cui L, Chan H, et al. Multimodal image-guided surgical and photodynamic interventions in head and neck cancer: From primary tumor to metastatic drainage. *Clin Cancer Res.* 2016;22(4):961-970. doi:10.1158/1078-0432.CCR-15-1235
33. Jin CS, Overchuk M, Cui L, et al. Nanoparticle-Enabled Selective Destruction of Prostate Tumor Using MRI-Guided Focal Photothermal Therapy. *Prostate.* 2016;76(13):1169-1181. doi:10.1002/pros.23203
34. Leibfarth S, Mönnich D, Welz S, et al. A strategy for multimodal deformable image registration to integrate PET/MR into radiotherapy treatment planning. *Acta Oncol (Madr).* 2013;52(7):1353-1359. doi:10.3109/0284186X.2013.813964
35. van der Heide UA, Houweling AC, Groenendaal G, Beets-Tan RGH, Lambin P. Functional MRI for radiotherapy dose painting. *Magn Reson Imaging.* 2012;30(9):1216-1223. doi:10.1016/j.mri.2012.04.010
36. Jaffray DA. Image-guided radiotherapy: From current concept to future perspectives. *Nat Rev Clin Oncol.* 2012;9(12):688-699. doi:10.1038/nrclinonc.2012.194
37. Hainfeld JF, Slatkin DN, Smilowitz HM. The use of gold nanoparticles to enhance radiotherapy in mice. *Phys Med Biol.* 2004;49(18):N309. doi:10.1088/0031-9155/49/18/N03
38. McMahon SJ, Hyland WB, Muir MF, et al. Biological consequences of nanoscale energy deposition near irradiated heavy atom nanoparticles. *Sci Rep.* 2011;1. doi:10.1038/srep00018

39. Butterworth KT, McMahon SJ, Currell FJ, Prise KM. Physical basis and biological mechanisms of gold nanoparticle radiosensitization. *Nanoscale*. 2012;4(16):4830-4838. doi:10.1039/c2nr31227a
40. Lux F, Sancey L, Bianchi A, Crémillieux Y, Roux S, Tillement O. Gadolinium-based nanoparticles for theranostic MRI-radiosensitization. *Nanomedicine*. 2015;10(11):1801-1815. doi:10.2217/nmm.15.30
41. Bonvalot S, Le Pechoux C, De Baere T, et al. First-in-human study testing a new radioenhancer using nanoparticles (NBTXR3) activated by radiation therapy in patients with locally advanced soft tissue sarcomas. *Clin Cancer Res*. 2017;23(4):908-917. doi:10.1158/1078-0432.CCR-16-1297
42. Bonvalot S, Rutkowski PL, Thariat J, et al. NBTXR3, a first-in-class radioenhancer hafnium oxide nanoparticle, plus radiotherapy versus radiotherapy alone in patients with locally advanced soft-tissue sarcoma (Act.In.Sarc): a multicentre, phase 2–3, randomised, controlled trial. *Lancet Oncol*. 2019;20(8):1148-1159. doi:10.1016/S1470-2045(19)30326-2
43. ClinicalTrials.gov: National Library of Medicine (US). NBTXR3 Crystalline Nanoparticles and Radiation Therapy in Treating Patients With Soft Tissue Sarcoma of the Extremity - Full Text View - ClinicalTrials.gov. <https://clinicaltrials.gov/ct2/show/NCT02379845>. Published 2015. Accessed November 23, 2020.
44. Miladi I, Alric C, Dufort S, et al. The in vivo radiosensitizing effect of gold nanoparticles

- based mri contrast agents. *Small*. 2014;10(6):1116-1124. doi:10.1002/sml.201302303
45. PA. R. Magnetic Resonance in Medicine. The Basic Textbook of the European Magnetic Resonance Forum. 8th edition. <https://www.magnetic-resonance.org/>. Published 2014. Accessed January 2, 2021.
  46. The American Cancer Society medical and editorial content team. MRI for Cancer. <https://www.cancer.org/treatment/understanding-your-diagnosis/tests/mri-for-cancer.html>. Published 2019.
  47. Lauffer RB. Paramagnetic Metal Complexes as Water Proton Relaxation Agents for NMR Imaging: Theory and Design. *Chem Rev*. 1987;87(5):901-927. doi:10.1021/cr00081a003
  48. Wahsner J, Gale EM, Rodríguez-Rodríguez A, Caravan P. Chemistry of MRI contrast agents: Current challenges and new frontiers. *Chem Rev*. 2019;119(2):957-1057. doi:10.1021/acs.chemrev.8b00363
  49. Xiao YD, Paudel R, Liu J, Ma C, Zhang ZS, Zhou SK. MRI contrast agents: Classification and application (Review). *Int J Mol Med*. 2016;38(5):1319-1326. doi:10.3892/ijmm.2016.2744
  50. Geraldes CFGC, Laurent S. Classification and basic properties of contrast agents for magnetic resonance imaging. *Contrast Media Mol Imaging*. 2009;4(1):1-23. doi:10.1002/cmml.265
  51. Gossuin Y, Gillis P, Hocq A, Vuong QL, Roch A. Magnetic resonance relaxation properties of superparamagnetic particles. *Wiley Interdiscip Rev Nanomedicine*

- Nanobiotechnology*. 2009;1(3):299-310. doi:10.1002/wnan.36
52. Tang KS, Hann B, Shapiro EM. On the use of micron-sized iron oxide particles (MPIOs) to label resting monocytes in bone marrow. *Mol Imaging Biol*. 2011;13(5):819-824. doi:10.1007/s11307-010-0437-3
  53. Ma X, Wang S, Hu L, et al. Imaging Characteristics of USPIO Nanoparticles (<5 nm) as MR Contrast Agent in Vitro and in the Liver of Rats. *Contrast Media Mol Imaging*. 2019;2019. doi:10.1155/2019/3687537
  54. Vogl TJ, Hammerstingl R, Schwarz W, et al. Superparamagnetic iron oxide-enhanced versus gadolinium-enhanced MR imaging for differential diagnosis of focal liver lesions. *Radiology*. 1996;198(3):881-887. doi:10.1148/radiology.198.3.8628887
  55. Kellar KE, Fujii DK, Gunther WHH, et al. NC 100150 injection, a preparation of optimized iron oxide nanoparticles for positive-contrast MR angiography. *J Magn Reson Imaging*. 2000;11(5):488-494. doi:10.1002/(SICI)1522-2586(200005)11:5<488::AID-JMRI4>3.0.CO;2-V
  56. Zhou Z, Wang L, Chi X, et al. Engineered iron-oxide-based nanoparticles as enhanced T 1 contrast agents for efficient tumor imaging. *ACS Nano*. 2013;7(4):3287-3296. doi:10.1021/nm305991e
  57. Bao Y, Sherwood JA, Sun Z. Magnetic iron oxide nanoparticles as: T 1 contrast agents for magnetic resonance imaging. *J Mater Chem C*. 2018;6(6):1280-1290. doi:10.1039/c7tc05854c

58. Wei H, Bruns OT, Kaul MG, et al. Exceedingly small iron oxide nanoparticles as positive MRI contrast agents. *Proc Natl Acad Sci U S A*. 2017;114(9):2325-2330.  
doi:10.1073/pnas.1620145114
59. Lim J, Turkbey B, Bernardo M, et al. Gadolinium MRI contrast agents based on triazine dendrimers: Relaxivity and in vivo pharmacokinetics. *Bioconjug Chem*. 2012;23(11):2291-2299. doi:10.1021/bc300461r
60. Hao D, Ai T, Goerner F, Hu X, Runge VM, Tweedle M. MRI contrast agents: Basic chemistry and safety. *J Magn Reson Imaging*. 2012;36(5):1060-1071.  
doi:10.1002/jmri.23725
61. Lux J, Chan M, Vander Elst L, et al. Metal chelating crosslinkers form nanogels with high chelation stability. *J Mater Chem B*. 2013;1(46):6359-6364. doi:10.1039/c3tb21104e
62. European Medicines Agency. In: *Definitions*. ; 2020. doi:10.32388/yokp53
63. Drugs@FDA: FDA-Approved Drugs.  
<https://www.accessdata.fda.gov/scripts/cder/daf/index.cfm?event=BasicSearch.process>.  
Published 2019. Accessed November 23, 2020.
64. Shokrollahi H. Contrast agents for MRI. *Mater Sci Eng C*. 2013;33(8):4485-4497.  
doi:10.1016/j.msec.2013.07.012
65. Alric C, Bazzi R, Lux F, et al. The design of hybrid nanoparticles for image-guided radiotherapy. *ACS Symp Ser*. 2012;1113:95-143. doi:10.1021/bk-2012-1113.ch007
66. Botta M, Tei L. Relaxivity enhancement in macromolecular and nanosized Gd III-based

- MRI contrast agents. *Eur J Inorg Chem.* 2012;2012(12):1945-1960.  
doi:10.1002/ejic.201101305
67. Lux F, Sancey L, Bianchi A, Crémillieux Y, Roux S, Tillement O. Gadolinium-based nanoparticles for theranostic MRI-radiosensitization. *Nanomedicine.* 2015;10(11):1801-1815. doi:10.2217/nmm.15.30
68. Baumann M, Krause M, Overgaard J, et al. Radiation oncology in the era of precision medicine. *Nat Rev Cancer.* 2016;16(4):234-249. doi:10.1038/nrc.2016.18
69. Baskar R, Lee KA, Yeo R, Yeoh KW. Cancer and radiation therapy: Current advances and future directions. *Int J Med Sci.* 2012;9(3):193-199. doi:10.7150/ijms.3635
70. Delaney G, Jacob S, Featherstone C, Barton M. The role of radiotherapy in cancer treatment: Estimating optimal utilization from a review of evidence-based clinical guidelines. *Cancer.* 2005;104(6):1129-1137. doi:10.1002/cncr.21324
71. Pignol JP, Rakovitch E, Beachey D, Le Sech C. Clinical significance of atomic inner shell ionization (ISI) and Auger cascade for radiosensitization using IUdR, BUdR, platinum salts, or gadolinium porphyrin compounds. *Int J Radiat Oncol Biol Phys.* 2003;55(4):1082-1091. doi:10.1016/S0360-3016(02)04508-X
72. Butterworth KT, McMahon SJ, Taggart LE, Prise KM. Radiosensitization by gold nanoparticles: Effective at megavoltage energies and potential role of oxidative stress. *Transl Cancer Res.* 2013;2(4):269-279. doi:10.3978/j.issn.2218-676X.2013.08.03
73. Kwatra D, Venugopal A, Anant S. Nanoparticles in radiation therapy: A summary of

- various approaches to enhance radiosensitization in cancer. *Transl Cancer Res.* 2013;2(4):330-342. doi:10.3978/j.issn.2218-676X.2013.08.06
74. Caravan P. Strategies for increasing the sensitivity of gadolinium based MRI contrast agents. *Chem Soc Rev.* 2006;35(6):512-523. doi:10.1039/b510982p
75. Lacerda S, Tóth É. Lanthanide Complexes in Molecular Magnetic Resonance Imaging and Theranostics. *ChemMedChem.* 2017;12(12):883-894. doi:10.1002/cmdc.201700210
76. Patil R, Galstyan A, Grodzinski ZB, et al. Single-and multi-arm gadolinium mri contrast agents for targeted imaging of glioblastoma. *Int J Nanomedicine.* 2020;15:3057-3070. doi:10.2147/IJN.S238265
77. Thunus L, Lejeune R. Overview of transition metal and lanthanide complexes as diagnostic tools. *Coord Chem Rev.* 1999;184(1):125-155. doi:10.1016/S0010-8545(98)00206-9
78. Zhang Y, Wei W, Das GK, Yang Tan TT. Engineering lanthanide-based materials for nanomedicine. *J Photochem Photobiol C Photochem Rev.* 2014;20(1):71-96. doi:10.1016/j.jphotochemrev.2014.06.001
79. Bünzli JCG. Lanthanide luminescence for biomedical analyses and imaging. *Chem Rev.* 2010;110(5):2729-2755. doi:10.1021/cr900362e
80. Mulder WJM, Strijkers GJ, Griffioen AW, et al. A liposomal system for contrast-enhanced magnetic resonance imaging of molecular targets. *Bioconjug Chem.* 2004;15(4):799-806. doi:10.1021/bc049949r

81. Tóth É, Bolskar RD, Borel A, et al. Water-soluble gadofullerenes: Toward high-relaxivity, pH-responsive MRI contrast agents. *J Am Chem Soc.* 2005;127(2):799-805.  
doi:10.1021/ja044688h
82. Dufort S, Bianchi A, Henry M, et al. Nebulized gadolinium-based nanoparticles: A theranostic approach for lung tumor imaging and radiosensitization. *Small.* 2015;11(2):215-221. doi:10.1002/smll.201401284
83. Yoo SS, Guo L, Sun X, et al. Fabrication and in vitro characterization of gadolinium-based nanoclusters for simultaneous drug delivery and radiation enhancement. *Nanotechnology.* 2016;27(38):385104. doi:10.1088/0957-4484/27/38/385104
84. Sancey L, Lux F, Kotb S, et al. The use of theranostic gadolinium-based nanoprobes to improve radiotherapy efficacy. *Br J Radiol.* 2014;87(1041):20140134.  
doi:10.1259/bjr.20140134
85. Bridot JL, Dayde D, Rivière C, et al. Hybrid gadolinium oxide nanoparticles combining imaging and therapy. *J Mater Chem.* 2009;19(16):2328-2335. doi:10.1039/b815836c
86. Xiao Q, Zheng X, Bu W, et al. A core/satellite multifunctional nanotheranostic for in vivo imaging and tumor eradication by radiation/photothermal synergistic therapy. *J Am Chem Soc.* 2013;135(35):13041-13048. doi:10.1021/ja404985w
87. Le Duc G, Roux S, Paruta-Tuarez A, et al. Advantages of gadolinium based ultrasmall nanoparticles vs molecular gadolinium chelates for radiotherapy guided by MRI for glioma treatment. *Cancer Nanotechnol.* 2014;5(1):1-14. doi:10.1186/s12645-014-0004-8

88. van der Meel R, Sulheim E, Shi Y, Kiessling F, Mulder WJM, Lammers T. Smart cancer nanomedicine. *Nat Nanotechnol.* 2019;14(11):1007-1017. doi:10.1038/s41565-019-0567-y
89. Mi P, Dewi N, Yanagie H, et al. Hybrid Calcium Phosphate-Polymeric Micelles Incorporating Gadolinium Chelates for Imaging-Guided Gadolinium Neutron Capture Tumor Therapy. *ACS Nano.* 2015;9(6):5913-5921. doi:10.1021/acsnano.5b00532
90. Rima W, Sancey L, Aloy MT, et al. Internalization pathways into cancer cells of gadolinium-based radiosensitizing nanoparticles. *Biomaterials.* 2013;34(1):181-195. doi:10.1016/j.biomaterials.2012.09.029
91. Khuntia D, Mehta M. Motexafin gadolinium: A clinical review of a novel radioenhancer for brain tumors. *Expert Rev Anticancer Ther.* 2004;4(6):981-989. doi:10.1586/14737140.4.6.981
92. Golombek SK, May JN, Theek B, et al. Tumor targeting via EPR: Strategies to enhance patient responses. *Adv Drug Deliv Rev.* 2018;130:17-38. doi:10.1016/j.addr.2018.07.007
93. Nasongkla N, Bey E, Ren J, et al. Multifunctional polymeric micelles as cancer-targeted, MRI-ultrasensitive drug delivery systems. *Nano Lett.* 2006;6(11):2427-2430. doi:10.1021/nl061412u
94. Cho K, Wang X, Nie S, Chen Z, Shin DM. Therapeutic nanoparticles for drug delivery in cancer. *Clin Cancer Res.* 2008;14(5):1310-1316. doi:10.1158/1078-0432.CCR-07-1441
95. Zhou Z, Lu ZR. Gadolinium-based contrast agents for magnetic resonance cancer

- imaging. *Wiley Interdiscip Rev Nanomedicine Nanobiotechnology*. 2013;5(1):1-18.  
doi:10.1002/wnan.1198
96. Bazzi R, Flores MA, Louis C, et al. Synthesis and properties of europium-based phosphors on the nanometer scale: Eu<sub>2</sub>O<sub>3</sub>, Gd<sub>2</sub>O<sub>3</sub>:Eu, and Y<sub>2</sub>O<sub>3</sub>:Eu. *J Colloid Interface Sci*. 2004;273(1):191-197. doi:10.1016/j.jcis.2003.10.031
97. Bazzi R, Flores-Gonzalez MA, Louis C, et al. Synthesis and luminescent properties of sub-5-nm lanthanide oxides nanoparticles. In: *Journal of Luminescence*. Vol 102-103. North-Holland; 2003:445-450. doi:10.1016/S0022-2313(02)00588-4
98. Louis C, Bazzi R, Marquette CA, et al. Nanosized hybrid particles with double luminescence for biological labeling. *Chem Mater*. 2005;17(7):1673-1682.  
doi:10.1021/cm0480162
99. Petoral RM, Söderlind F, Klasson A, et al. Synthesis and characterization of Tb<sup>3+</sup>-doped Gd<sub>2</sub>O<sub>3</sub> nanocrystals: A bifunctional material with combined fluorescent labeling and MRI contrast agent properties. *J Phys Chem C*. 2009;113(17):6913-6920.  
doi:10.1021/jp808708m
100. Fortin MA, Petoral RM, Söderlind F, et al. Polyethylene glycol-covered ultra-small Gd<sub>2</sub>O<sub>3</sub> nanoparticles for positive contrast at 1.5 T magnetic resonance clinical scanning. *Nanotechnology*. 2007;18(39):395501. doi:10.1088/0957-4484/18/39/395501
101. Engström M, Klasson A, Pedersen H, Vahlberg C, Käll PO, Uvdal K. High proton relaxivity for gadolinium oxide nanoparticles. *Magn Reson Mater Physics, Biol Med*. 2006;19(4):180-186. doi:10.1007/s10334-006-0039-x

102. Hussain Z, Khan S, Imran M, Sohail M, Shah SWA, de Matas M. PEGylation: a promising strategy to overcome challenges to cancer-targeted nanomedicines: a review of challenges to clinical transition and promising resolution. *Drug Deliv Transl Res.* 2019;9(3):721-734. doi:10.1007/s13346-019-00631-4
103. Kryza D, Taleb J, Janier M, et al. Biodistribution study of nanometric hybrid gadolinium oxide particles as a multimodal SPECT/MR/optical imaging and theragnostic agent. *Bioconjug Chem.* 2011;22(6):1145-1152. doi:10.1021/bc1005976
104. Mowat P, Mignot A, Rima W, et al. In vitro radiosensitizing effects of ultrasmall gadolinium based particles on tumour cells. In: *Journal of Nanoscience and Nanotechnology.* Vol 11. ; 2011:7833-7839. doi:10.1166/jnn.2011.4725
105. Le Duc G, Miladi I, Alric C, et al. Toward an image-guided microbeam radiation therapy using gadolinium-based nanoparticles. *ACS Nano.* 2011;5(12):9566-9574. doi:10.1021/nn202797h
106. Faure AC, Dufort S, Josserand V, et al. Control of the in vivo biodistribution of hybrid nanoparticles with different poly(ethylene glycol) coatings. *Small.* 2009;5(22):2565-2575. doi:10.1002/sml.200900563
107. Sancey L, Kotb S, Truillet C, et al. Long-term in Vivo clearance of gadolinium-based AGuIX nanoparticles and their biocompatibility after systemic injection. *ACS Nano.* 2015;9(3):2477-2488. doi:10.1021/acsnano.5b00552
108. Verry C, Dufort S, Lemasson B, et al. Targeting brain metastases with ultrasmall theranostic nanoparticles, a first-in-human trial from an MRI perspective. *Sci Adv.*

2020;6(29):eaay5279. doi:10.1126/sciadv.aay5279

109. Kotb S, Detappe A, Lux F, et al. Gadolinium-based nanoparticles and radiation therapy for multiple brain melanoma metastases: Proof of concept before phase I trial. *Theranostics*. 2016;6(3):418-427. doi:10.7150/thno.14018
110. Mignot A, Truillet C, Lux F, et al. A top-down synthesis route to ultrasmall multifunctional Gd-based silica nanoparticles for theranostic applications. *Chem - A Eur J*. 2013;19(19):6122-6136. doi:10.1002/chem.201203003
111. Lux F, Mignot A, Mowat P, et al. Ultrasmall rigid particles as multimodal probes for medical applications. *Angew Chemie - Int Ed*. 2011;50(51):12299-12303. doi:10.1002/anie.201104104
112. Radiotherapy of Multiple Brain Metastases Using AGuIX® - Full Text View - ClinicalTrials.gov. <https://clinicaltrials.gov/ct2/show/NCT03818386>. Accessed January 3, 2021.
113. Dufort S, Bianchi A, Henry M, et al. Nebulized gadolinium-based nanoparticles: A theranostic approach for lung tumor imaging and radiosensitization. *Small*. 2015;11(2):215-221. doi:10.1002/smll.201401284
114. Fries P, Morr D, Müller A, et al. Evaluation of a Gadolinium-Based Nanoparticle (AGuIX) for Contrast-Enhanced MRI of the Liver in a Rat Model of Hepatic Colorectal Cancer Metastases at 9.4 Tesla. *RoFo Fortschritte auf dem Gebiet der Rontgenstrahlen und der Bildgeb Verfahren*. 2015;187(12):1108-1115. doi:10.1055/s-0035-1553500

115. Verry C, Dufort S, Barbier EL, et al. MRI-guided clinical 6-MV radiosensitization of glioma using a unique gadolinium-based nanoparticles injection. *Nanomedicine*. 2016;11(18):2405-2417. doi:10.2217/nmm-2016-0203
116. Detappe A, Kunjachan S, Sancey L, et al. Advanced multimodal nanoparticles delay tumor progression with clinical radiation therapy. *J Control Release*. 2016;238:103-113. doi:10.1016/j.jconrel.2016.07.021
117. Lux F, Tran VL, Thomas E, et al. AGuiX<sup>®</sup> from bench to bedside-transfer of an ultrasmall theranostic gadolinium-based nanoparticle to clinical medicine. *Br J Radiol*. 2019;92(1093):20180365. doi:10.1259/bjr.20180365
118. Štefančíková L, Porcel E, Eustache P, et al. Cell localisation of gadolinium-based nanoparticles and related radiosensitising efficacy in glioblastoma cells. *Cancer Nanotechnology*. 2014;5(1). doi:10.1186/s12645-014-0006-6
119. Luchette M, Korideck H, Makrigiorgos M, Tillement O, Berbeco R. Radiation dose enhancement of gadolinium-based AGuiX nanoparticles on HeLa cells. *Nanomedicine Nanotechnology, Biol Med*. 2014;10(8):1751-1755. doi:10.1016/j.nano.2014.06.004
120. Miladi I, Aloy MT, Armandy E, et al. Combining ultrasmall gadolinium-based nanoparticles with photon irradiation overcomes radioresistance of head and neck squamous cell carcinoma. *Nanomedicine Nanotechnology, Biol Med*. 2015;11(1):247-257. doi:10.1016/j.nano.2014.06.013
121. Štefančíková L, Lacombe S, Salado D, et al. Effect of gadolinium-based nanoparticles on nuclear DNA damage and repair in glioblastoma tumor cells. *J Nanobiotechnology*.

- 2016;14(1):63. doi:10.1186/s12951-016-0215-8
122. Le Duc G, Miladi I, Alric C, et al. Toward an image-guided microbeam radiation therapy using gadolinium-based nanoparticles. *ACS Nano*. 2011;5(12):9566-9574. doi:10.1021/nm202797h
123. Bianchi A, Dufort S, Lux F, et al. Targeting and in vivo imaging of non-small-cell lung cancer using nebulized multimodal contrast agents. *Proc Natl Acad Sci U S A*. 2014;111(25):9247-9252. doi:10.1073/pnas.1402196111
124. Verry C, Dufort S, Villa J, et al. Theranostic AGuIX nanoparticles as radiosensitizer: A phase I, dose-escalation study in patients with multiple brain metastases (NANO-RAD trial). *Radiother Oncol*. 2021;160:159-165. doi:10.1016/j.radonc.2021.04.021
125. Byrne HL, Le Duc G, Lux F, et al. Enhanced MRI-guided radiotherapy with gadolinium-based nanoparticles: Preclinical evaluation with an MRI-linac. *Cancer Nanotechnol*. 2020;11(1):1-14. doi:10.1186/s12645-020-00065-5
126. Wu C, Cai R, Zhao T, et al. Hyaluronic Acid-Functionalized Gadolinium Oxide Nanoparticles for Magnetic Resonance Imaging-Guided Radiotherapy of Tumors. *Nanoscale Res Lett*. 2020;15(1). doi:10.1186/s11671-020-03318-9
127. Qin J, Liang G, Feng Y, et al. Synthesis of gadolinium/iron-bimetal-phenolic coordination polymer nanoparticles for theranostic applications. *Nanoscale*. 2020;12(10):6096-6103. doi:10.1039/c9nr10020b
128. Khan M, Boumati S, Arib C, et al. Doxorubicin (Dox) gadolinium–gold-complex: A new

- way to tune hybrid nanorods as theranostic agent. *Int J Nanomedicine*. 2021;16:2219-2236. doi:10.2147/IJN.S295809
129. Xia J, Xue Y, Lei B, et al. Multimodal channel cancer chemotherapy by 2D functional gadolinium metal–organic framework. *Natl Sci Rev*. 2021;8(7). doi:10.1093/NSR/NWAA221
130. Lomovskaya N, Otten SL, Doi-Katayama Y, et al. Doxorubicin overproduction in *Streptomyces peucetius*: Cloning and characterization of the *dnrU* ketoreductase and *dnrV* genes and the *doxA* cytochrome P-450 hydroxylase gene. *J Bacteriol*. 1999;181(1):305-318. doi:10.1128/jb.181.1.305-318.1999
131. Arcamone F, Cassinelli G, Fantini G, et al. Adriamycin, 14-hydroxydaimomycin, a new antitumor antibiotic from *S. Peucetius* var. *caesius*. *Biotechnol Bioeng*. 1969;11(6):1101-1110. doi:10.1002/bit.260110607
132. Pfizer Canada-Pharmaceuticals. *PRODUCT MONOGRAPH Pr DOXORUBICIN*.; 2019.
133. Lown JW. The mechanism of action of quinone antibiotics. *Mol Cell Biochem*. 1983;55(1):17-40. doi:10.1007/BF00229240
134. Lown JW. Discovery and development of anthracycline antitumour antibiotics. *Chem Soc Rev*. 1993;22(3):165-176. doi:10.1039/CS9932200165
135. Brown JR, Imam SH. 5 Recent Studies on Doxorubicin and its Analogues. *Prog Med Chem*. 1985;21(C):169-236. doi:10.1016/S0079-6468(08)70410-7
136. Singal PK, Iliskovic N. Doxorubicin-induced cardiomyopathy. *N Engl J Med*.

- 1998;339(13):900-905. doi:10.1056/NEJM199809243391307
137. Krishna R, Mayer LD. Multidrug resistance (MDR) in cancer Mechanisms, reversal using modulators of MDR and the role of MDR modulators in influencing the pharmacokinetics of anticancer drugs. *Eur J Pharm Sci.* 2000;11(4):265-283. doi:10.1016/S0928-0987(00)00114-7
138. Gabizon A, Shmeeda H, Barenholz Y. Pharmacokinetics of pegylated liposomal doxorubicin: Review of animal and human studies. *Clin Pharmacokinet.* 2003;42(5):419-436. doi:10.2165/00003088-200342050-00002
139. Leonard RCF, Williams S, Tulpule A, Levine AM, Oliveros S. Improving the therapeutic index of anthracycline chemotherapy: Focus on liposomal doxorubicin (Myocet™). *Breast.* 2009;18(4):218-224. doi:10.1016/j.breast.2009.05.004
140. Wei X, Ming LJ. Comprehensive 2D 1H NMR Studies of Paramagnetic Lanthanide(III) Complexes of Anthracycline Antitumor Antibiotics. *Inorg Chem.* 1998;37(9):2255-2262. doi:10.1021/ic970741+
141. Weiss RB. The anthracyclines: Will we ever find a better doxorubicin? *Semin Oncol.* 1992;19(6):670-686. doi:10.5555/uri:pii:009377549290036Z
142. Bouma J, Beijnen JH, Bult A, Underberg WJM. Anthracycline antitumour agents - A review of physicochemical, analytical and stability properties. *Pharm Weekbl Sci Ed.* 1986;8(2):109-133. doi:10.1007/BF02086146
143. Mi P, Kokuryo D, Cabral H, et al. A pH-activatable nanoparticle with signal-amplification

- capabilities for non-invasive imaging of tumour malignancy. *Nat Nanotechnol.* 2016;11(8):724-730. doi:10.1038/nnano.2016.72
144. Ganesh T, Mokhtari RB, Alhamami M, Yeger H, Cheng HLM. Manganese-enhanced MRI of minimally gadolinium-enhancing breast tumors. *J Magn Reson Imaging.* 2015;41(3):806-813. doi:10.1002/jmri.24608
145. Lee B Il, Lee KS, Lee JH, Lee IS, Byeon SH. Synthesis of colloidal aqueous suspensions of a layered gadolinium hydroxide: A potential MRI contrast agent. *Dalt Trans.* 2009;(14):2490-2495. doi:10.1039/b823172a
146. Zein R, Sharrouf W, Selting K. Physical Properties of Nanoparticles That Result in Improved Cancer Targeting. *J Oncol.* 2020;2020. doi:10.1155/2020/5194780
147. La-Beck NM, Gabizon AA. Nanoparticle interactions with the immune system: Clinical implications for liposome-based cancer chemotherapy. *Front Immunol.* 2017;8(APR):6-11. doi:10.3389/fimmu.2017.00416
148. Willard MA, Kurihara LK, Carpenter EE, Calvin S, Harris VG. Chemically prepared magnetic nanoparticles. *Int Mater Rev.* 2004;49(3-4):125-170. doi:10.1179/095066004225021882
149. Wu K, Su D, Liu J, Saha R, Wang JP. Magnetic nanoparticles in nanomedicine: A review of recent advances. *Nanotechnology.* 2019;30(50). doi:10.1088/1361-6528/ab4241
150. Lacerda S, Tóth É. Lanthanide Complexes in Molecular Magnetic Resonance Imaging and Theranostics. *ChemMedChem.* 2017;12(12):883-894. doi:10.1002/cmdc.201700210

151. Bünzli JCG. Lanthanide luminescence for biomedical analyses and imaging. *Chem Rev.* 2010;110(5):2729-2755. doi:10.1021/cr900362e
152. Zhou Z, Lu ZR. Gadolinium-based contrast agents for magnetic resonance cancer imaging. *Wiley Interdiscip Rev Nanomedicine Nanobiotechnology.* 2013;5(1):1-18. doi:10.1002/wnan.1198
153. Patil R, Galstyan A, Grodzinski ZB, et al. Single-and multi-arm gadolinium mri contrast agents for targeted imaging of glioblastoma. *Int J Nanomedicine.* 2020;15:3057-3070. doi:10.2147/IJN.S238265
154. Mi P, Dewi N, Yanagie H, et al. Hybrid Calcium Phosphate-Polymeric Micelles Incorporating Gadolinium Chelates for Imaging-Guided Gadolinium Neutron Capture Tumor Therapy. *ACS Nano.* 2015;9(6):5913-5921. doi:10.1021/acsnano.5b00532
155. Rima W, Sancey L, Aloy MT, et al. Internalization pathways into cancer cells of gadolinium-based radiosensitizing nanoparticles. *Biomaterials.* 2013;34(1):181-195. doi:10.1016/j.biomaterials.2012.09.029
156. Khuntia D, Mehta M. Motexafin gadolinium: A clinical review of a novel radioenhancer for brain tumors. *Expert Rev Anticancer Ther.* 2004;4(6):981-989. doi:10.1586/14737140.4.6.981
157. Nasongkla N, Bey E, Ren J, et al. Multifunctional polymeric micelles as cancer-targeted, MRI-ultrasensitive drug delivery systems. *Nano Lett.* 2006;6(11):2427-2430. doi:10.1021/nl061412u

158. Cho K, Wang X, Nie S, Chen Z, Shin DM. Therapeutic nanoparticles for drug delivery in cancer. *Clin Cancer Res.* 2008;14(5):1310-1316. doi:10.1158/1078-0432.CCR-07-1441
159. Yoo SS, Razzak R, Bédard E, et al. Layered gadolinium-based nanoparticle as a novel delivery platform for microRNA therapeutics. *Nanotechnology.* 2014;25(42):425102. doi:10.1088/0957-4484/25/42/425102
160. Krishna R, Mayer LD. Multidrug resistance (MDR) in cancer Mechanisms, reversal using modulators of MDR and the role of MDR modulators in influencing the pharmacokinetics of anticancer drugs. *Eur J Pharm Sci.* 2000;11(4):265-283. doi:10.1016/S0928-0987(00)00114-7
161. Leonard RCF, Williams S, Tulpule A, Levine AM, Oliveros S. Improving the therapeutic index of anthracycline chemotherapy: Focus on liposomal doxorubicin (Myocet<sup>TM</sup>). *Breast.* 2009;18(4):218-224. doi:10.1016/j.breast.2009.05.004
162. Gabizon A, Shmeeda H, Barenholz Y. Pharmacokinetics of pegylated liposomal doxorubicin: Review of animal and human studies. *Clin Pharmacokinet.* 2003;42(5):419-436. doi:10.2165/00003088-200342050-00002
163. Stefanakis D, Ghanotakis DF. Synthesis and characterization of gadolinium nanostructured materials with potential applications in magnetic resonance imaging, neutron-capture therapy and targeted drug delivery. *J Nanoparticle Res.* 2010;12(4):1285-1297. doi:10.1007/s11051-010-9848-y
164. Liu Z, Liu X, Yuan Q, et al. Hybrid mesoporous gadolinium oxide nanorods: A platform for multimodal imaging and enhanced insoluble anticancer drug delivery with low

- systemic toxicity. *J Mater Chem*. 2012;22(30):14982-14990. doi:10.1039/c2jm31100c
165. Di W, Ren X, Zhao H, Shirahata N, Sakka Y, Qin W. Single-phased luminescent mesoporous nanoparticles for simultaneous cell imaging and anticancer drug delivery. *Biomaterials*. 2011;32(29):7226-7233. doi:10.1016/j.biomaterials.2011.06.019
166. Huang S, Liu J, Liu D, Yuan Q. Facile and large-scale synthesis of Gd(OH)<sub>3</sub> nanorods for MR imaging with low toxicity. *New J Chem*. 2012;36(6):1335-1338. doi:10.1039/c2nj21009f
167. Hemmer E, Kohl Y, Colquhoun V, Thielecke H, Soga K, Mathur S. Probing cytotoxicity of gadolinium hydroxide nanostructures. *J Phys Chem B*. 2010;114(12):4358-4365. doi:10.1021/jp911607h
168. Yang Y, Sun Y, Liu Y, et al. Long-term in vivo biodistribution and toxicity of Gd(OH)<sub>3</sub> nanorods. *Biomaterials*. 2013;34(2):508-515. doi:10.1016/j.biomaterials.2012.09.075
169. Ganesh T, Mokhtari RB, Alhamami M, Yeger H, Cheng HLM. Manganese-enhanced MRI of minimally gadolinium-enhancing breast tumors. *J Magn Reson Imaging*. 2015;41(3):806-813. doi:10.1002/jmri.24608
170. Mi P, Kokuryo D, Cabral H, et al. A pH-activatable nanoparticle with signal-amplification capabilities for non-invasive imaging of tumour malignancy. *Nat Nanotechnol*. 2016;11(8):724-730. doi:10.1038/nnano.2016.72
171. Chiu GNC, Abraham SA, Ickenstein LM, et al. Encapsulation of doxorubicin into thermosensitive liposomes via complexation with the transition metal manganese. *J*

- Control Release*. 2005;104(2):271-288. doi:10.1016/j.jconrel.2005.02.009
172. Cheung BCL, Sun THT, Leenhouts JM, Cullis PR. Loading of doxorubicin into liposomes by forming Mn<sup>2+</sup>-drug complexes. *Biochim Biophys Acta - Biomembr*. 1998;1414(1-2):205-216. doi:10.1016/S0005-2736(98)00168-0
173. Abraham SA, Edwards K, Karlsson G, et al. Formation of transition metal-doxorubicin complexes inside liposomes. *Biochim Biophys Acta - Biomembr*. 2002;1565(1):41-54. doi:10.1016/S0005-2736(02)00507-2
174. Wei X, Ming LJ. Comprehensive 2D 1H NMR Studies of Paramagnetic Lanthanide(III) Complexes of Anthracycline Antitumor Antibiotics. *Inorg Chem*. 1998;37(9):2255-2262. doi:10.1021/ic970741+
175. Du G, Van Tendeloo G. Preparation and structure analysis of Gd(OH)<sub>3</sub> nanorods. *Nanotechnology*. 2005;16(4):595-597. doi:10.1088/0957-4484/16/4/043
176. Munshi A, Hobbs M, Meyn RE. Clonogenic cell survival assay. *Methods Mol Med*. 2005;110:21-28. doi:10.1385/1-59259-869-2:021
177. Schneider CA, Rasband WS, Eliceiri KW. NIH Image to ImageJ: 25 years of image analysis. *Nat Methods*. 2012;9(7):671-675. doi:10.1038/nmeth.2089
178. Direcks WGE, Van Gelder M, Lammertsma AA, Molthoff CFM. A new rat model of human breast cancer for evaluating efficacy of new anti-cancer agents in vivo. *Cancer Biol Ther*. 2008;7(4):532-537. doi:10.4161/cbt.7.4.5481
179. Bouma J, Beijnen JH, Bult A, Underberg WJM. Anthracycline antitumour agents - A

- review of physicochemical, analytical and stability properties. *Pharm Weekbl Sci Ed.* 1986;8(2):109-133. doi:10.1007/BF02086146
180. Jain RK, Stylianopoulos T. Delivering nanomedicine to solid tumors. *Nat Rev Clin Oncol.* 2010;7(11):653-664. doi:10.1038/nrclinonc.2010.139
181. Gratton SEA, Ropp PA, Pohlhaus PD, et al. The effect of particle design on cellular internalization pathways. *Proc Natl Acad Sci U S A.* 2008;105(33):11613-11618. doi:10.1073/pnas.0801763105
182. Brown KA, Yang X, Schipper D, et al. A self-assembling lanthanide molecular nanoparticle for optical imaging. *Dalt Trans.* 2015;44(6):2667-2675. doi:10.1039/c4dt02646b
183. Shen J, Sun LD, Zhu JD, Wei LH, Sun HF, Yan CH. Biocompatible bright YVO<sub>4</sub>:Eu nanoparticles as versatile optical bioprobes. In: *Advanced Functional Materials.* Vol 20. John Wiley & Sons, Ltd; 2010:3708-3714. doi:10.1002/adfm.201001264
184. Bünzli JCG. Lanthanide luminescence for biomedical analyses and imaging. *Chem Rev.* 2010;110(5):2729-2755. doi:10.1021/cr900362e
185. Le Duc G, Miladi I, Alric C, et al. Toward an image-guided microbeam radiation therapy using gadolinium-based nanoparticles. *ACS Nano.* 2011;5(12):9566-9574. doi:10.1021/nn202797h
186. Arcamone F, Cassinelli G, Fantini G, et al. Adriamycin, 14-hydroxydaimomycin, a new antitumor antibiotic from *S. Peucetius* var. *caesius*. *Biotechnol Bioeng.* 1969;11(6):1101-

1110. doi:10.1002/bit.260110607
187. Lomovskaya N, Otten SL, Doi-Katayama Y, et al. Doxorubicin overproduction in *Streptomyces peucetius*: Cloning and characterization of the *dnrU* ketoreductase and *dnrV* genes and the *doxA* cytochrome P-450 hydroxylase gene. *J Bacteriol.* 1999;181(1):305-318. doi:10.1128/jb.181.1.305-318.1999
188. Lown JW. Discovery and development of anthracycline antitumour antibiotics. *Chem Soc Rev.* 1993;22(3):165-176. doi:10.1039/CS9932200165
189. Lown JW. The mechanism of action of quinone antibiotics. *Mol Cell Biochem.* 1983;55(1):17-40. doi:10.1007/BF00229240
190. Weiss RB. The anthracyclines: Will we ever find a better doxorubicin? *Semin Oncol.* 1992;19(6):670-686. doi:10.5555/uri:pii:009377549290036Z
191. Bouma J, Beijnen JH, Bult A, Underberg WJM. Anthracycline antitumour agents - A review of physicochemical, analytical and stability properties. *Pharm Weekbl Sci Ed.* 1986;8(2):109-133. doi:10.1007/BF02086146
192. Ganesh T, Mokhtari RB, Alhamami M, Yeger H, Cheng HLM. Manganese-enhanced MRI of minimally gadolinium-enhancing breast tumors. *J Magn Reson Imaging.* 2015;41(3):806-813. doi:10.1002/jmri.24608
193. Mi P, Kokuryo D, Cabral H, et al. A pH-activatable nanoparticle with signal-amplification capabilities for non-invasive imaging of tumour malignancy. *Nat Nanotechnol.* 2016;11(8):724-730. doi:10.1038/nnano.2016.72

194. Lu ZR, Wang X, Parker DL, Goodrich KC, Buswell HR. Poly(L-glutamic acid) Gd(III)-DOTA conjugate with a degradable spacer for magnetic resonance imaging. *Bioconjug Chem.* 2003;14(4):715-719. doi:10.1021/bc0340464
195. Dekie L, Toncheva V, Dubruel P, Schacht EH, Barrett L, Seymour LW. Poly-L-glutamic acid derivatives as vectors for gene therapy. *J Control Release.* 2000;65(1-2):187-202. doi:10.1016/S0168-3659(99)00235-7
196. Li C. Poly(L-glutamic acid)-anticancer drug conjugates. *Adv Drug Deliv Rev.* 2002;54(5):695-713. doi:10.1016/S0169-409X(02)00045-5
197. Hirata N, Fujisawa Y, Tanabe K, Harada H, Hiraoka M, Nishimoto SI. Radiolytic activation of a cytarabine prodrug possessing a 2-oxoalkyl group: One-electron reduction and cytotoxicity characteristics. *Org Biomol Chem.* 2009;7(4):651-654. doi:10.1039/b816194a
198. Tanabe K, Ebihara M, Hirata N, Nishimoto S ichi. Radiolytic one-electron reduction characteristics of tyrosine derivative caged by 2-oxopropyl group. *Bioorganic Med Chem Lett.* 2008;18(23):6126-6129. doi:10.1016/j.bmcl.2008.10.018
199. Tan J, Shah S, Thomas A, Ou-Yang HD, Liu Y. The influence of size, shape and vessel geometry on nanoparticle distribution. *Microfluid Nanofluidics.* 2013;14(1-2):77-87. doi:10.1007/s10404-012-1024-5
200. Kinnear C, Moore TL, Rodriguez-Lorenzo L, Rothen-Rutishauser B, Petri-Fink A. Form Follows Function: Nanoparticle Shape and Its Implications for Nanomedicine. *Chem Rev.* 2017;117(17):11476-11521. doi:10.1021/acs.chemrev.7b00194

201. Mann AKP, Schenck L, Koynov A, et al. Producing Amorphous Solid Dispersions via Co-Precipitation and Spray Drying: Impact to Physicochemical and Biopharmaceutical Properties. *J Pharm Sci.* 2018;107(1):183-191. doi:10.1016/j.xphs.2017.07.001
202. Vranić E. Amorphous pharmaceutical solids. *Bosn J Basic Med Sci.* 2004;4(3):35-39. doi:10.17305/bjbms.2004.3383
203. Willard MA, Kurihara LK, Carpenter EE, Calvin S, Harris VG. Chemically prepared magnetic nanoparticles. *Int Mater Rev.* 2004;49(3-4):125-170. doi:10.1179/095066004225021882
204. Merbach A, Helm L, Tóth É. *The Chemistry of Contrast Agents in Medical Magnetic Resonance Imaging: Second Edition.*; 2013. doi:10.1002/9781118503652
205. Leibfarth S, Mönnich D, Welz S, et al. A strategy for multimodal deformable image registration to integrate PET/MR into radiotherapy treatment planning. *Acta Oncol (Madr).* 2013;52(7):1353-1359. doi:10.3109/0284186X.2013.813964
206. Lee ES, Gao Z, Bae YH. Recent progress in tumor pH targeting nanotechnology. *J Control Release.* 2008;132(3):164-170. doi:10.1016/j.jconrel.2008.05.003
207. Feng L, Dong Z, Tao D, Zhang Y, Liu Z. The acidic tumor microenvironment: A target for smart cancer nano-theranostics. *Natl Sci Rev.* 2018;5(2):269-286. doi:10.1093/nsr/nwx062
208. Lin J, Alexander-Katz A. Cell membranes open “doors” for cationic nanoparticles/ biomolecules: Insights into uptake kinetics. *ACS Nano.* 2013;7(12):10799-10808.

doi:10.1021/nm4040553

209. Cho EC, Xie J, Wurm PA, Xia Y. Understanding the role of surface charges in cellular adsorption versus internalization by selectively removing gold nanoparticles on the cell surface with a I<sup>2</sup>/KI etchant. *Nano Lett.* 2009;9(3):1080-1084. doi:10.1021/nl803487r
210. Dougherty A, Nasution ELY, Iskandar F, Dougherty G. Facile solvothermal synthesis and functionalization of polyethylene glycol-coated paramagnetic Gd<sub>2</sub>(CO<sub>3</sub>)<sub>3</sub> particles and corresponding Gd<sub>2</sub>O<sub>3</sub> nanoparticles for use as MRI contrast agents. *J Sci Adv Mater Devices.* 2019;4(1):72-79. doi:10.1016/j.jsamd.2018.12.005
211. Matsumoto K, Saitoh H, Doan TLH, et al. Destruction of tumor mass by gadolinium-loaded nanoparticles irradiated with monochromatic X-rays: Implications for the Auger therapy. *Sci Rep.* 2019;9(1):1-10. doi:10.1038/s41598-019-49978-1
212. Shao C, Li S, Gu W, et al. Multifunctional Gadolinium-Doped Manganese Carbonate Nanoparticles for Targeted MR/Fluorescence Imaging of Tiny Brain Gliomas. *Anal Chem.* 2015;87(12):6251-6257. doi:10.1021/acs.analchem.5b01639
213. Liang G, Cao L, Chen H, et al. Ultrasmall gadolinium hydrated carbonate nanoparticle: An advanced T<sub>1</sub> MRI contrast agent with large longitudinal relaxivity. *J Mater Chem B.* 2013;1(5):629-638. doi:10.1039/c2tb00243d
214. Khalil IR, Irorere VU, Radecka I, et al. Poly- $\gamma$ -glutamic acid: Biodegradable polymer for potential protection of beneficial viruses. *Materials (Basel).* 2016;9(1):1-13. doi:10.3390/ma9010028

215. Sakamoto K, Schmidt JW, Wagner KU. Mouse models of breast cancer. *Methods Mol Biol.* 2015;1267:47-71. doi:10.1007/978-1-4939-2297-0\_3
216. Holen I, Speirs V, Morrissey B, Blyth K. In vivo models in breast cancer research: Progress, challenges and future directions. *DMM Dis Model Mech.* 2017;10(4):359-371. doi:10.1242/dmm.028274
217. Verry C, Dufort S, Lemasson B, et al. Targeting brain metastases with ultrasmall theranostic nanoparticles, a first-in-human trial from an MRI perspective. *Sci Adv.* 2020;6(29):eaay5279. doi:10.1126/sciadv.aay5279
218. Lacerda S, Tóth É. Lanthanide Complexes in Molecular Magnetic Resonance Imaging and Theranostics. *ChemMedChem.* 2017;12(12):883-894. doi:10.1002/cmdc.201700210
219. Seddon B, Strauss SJ, Whelan J, et al. Gemcitabine and docetaxel versus doxorubicin as first-line treatment in previously untreated advanced unresectable or metastatic soft-tissue sarcomas (GeDDiS): a randomised controlled phase 3 trial. *Lancet Oncol.* 2017;18(10):1397-1410. doi:10.1016/S1470-2045(17)30622-8
220. Volkova M, Russell R. Anthracycline Cardiotoxicity: Prevalence, Pathogenesis and Treatment. *Curr Cardiol Rev.* 2012;7(4):214-220. doi:10.2174/157340311799960645
221. Zhao N, C Woodle M, Mixson AJ. Advances in Delivery Systems for Doxorubicin. *J Nanomed Nanotechnol.* 2018;09(05):519. doi:10.4172/2157-7439.1000519
222. Xu W, Park JY, Kattel K, et al. Fluorescein-polyethyleneimine coated gadolinium oxide nanoparticles as T1 magnetic resonance imaging (MRI)-cell labeling (CL) dual agents.

- RSC Adv.* 2012;2(29):10907-10915. doi:10.1039/c2ra21052e
223. Wilhelm S, Tavares AJ, Dai Q, et al. Analysis of nanoparticle delivery to tumours. *Nat Rev Mater.* 2016;1(5):16014. doi:10.1038/natrevmats.2016.14
224. Direcks WGE, Van Gelder M, Lammertsma AA, Molthoff CFM. A new rat model of human breast cancer for evaluating efficacy of new anti-cancer agents in vivo. *Cancer Biol Ther.* 2008;7(4):532-537. doi:10.4161/cbt.7.4.5481
225. Denny KH, Stewart CW. *Acute, Sub-Acute, Sub-Chronic and Chronic General Toxicity Testing for Preclinical Drug Development.* Second Edi. Elsevier Inc.; 2013. doi:10.1016/B978-0-12-387815-1.00005-8
226. Kratz F, Ehling G, Kauffmann HM, Unger C. Acute and repeat-dose toxicity studies of the (6-maleimidocaproyl)hydrazone derivative of doxorubicin (DOXO-EMCH), an albumin-binding prodrug of the anticancer agent doxorubicin. *Hum Exp Toxicol.* 2007;26(1):19-35. doi:10.1177/0960327107073825
227. Reynolds CH, Annan N, Beshah K, et al. Gadolinium-loaded nanoparticles: New contrast agents for magnetic resonance imaging. *J Am Chem Soc.* 2000;122(37):8940-8945. doi:10.1021/ja001426g
228. Rispin A, Farrar D, Margosches E, et al. Alternative methods for the median lethal dose (LD50) test: The up-and-down procedure for acute oral toxicity. *ILAR J.* 2002;43(4):233-243. doi:10.1093/ilar.43.4.233